Realia et naturalia

DISSERTATIONES
CHIMICAE
UNIVERSITATIS
TARTUENSIS
146

INDREK TALLO

Synthesis and characterization of new micro-mesoporous carbide derived carbon materials for high energy and power density electrical double layer capacitors

DISSERTATIONES CHIMICAE UNIVERSITATIS TARTUENSIS
146

DISSERTATIONES CHIMICAE UNIVERSITATIS TARTUENSIS
146

INDREK TALLO

Synthesis and characterization of new micro-mesoporous carbide derived carbon materials for high energy and power density electrical double layer capacitors

UNIVERSITY OF TARTU
PRESS
1632

Institute of Chemistry, Faculty of Science and Technology, University of Tartu, Estonia

Dissertation is accepted for the commencement of the degree of Doctor of Philosophy in Chemistry on June 18th, 2015 by the Council of Institute of Chemistry, University of Tartu.

Supervisors: Prof. Enn Lust
Institute of Chemistry, University of Tartu, Estonia

Ph.D. Alar Jänes
Institute of Chemistry, University of Tartu, Estonia

Ph.D. Thomas Thomberg
Institute of Chemistry, University of Tartu, Estonia

Opponent: Prof. Pawel J. Kulesza
Department of Chemistry, University of Warsaw, Poland

Commencement: August 28th, 2015, at 12:00
14a Ravila Street, Tartu (Chemicum), auditorium 1021

ISSN 1406-0299
ISBN 978-9949-32-881-9 (print)
ISBN 978-9949-32-882-6 (pdf)

University of Tartu Press
www.tyk.ee

TABLE OF CONTENTS

I. LIST OF ORIGINAL PUBLICATIONS

I. **I. Tallo**, T. Thomberg, K. Kontturi, A. Jänes, E. Lust, Nanostructured carbide-derived carbon synthesized by chlorination of tungsten carbide. Carbon, 49 (13) 4427–4433 (2011).

II. **I. Tallo**, T. Thomberg, A. Jänes, E. Lust, Electrochemical Behaviour of α-Tungsten Carbide-Derived Carbon Based Electric Double-Layer Capacitors. Journal of the Electrochemical Society, 159 (3) A208–A213 (2012).

III. **I. Tallo**, T. Thomberg, H. Kurig, A. Jänes, K. Kontturi, E. Lust, Supercapacitors based on carbide-derived carbons synthesised using HCl and Cl_2 as reactants. Journal of Solid State Electrochemistry, 17 (1) 19–28 (2013).

IV. **I. Tallo**, T. Thomberg, H. Kurig, K. Kontturi, A. Jänes, E. Lust, Novel Micromesoporous Carbon Materials Synthesized from Tantalum Hafnium Carbide and Tungsten Titanium Carbide. Carbon 67, 607–616 (2014).

Author's contribution

Paper I: Performed all the material synthesis. Participated in the analysis of data and preparation of the manuscript.

Paper II: Performed all the electrochemical measurements and analysis of data. Participated in the preparation of the manuscript.

Paper III: Performed all the material synthesis, electrochemical measurements and analysis of data. Responsible for the preparation of manuscript.

Paper IV: Performed all the material synthesis, electrochemical measurements and analysis of data. Responsible for the preparation of manuscript.

2. ABBREVIATIONS AND SYMBOLS

ac – alternating current
A_{CS} – cross-section area of the adsorbate molecule
AN – acetonitrile
av – alternating voltage
BET – Brunauer-Emmett-Teller
BJH – Barret-Joyner-Halenda
C – total capacitance
$C''(\omega)$ – imaginary part of the capacitance
$C'(\omega)$ – real part of the capacitance
C_{cc} – capacitance calculated from constant current measurements
CCCD – constant current charge/discharge
C_{coe} – the coefficient constant related to the adsorption interaction energy
C_{CV} – capacitance calculated from cyclic voltammetry measurements
C_D – the capacitance of the diffuse layer
CDC – carbide derived carbon
C_H – capacitance of the inner Helmholtz layer
C_m – specific gravimetric capacitance
C_p – parallel capacitance
C_s – series capacitance
CV – cyclic voltammetry
d – distance
dc – direct current
DR – Dubinin-Radushkevich
$E(i\omega)$ – voltage fasor
ΔE – cell potential
E_0 – the maximum amplitude of the av signal
EDLC – electrical double layer capacitor
EDX – electron dispersive X-ray spectroscopy
EELS – electron energy loss spectroscopy
EIS – electrochemical impedance spectroscopy
ELNES – energy loss near edge structure
E_{max} – maximum specific energy
f – ac current frequency
FIB – focused ion beam
f_R – frequency corresponding to the relaxation time constant
FWHM – full width at half-maximum
HK – Horvath-Kowazoe
HRTEM – high resolution transmission electron microscopy
I – current
i – imaginary number
$I(i\omega)$ – current fasor
$I(t)$ – time dependent output current
I_0 – initial current

I_D – intensity of the D-peak (Raman)
I_G – intensity of the G-peak (Raman)
j – current density
K – the X-ray wavelength
L_a – estimated average crystallite sizes along the a-directions of the graphitic structure
L_c – estimated average crystallite sizes along the c-directions of the graphitic structure
m – mass
M – molar mass
m_f – final weight of the sample
m_i – initial weight of the sample
m_{tot} – mass of two electrodes
N_A – the Avogadro constant
NLDFT – non-local density functional theory
p – pressure
$P(\omega)$ – active power (i.e. real) component of the complex power
p/p_0 – relative pressure
p_0 – atmospheric pressure
PC – propylene carbonate
P_{max} – maximum specific power
PTFE – polytetrafluoroethylene
PVDC – polyvinylidendichloride
PVDF – polyvinylidendifluoride
$Q(\omega)$ – reactive (i.e. imaginary) power component of the complex power
r – radius of the pore
R – total resistance of the system
RC – resistance–capacitance (circuit)
R_p – parallel resistance
R_s – series resistance
$S(\omega)$ – complex power
SAED – selected area electron diffraction
S_{BET} – specific surface area, calculated using the BET theory
SC – supercapacitor
SEM – scanning electron microscopy
S_{micro} – micropore surface area calculated using the *t*-plot method
T – temperature
t – time
TEM – transmission electron microscopy
t_{stat} – the statistical thickness of the adsorbed layer
T_{synth} – synthesis temperature
v – voltage scan rate
V_{micro} – micropore volume calculated using the *t*-plot method
V_{tot} – total pore volume
W – mass of the adsorbed gas at its relative pressure p/p_0,

W_m – the mass of a monolayer of an adsorbed gas
XPS – X-ray photoelectron spectroscopy
XRD – X-ray diffraction
$Z''(\omega)$ – imaginary part of the impedance
$Z'(\omega)$ – real part of the impedance
$Z(\omega)$ – impedance (complex resistance)
$|Z(\omega)|$ – impedance modulus
β – the full width at half-maximum of the reflections (XRD)
ΔE_{rms} – the root mean square of the potential
ε – dielectric constant of the environment
ε_0 – dielectric permeability of vacuum
θ – position of a reflection (XRD)
ϖ – extent of conversion
τ_R – characteristic relaxation time constant
χ – the mass fraction of carbon in the carbide
ω – angular frequency
θ – phase angle between voltage and current

3. INTRODUCTION

Carbon can be considered one of the most used materials in the world. Depending on the structure and origin, carbon materials exhibit different physical, chemical and electrochemical properties [1,2]. Continuous interest in the development of porous carbon materials with relatively high specific surface area and controlled pore size distribution is directly related to the wide area of their potential applications such as adsorbents/absorbents for gas (H_2, CH_4) storage, catalyst support, electrode material for supercapacitors, sea water desalination devices, etc. [1–5].

A very promising application of porous carbon is its use as an electrode material in supercapacitors [6,7]. Supercapacitors are important energy storage systems, which can be used in various areas of modern technology such as pulse energy generation systems, electrical transportation and consumer goods. For the optimization of the energy density – power density properties of supercapacitors, such parameters of porous carbon as the specific surface area, pore volume, pore size distribution and electrical conductivity have to be optimized [6,8–11]. Therefore, it is important to synthesize different carbon materials under controlled conditions to establish the parameters influencing the porous carbon material characteristics.

Carbide-derived carbons (CDCs) are micro- and mesoporous materials with very high specific surface area [8,12]. CDCs are produced by selective extraction of non-carbon elements from carbides, applying halogens or halogen containing gases at elevated temperatures. Various binary and ternary carbides have been chlorinated to prepare porous carbons, including TiC, Al_4C_3, Mo_2C, VC, SiC, WC, $WTiC_2$ and Ta_4HfC_5. The results of these studies show that the porous structure of CDCs produced depends especially on the origin and uniformity of the precursor carbide selected as a raw material. Depending on the experimental conditions (temperature, reaction time, etc.) applied, CDC synthesis enables the formation of a variety of different carbon structures such as amorphous carbon, carbon onions, nano-diamonds, nanotubes, graphite ribbons and ordered graphite [8,12–21].

Previously it has been found that compared to the other amorphous porous carbons, CDC materials have some advantages such as high purity, narrow pore size distribution within selected porosity regions and hierarchical structure of the micro- and mesopores. The overall shape of the initial binary carbide particles also remains unchanged during chlorination and no significant shrinkage occurs. Thus, the shape of the resulting carbon can be influenced mainly by the precursor carbide particle size selected. The pore size distribution of the resulting powders can be adjusted by the selection of precursor carbide and the chlorination temperature applied [8,12–22].

The main aim of this work was to synthesize CDC materials from different binary and ternary carbides (WC, TiC, $WTiC_2$ and Ta_4HfC_5) at various temperatures. Various physical and electrochemical characterization techniques were carried out to obtain a better understanding of the synthesized CDC materials and how the physical properties of carbon powders prepared correlate to the electrochemical behavior in supercapacitor applications.

4. LITERATURE OVERVIEW

4.1. Nanoporous carbon materials

Carbon is considered an extraordinary element due to its high number of possible allotropic forms and as a result having very variable physical properties [1–3]. The most known examples these allotropes are graphite, diamond, amorphous carbon, fullerenes and carbon nanotubes. While graphite and diamond are found as minerals, the other forms of carbon are mostly of synthetic origin.

Most of the carbon used in modern technology can be considered as engineered carbons which have mainly an amorphous structure. Amorphous carbon can be viewed as a mix of little domains of highly twisted sheets of graphene and carbon atoms with different sp-hybridization states between them. Some of these materials can be turned into graphite by applying high temperatures (over 2000 °C) where the twisted sheets of graphene align and form larger graphite crystals [1,2,4,23].

Large quantities of carbon materials are produced from carbon rich organic precursors using high temperature carbonization process. Some widely used forms of carbon materials are produced from biomass such as wood, coconut shells, hay, etc., and from synthetic polymers such as polyvinylidendifluoride (PVDF) and polyvinylidendichloride (PVDC). Thanks to the extraction of volatile compounds and the remaining complex and strong carbonized structure, it is possible to obtain very porous materials, sometimes even without the need for additional activation or post-treatment [5,23]. The properties of these carbon materials depend strongly on several variables applied during synthesis such as composition of precursor, reactor design, temperature, pressure and duration of the synthesis process applied, as well as on the chemical composition of activators used. During carbonization the precursor thermally decomposes (pyrolysis) and therefore the volatile components and heteroatoms are removed. The higher the temperature, the easier it is for the carbon atoms to reorganize and as a result, the small ordered microcrystals will be formed. The choice of precursor and carbonization parameters determines the sizes and orientations of the graphite crystals and amorphous area structures, thus, determining the carbon materials structure and physical properties [1–5,23,24].

4.1.1. Carbide derived carbon materials

Carbide derived carbons (CDC) are porous carbon materials which are prepared by halogenation (by reaction with Cl_2, Br_2, F_2, HCl, HBr, or HF) of metal (TiC, Mo_2C, Al_4C_3, VC, WC, Cr_3C_2, etc.) or nonmetal (SiC, B_4C, etc.) carbides. A very interesting property of CDC is that the carbon particles mainly retain the shape of initial binary carbide precursor particles and its porous properties are highly dependent on the chemical composition and crystallographic structure of the initial carbide used. The most applied method for the synthesis of CDC is the high-temperature chlorination process, although other halogen or halogen

containing gases are usable. The positive aspects of CDC, when compared with other activated porous carbon materials, are high purity, narrow pore size distribution, good electric conductivity and the possibility to fine-tune the average pore sizes. It has been demonstrated many times [6–8,13,14,25,26] that it is possible to alter the mentioned properties by choosing precursors or changing synthesis conditions, i.e., temperature or reactant or both [8,14]. Usually there is an optimal chlorination temperature determining the optimal ratio of micropores (pores with diameter of less than 2 nm) and mesopores (pores with diameter between 2 nm and 50 nm). However, based on the chemical composition of the raw carbide used (i.e., on the activity of the metal cation (redox potential)), the optimal synthesis temperature (T_{synth}) varies from 500 °C to 1200 °C, depending strongly on the final application area of the CDC applied. For electrical double layer capacitors (EDLC), some amount of mesopores and a high amount of micropores is required because in addition to the adsorption of ions into micropores, the quick transport of ions (taking mainly place in mesopores) is required. As it was shown by Eikerling et al. [9] the hierarchical structure for development of quickly chargeable high power density EDLC is an inevitable pre-requisite [6–9,13–16,25,26].

Using SiC as precursor [27] only microporous materials can be synthesized. From TiC [16] and VC [17] mainly microporous materials with limited amount of mesopores can be prepared. From chromium carbides (Cr_3C_2; Cr_7C_3; Cr_2C_6) [14] mainly mesoporous materials can be prepared.

However, from Al_4C_3, B_4C and especially from Mo_2C powder, carbon materials with hierarchical micro- and mesoporous structure have been prepared [13].

Mo_2C-CDC based amorphous carbons form the most complicated, but interesting class of CDC materials giving the mainly microporous CDC at $T_{synth} \leq 700$ °C and mainly mesoporous partially graphitized carbon powders at $T_{synth} \geq 1000$ °C. It should be mentioned that based on the systematical studies of the electrical double layer capacitor single cells, the Mo_2C-CDC synthesized at $T_{synth} = 800$ °C demonstrates very short charging/discharging times and, thus, extremely high power densities have been calculated for EDLCs [18].

The crystallographic characteristics of synthesized CDC have been systematically studied using X-ray diffraction (XRD); X-ray photoelectron spectroscopy (XPS) and high resolution transmission electron microscopy (HRTEM) combined with electron energy loss (EELS) and selected area electron diffraction (SAED) methods. In addition, Raman spectroscopy method has been applied for the analysis of graphitization level of CDC prepared [28,29].

The graphitization level depends extremely strongly on the raw carbide chemical composition, determining the crystallographic structure of raw binary carbide powder. CDCs synthesized from binary carbides crystallizing in hexagonal crystallographic syngony (Mo_2C), are characterized by lower graphitization temperatures ($T_{synth} \leq 900$ °C) than binary carbides with rhombohedral crystallographic syngony (α-SiC, B_4C, etc.). CDCs synthesized from binary carbides crystallizing in cubic crystallographic syngony have usually higher graphitization temperatures compared with that for hexagonal (Mo_2C) structure.

As has been shown earlier [30], with the increase of T_{synth} the graphitization level of final CDC powder increases (generally up to 40 – 60 % at $T_{synth} \geq 1000$ °C for Mo_2C-CDC). The same tendency seems to be valid for TiC-CDC, VC-CDC and WC-CDC, however, forming smaller graphitic areas (few layers at some surface regions) at somewhat higher synthesis temperatures $T_{synth} \geq 1100$ °C.

Systematic analysis of focused ion beam scanning electron microscopy electron dispersive X-ray spectroscopy (FIB-SEM-EDX), XPS and focused ion beam secondary ion mass spectroscopy (FIB-SIMS) data indicates that fully reacted CDC are free of contaminating additives and due to high temperature cleaning step with molecular hydrogen, they do not contain any raw carbides, chlorine, chlorides as well as any other intermediates [31–33].

4.2. Supercapacitors

Supercapacitors (SC) are electrochemical energy storage devices, which are applicable for quick storage and release of energy. In literature they are also known as ultracapacitors. While looking at specific energy and power, supercapacitors lie between batteries and traditional dielectric capacitors. Depending on the structural and physical design, the specific power and energy values of supercapacitors can vary over several orders of magnitude. Due to wide variability in power densities, they can be used in many applications either as independent energy storage or combined with other energy sources, such as batteries and fuel cells, in hybrid energy recuperation/regeneration complexes [10–12,34,35].

Supercapacitors can be charged and discharged quickly at power densities exceeding 1 kW kg^{-1}. This results from physical charge storage mechanism, which is quick and electrochemically effective. Supercapacitors can also be cycled up to a million times or even more. For these reasons they are already being used in various areas of modern technology such as consumer goods, lifting and transport (cars, trains, ships, airplanes, etc.) systems and even in industrial energetics [10,22].

Practical development and theoretical studies in the field of supercapacitors are divided in two directions, based on the charge storage mechanism. These are the electrical double layer capacitors (EDLC) which store energy through formation of the electric double layer, and the hybrid capacitors, which store energy, in addition to the electric double layer, through faradic nearly reversible redox reactions [10,22].

EDLC-s store energy by means of charge separation, i.e., adsorption of ions at the electrode surface and the capacitance that results from it is of electrostatic origin in both electrodes. The specific energy of EDLC is considerably larger than that for conventional dielectrical capacitor due to the huge specific surface area (surface porosity and roughness of electrodes) applicable for ion adsorption. The distance between opposite ionic adsorption layer, i.e., charge layers is roughly the thickness of the electrical double layers (diameter of the

solvent molecule – 0.3–0.6 μm). The extremely high surface area results from micropores (including atomic scale roughness) of the carbon matrix. These properties of electrodes make it possible to store a significant amount of charge as adsorbed ions onto/into the porous electrode. The process of storing and releasing energy is fast because it is based on the physical adsorption of ions on the electrode surface and therefore the adsorption relaxation time is very short. In batteries and battery type electrodes, the charge accumulation and release processes are much slower because in addition to mass transfer the slower steps such as heterogeneous charge transfer and surface restructuring reactions take place [10,12,19,22,30,36,37].

In hybrid capacitors nearly reversible faradic charge transfer process (ideal case) takes place at one electrode (so-called faradic electrode) and the faradic capacitance (accumulated charge is proportional to the electrochemically redox active compound's mass) resulting from it is not purely of electrostatic origin. The other electrode is usually a pure EDLC type and no faradic reactions take place there. For hybrid capacitors, within potential region of intensive redox processes (redox peaks in CV), the capacitance is more related to the electrochemical faradic charge transfer processes at the surface and the accumulated charge density is limited by the amount of electrochemically active material accumulated or deposited at the surface, formed during the charge transfer, i.e., energy accumulation step. Since in hybrid capacitors the stored energy is based mainly on the faradic redox processes, they also have many properties similar to batteries [10,12,38].

4.2.1. Electrical double layer structure and accumulation of ions, i.e., energy storage of the electrical double layer capacitors

The first model of the electrical double layer was presented by Helmholtz in 1853 and nowadays it is known as Helmholtz theory [39]. According to this theory, the electrical double layer at the surface of the electrode consists of two parallel layers of oppositely charged particles. One is the layer of charges developed on the surface of the metal and the other is a layer of ions drawn to near the surface of the metal electrode. The distance between these layers is approximately equal to the diameter of the solvent molecule. It was assumed that the charge within these layers is uniformly distributed all over the interface.

In Helmholtz theory the electrical double layer capacitance can be approximated as capacitance for the traditional plate capacitor. Thus, capacitance (C) can be described by equation:

$$C = \frac{\varepsilon\varepsilon_0}{d}, \tag{1}$$

where ε_0 is the dielectric permeability of vacuum, ε is the dielectric constant of the environment and d is the distance between the plates. While the assumption of the uniformly distributed charge over the interface can be reasonable for ideal

metals, then the assumption of uniformly accumulated layer of ions is unlikely for the solution side. For example in the case of specific adsorption, certain areas of the electric double layer are formed by different ions, which have different adsorption energies and distances of the closest approach of ions onto the electrode surface [39–41].

However, somewhat surprisingly, the Helmholtz theory is in rather good agreement with the experimental results for concentrated electrolytes, but it does not describe, for example, the dependence of differential capacitance (and charge density) on temperature, electrolyte concentration and on Gibbs adsorption (Gibbs energy) of specifically adsorbed ions, i.e., on the surface active additions in the electrolyte.

The next model for the electrical double layer was developed independently by Gouy (1910) and Chapman (1913) [42,43]. These models (so-called Gouy-Chapman theory) take the ions in the solution as ideal mathematical points which are in constant thermal motion. Remarkably, there is also no compact Helmholtz layer on the electrode surface and the ions that create the electrical double layer at the electrode|solution interface are in continuous thermal motion. The electric field, which originates from the charge of the electrode, makes the oppositely charged ions to preferably move to the electrode surface. This theory is applicable only in very dilute electrolyte solutions because it does not take into consideration the real sizes of ions.

The theories developed by Helmholtz and Gouy-Chapman were unified by Stern in 1924 [42–44]. According to the Stern theory, the charge of the electrode is compensated by the charge of ions which are located in two distinct layers. One of them is located near the surface of the interface and forms the so-called inner layer, sometimes known as the Helmholtz layer. The distance between the ions at the outer Helmholtz plane and the metal interface is equal to the radius of the ions (solvated ions). The other dynamic layer of the ions makes up the so-called diffuse layer, where the particles are in continuous thermal motion and are further away from the interface than the Helmholtz layer. The cumulative charge of these two layers is equal in magnitude to the surface charge of the ideal metal electrode [44].

The models of Gouy-Chapman and Stern were additionally improved by Frumkin and Grahame, dividing the Helmholtz layer into two parts for electrolytes containing specifically adsorbed ions (specifically adsorbed ions are ions with very low solvation energy). The inner Helmholtz layer consists of specifically adsorbed ions and the outer Helmholtz layer consists of ions that are not specifically adsorbed. The latter is therefore the minimum distance between the physically adsorbed ions onto the electrode surface. The outer Helmholtz plane is also the plane from which the ions in thermal motion can move without additional energy barriers and, thus, they are forming the diffuse layer. Grahame showed that when no specific adsorption of ions or solvent molecules takes place, the electrical double layer can be modeled as two capacitors connected in series:

$$\frac{1}{C} = \frac{1}{C_{\mathrm{H}}} + \frac{1}{C_{\mathrm{D}}}, \tag{2}$$

where C is the differential capacitance of the electric double layer, C_{H} is the capacitance of the inner (Helmholtz) layer and C_{D} is the capacitance of the diffuse layer [45,46].

There are many more novel theories, based on the modern physics, for the electrical double layer which usually take into account the Kohn-Sham model [47] for electric conductors and statistical models for electrolyte solutions with many variables and are therefore more complex. Some of these for example are known as Rice, Thomas-Fermi, modified Thomas-Fermi and Hurwitz-Parsons models [48–51]. These models take into account the non-ideal properties of the metal, where the so-called potential drop within the surface of the non-ideal metal electrode occurs [52,53]. For electrodes with low concentration of charge carriers and limited number of "free" electrons like Bi, Sb and especially carbon electrodes, the potential drop has very important influence onto the total capacitance of the non-ideal electrode|electrolyte interface. However, it should be noted that at the time being there is no agreement how to apply the modified Thomas-Fermi or other novel models, worked out and tested for single crystal plane electrodes with ideal crystalline structure [40,54], for the porous and rough semiconducting carbon electrodes.

The high capacitance of supercapacitors is determined by the very high specific surface area (up to 2500 $m^2\ g^{-1}$) and very small distance between the opposite charges (10^{-10} m) forming the electrical double layer. The specific energy ($E_{\max}$) and specific power ($P_{\max}$) can be calculated according to equations

$$E_{\max} = \frac{1}{2}\frac{C\Delta E^2}{m} \tag{3}$$

and

$$P_{\max} = \frac{\Delta E^2}{4Rm}, \tag{4}$$

where C is the total capacitance for one electrode|electrolyte interface, ΔE is the potential between the two oppositely charged electrodes (so-called cell potential), R is the series resistance of the capacitor and m is the mass of electrodes [10]. Thus, based on Eqs. (3) and (4), the cell potential is an important factor determining the exponential dependence of the specific energy and power density on ΔE for real EDLC under study. However, for real systems, due to mass-transfer limitations and non-ideal adsorption, there are deviations from the root dependence of $E_{\max}$ and $P_{\max}$ on ΔE.

The maximum cell potential for the supercapacitor is usually determined by the stability of the electrolyte. Aqueous electrolytes have good equivalent conductivities, high dielectric constants, low prices and they are considered as

environmentally friendly systems. However, they have a downside of a low maximum cell potential ($\Delta E \leq 1.23$V). Based on thermodynamics data, at cell potential 1.23 V the water molecules start to decompose. For higher cell potentials various non-aqueous electrolytes are used, which are based usually on aprotic non-aqueous solvents. In many supercapacitors, different organic solvents have been tested, however, in commercial EDLC mainly acetonitrile (AN) and propylene carbonate (PC) with dissolved quaternary ammonium salts as electrolytes are used. By applying organic solvents, the cell potential can be increased up to 3 V. However, the conductivities of these electrolytes are smaller (especially for PC based systems) and therefore the supercapacitors have larger internal resistance, decreasing nearly linearly the power density of the EDLC completed. It should be noted that the latter is also influenced by the electrical conductivity of the electrode material, resistances between the electrode and current collector and diffusion resistances resulting from the movement of ions within the small pores of the hierarchically porous electrode and in the porous polymer membrane separator [9,10,55–57].

4.2.1. Carbide derived carbon as an electrode material for supercapacitors

Based on the very high specific surface area, widely tunable microporosity, mesoporosity and macroporosity, the carbide derived carbons (CDC) are very attractive materials for high energy and power density supercapacitors. In addition the porous amorphous CDC carbon powders can be specially designed for high power and/or medium energy EDLC applications. Very inert (electrochemically redox inactive) and low density carbons for EDLC electrodes can be designed selecting raw organic polymers, aerogels as well as binary or ternary carbides as precursors [6,58,59]. Carefully treated carbons (reduced at high temperature with molecular H_2) are characterized with very wide region of ideal polarizability (up to 3.6 V) in very clean and dry (H_2O free) non-aqueous electrolyte solutions and aprotic ionic liquids (1-ethyl-3-methyl-imidazolium tetrafluoroborate ($EtMeImBF_4$) or 1-ethyl-3-methyl-imidazolium tetracyanoborate ($EtMeImB(CN)_4$)) [60]. Depending on the medium particle size of the carbon powder, very thin-layered carbon electrodes (thickness < 100 μm) can be prepared using very cheap and scalable rolling technology. However, noticeably thinner carbon electrodes can be prepared using different vacuum-spraying (including ultra-sound), magnetron sputtering or electrospinning methods [61]. Depending on the final application area, different binding materials (i.e., polymer solutions in organic and inorganic solvents) like polytetrafluoroethylene (PTFE) dispersion in H_2O, polyvinylidenedifluoride (PVDF) in dimethyl formamide or Nafion® in H_2O can be used for preparation of well-designed tunable electrodes. Depending on the surface conductivity of carbon powder used, sometimes graphite powders have been added into the raw carbon pastes to increase the electrical conductivity of the electrode layer [8,10,29].

4.3. Physical characterization techniques

4.3.1. Low temperature N_2 sorption measurements

Specially designed porous carbon materials have very high specific surface areas, which consists of a vast and complicated network of connected pores. According to IUPAC definitions, pores can be divided into three main classes: micropores – pore diameters below 2 nm, mesopores – pore diameters between 2 and 50 nm and macropores – pore diameters over 50 nm.

The quantitative relation between the amount of adsorbed gas and the equilibrium gas pressure (at constant reference pressure P_0 and constant temperature) is called the adsorption desorption isotherm. When the isotherm is presented as a graph, then from the shape of the isotherm, it is possible to estimate, what type the porosity (porous structure) of the material under study is. For example, based on the shape of the isotherms, it is possible to distinguish microporous, mesoporous and macroporous materials. Additionally, it is possible to determine the average pore geometry from the shape of the hysteresis of the sorption-desorption isotherm. In order to interpret the isotherms quantitatively and analyze the porous structure of the materials under study, additional models have been introduced and therefore the more complicated theories have been developed. The most used approximations are Brunauer-Emmet-Teller (BET), Langmuir, Dubinin-Radushkevich (D-R) and non-local density functional theory (NLDFT) models [62–66].

4.3.1.1. BET theory

To calculate the specific surface area, mainly the Brunauer-Emmet-Teller method is used [62,64]. The specific surface area can be calculated from the BET equation:

$$\frac{1}{W((p/p_0)-1)} = \frac{1}{W_m C_{\text{coe}}} + \frac{C_{\text{coe}}-1}{W_m C_{\text{coe}}}\left(\frac{p}{p_0}\right), \tag{5}$$

where W is the mass of the adsorbed gas at its relative pressure p/p_0, W_m is the mass of a monolayer of an adsorbed gas, C_{coe} is a coefficient constant related to the adsorption interaction energy existing between the monolayer molecules and the absorbent. To apply the BET equation, the plot $1/[W(p_0/p)\text{-}1]$ versus p/p_0 (so-called BET plot) must be linear. However, for most materials (in the case of N_2 adsorption) this is true within the p/p_0 range from 0.05 to 0.35, while in the case of microporous materials it is valid only up to 0.2. For the calculation of the surface area, the BET equation is generally applied at several different fixed p/p_0 points in the aforementioned pressure region. The mass of the adsorbed monolayer W_m can be expressed by the slope (Eq. 6) and intercept (Eq. 7) in the BET plot:

$$\text{slope} = \frac{C_{\text{coe}} - 1}{W_m C_{\text{coe}}}, \tag{6}$$

$$\text{intercept} = \frac{1}{W_{\text{m}} C_{\text{coe}}}. \tag{7}$$

Combining the last two equations, we can derive W_{m} as:

$$W_{\text{m}} = \frac{1}{\text{slope} + \text{intercept}}. \tag{8}$$

Next, from the W_m it is possible to calculate the BET specific surface area according to Eq. 9:

$$S_{\text{BET}} = \frac{W_{\text{m}} N_{\text{A}} A_{\text{CS}}}{M \cdot m}, \tag{9}$$

where N_{A} is the Avogadro constant, M is the molecular mass of the adsorbate, m is the mass of the sample and A_{CS} is the cross-section area of the adsorbate molecule (in the case of N_2 at 77 K, A_{CS} = 16.2 Å^2) [62,64].

4.3.1.2. Calculation of total pore volume and average pore radius

For the calculation of the total pore volume, the relative pressure of the gas used must be as close as possible to one. Then, it can be assumed that all the pores are filled with liquid N_2 adsorbate. If the material under study does not contain macropores then the isotherm is practically horizontal and approaches to a constant value, thus, the total pore volume is well defined. In the case of existing macropores, the slope of the isotherm increases sharply when the relative pressure approaches unity and consequently calculation of an exact value of total pore volume is more complex. From the amount of the absorbed nitrogen V_{ads}, the total pore volume is calculated according to Eq. 10:

$$V_{\text{t}} = \frac{P V_{\text{ads}} V_{\text{m}}}{RT}, \tag{10}$$

where P is the pressure, T is the temperature, R is the universal gas constant, and V_{m} is the molar volume of adsorbate (34.7 cm^3 mol^{-1} for N_2 at 77K) [67].

The average pore size r_{p} can be obtained from the total pore volume. Assuming that the pores have a cylindrical shape, r_{p} can be calculated according to Eq. 11:

$$r_p = \frac{2V_t}{S_{BET}}. \quad (11)$$

However, it should be noted that the shape of Eq. 11 depends on the geometry of the pores prevailing inside of the material studied.

4.3.1.3. The *t*-plot method

Applying the *t*-plot method, the adsorbed gas volume is plotted against the statistical thickness of the adsorbed layer t_{stat} (so-called *t*-plot). Thus, it is possible to obtain the external surface area, S_{ext}. The *t*-plot method uses higher relative pressures than the BET method, therefore taking into account mainly the meso- and macropores in the porous material. There are many empirical methods to calculate t_{stat} [68,69], however one of the mainly used approximations has been proposed by de Boer:

$$t_{stat} = \left[\frac{13.99}{\log(p/p_0) + 0.034} \right]^{1/2}. \quad (12)$$

For absorbents which, contains micropores, the *t*-plot usually deviates from a straight line at lower relative pressures. From the slope value *s*, calculated from the linear region of *t*-plot, it is possible to calculate S_{ext} for the adsorbent according to Eq. 13:

$$S_{ext} = 15.47s, \quad (13)$$

where the constant 15.47 is the density conversion factor if nitrogen is used. Consequently, the surface area contributed from micropores S_{micro} can be calculated according to Eq. 14:

$$S_{micro} = S_{BET} - S_t. \quad (14)$$

Thus, if the materials under study contain micropores, the volume of micropores V_{micro} can be approximated from the extrapolation of the high pressure linear region of *t*-plot to the V_{ads} axis. The intercept *i* is related to V_{micro} through a constant according to Eq. 15:

$$V_{micro} = 0.001547 \cdot i. \quad (15)$$

4.3.1.4. The non-local density functional theory (NLDFT)

One of the most accurate methods for describing the pore size distribution in micro-mesoporous materials is the non-local density functional theory (NLDFT). The shortfall of classical methods such as Dubinin-Radushkevich (DR), Barret-Joyner-Halenda (BJH) and Horvath-Kowazoe (HK) is that they do not describe accurately filling of the smaller micropores. NLDFT overcomes this difficulty and fills the gap between the molecular and macroscopic approaches [70–75].

NLDFT describes objectively the local liquid structure near the curved solid surfaces. The shape of the isotherm is determined by the intermolecular forces between the liquid-liquid and the liquid-solid interfaces. The relation between the shape of the isotherm and molecular forces can be described by the generalized adsorption isotherm (GAI):

$$N(P/P_0) = \int_{W_{\min}}^{W_{\max}} N(P/P_0, W) f(W) \mathrm{d}W \ , \tag{16}$$

where $N(P/P_0)$ is a point in the adsorption isotherm, W is the pore width, $N(P/P_0, W)$ is the corresponding point in the isotherm of the pore with width W and $f(W)$ is the pore size distribution function.

Eq. 16 assumes that the final isotherm consists from many individual isotherms for pores, which are multiplied by their distribution $f(W)$ relative to the total pore size distribution.

4.3.2. X-ray diffraction

Powder X-ray diffraction (XRD) and corresponding analysis is usually carried out to investigate the crystallographic structural changes in amorphous carbons and CDC that occur at different synthesis conditions applied. The XRD patterns for CDC usually show reflections corresponding to the graphite like basal plane (002) and edge (100)/(101) planes at 2θ equal to 26° and 43°, respectively. The (002) and (004) diffraction peaks correspond to the parallel graphene layers and the (100)/(101) peaks characterize the two-dimensional in-plane symmetry along the graphene layers [76–79].

Using the Scherrer equation, the mean crystallite sizes can be calculated according to:

$$L_{\mathrm{a;c}} = K\lambda / \beta \cos\theta \, , \tag{17}$$

where L_c and L_a are the estimated average crystallite sizes along the c- and a-directions of the graphitic structure, respectively; β is the full width at half-maximum (FWHM) of the reflections (after correcting for the instrumental broadening), θ is the position of a reflection and K is the X-ray wavelength of the beam used (for CuKα, K = 0.15406 nm) [76–82].

4.3.3. Raman spectroscopy

The first-order Raman spectra for perfectly ordered monocrystalline graphite show one peak at 1590 cm^{-1}, whereas disordered amorphous carbons generally demonstrate two peaks: the so-called graphite-like (G) peak at 1590 cm^{-1} and the disorder-induced (D) peak at 1350 cm^{-1}. The presence of D- and G-peaks, ratio of their intensities (I_D/I_G) and full width at half maximum (FWHM) values can be used to characterize the structure of an amorphous carbon under study. The G-peak corresponds to in-plane bond stretching motion of pairs of C atoms in sp^2 configuration with E_{2g} symmetry. Thus, this mode does not require the presence of six-fold C rings, and it occurs for all sp^2 sites, not only for those atoms located in the hexagonal graphene (ordered graphite) structure. The D-peak is a breathing mode with A_{1g} symmetry, which is forbidden in perfect graphite, and it only becomes active in the presence of some disorder in graphite structure [28,83–86].

Tuinstra and Koening noted [87] that the ratio of intensities of D- and G-peaks, i.e., I_D/I_G varied inversely with the in-plane correlation length L_a

$$L_a = 4.4\frac{I_G}{I_D} \tag{18}$$

The Tuinstra–Koening (T–K) method has been developed for analysis of the disordered graphite with unit sizes larger than 2 nm. Increasing the number of defects in carbon structure and reducing L_a below 2 nm, the number of ordered rings decreases and intensity of D-peak starts to decrease. However, the G-peak relates only to bond stretching of C atoms in sp^2 configuration, so G-peak retains its intensity, and the ratio of intensities of D- and G-peak decreases with increasing disorder in carbon structure and therefore the T–K equation is no longer valid. Thus, for more disordered carbons, the connection between L_a and the ratio of I_D/I_G is better described by the Ferrari–Robertson (F–R) relation [83,84]:

$$\frac{I_D}{I_G} = C'(\lambda){L_a}^2 \tag{19}$$

where $C'(\lambda)$ is a wavelength dependent parameter. At fixed λ = 514 nm, C' = 0.55. For small L_a, the intensity of D-peak is proportional to the probability of finding a six-fold ring in the carbon clusters area. Thus, in amorphous carbons, the development of a D-peak indicates some ordering, which is exactly the opposite to the case of graphite [88–90].

4.3.4. Transmission electron microscopy

Transmission electron microscopy (TEM) is a suitable method for morphological studies of carbon powders in the nanometer dimensions. An electron beam is guided through a very thin sample, usually less than 100 nm thick. The beam will partly scatter either losing or retaining its kinetic energy, depending on the physical (i.e., crystallographic and electronic) properties of the carbon sample measured. The elastically scattered electrons form a picture projection, the resolution of which is dependent on the spherical and chromatic abbreviations. The non-elastically scattered electrons are used in electron energy loss spectroscopy (EELS), characterizing the electronic structure and dielectric properties of the material under study. The electronic structure of carbon material is usually characterized by the ratio of carbon atoms in sp^3 and sp^2 electronic configurations. From the shape of the carbon K-edge adsorption spectrum, it is possible to estimate the ratio between sp^2 and sp^3 in the carbon sample under examination [91–94].

4.3.5. Scanning electron microscopy

Scanning electron microscopy (SEM) can also be used for analysis of changes in morphology in the carbon material under investigation. This is a very good method for qualitative visualization of macroscopic and mesoscopic structure of porous carbon electrode matrix under study [31]. Sometimes even plastificator (binder) nanowires can be clearly seen in the SEM images. Usually linear dimensions of the carbon particles forming the electrode layers can be obtained, thus, clearly visualized. SEM-EDX data will give some preliminary information characterizing the chemical composition of the electrode surface under study. SEM-EDX method, combined with FIB process, can be applied for the analysis of contamination processes taking place during the cell potential cycling conditions within very wide cell potential regions.

4.4. Electrochemical measurement techniques

For detailed electrochemical analysis of the electrode material properties, different electrochemical methods such as cyclic voltammetry (CV), constant current charge/discharge (CCCD) and electrochemical impedance spectroscopy (EIS) can be applied. Sometimes constant power charging/discharging (CPCD) test method has been applied for characterization of the single cell energy and power density (so-called Ragone plot) and other characteristics. It should be noted that for detailed analysis of the electrode materials and single cells, the three electrode and two electrode cell configurations, respectively, have been worked out and applied [10,95–97].

4.4.1. Cyclic voltammetry

During cyclic voltammetry (CV) measurements the cell potential (ΔE) is changed at a constant scan rate and the current density is measured. During the potential changes the current flowing through the system is registered. The cycle consists of both charging and discharging half-cycles and can be measured at different fixed scan rates. The measured current density (j) can be used for calculation of the medium so-called integral capacitance values according to Eq. 20:

$$C = jv^{-1}. \tag{20}$$

Eq. (20) is correct if the capacitance C is constant ($C \neq f(\Delta E)$) and if the series resistance $R_s \rightarrow 0$. Thus, Eq. (20) can be used to calculate the capacitance values only when R_s is very low and in the region of slow potential scan rates v, if the values of current measured for the EDLCs are very small. Thus, only under these conditions the potential drop (IR–drop) is negligible and the current response is essentially equal to that of a pure ideal capacitor. In a symmetrical two–electrode system the specific capacitance C_m (F g^{-1}) for one activated carbon electrode can be obtained as follows:

$$C_m = \frac{2C}{m}, \tag{21}$$

where m is the weight in g per one activated carbon electrode assuming that the positively and negatively charged electrodes have the same capacitance at fixed ΔE applied. It should be noted that this approach is sometimes not very exact if the specific adsorption of ions takes place at electrodes under study [95–97].

4.4.2. Constant current charge/discharge measurements

The charging and capacitances discharging of the cell can be calculated using the constant current charge/discharge (CCCD) cycle data. The capacitance of the cell C (F cm^{-2}) can be obtained from the slope of the discharge (or charge) curve according to Eq. (22):

$$C = j\frac{\mathrm{d}t}{\mathrm{d}(\Delta E)}, \tag{22}$$

where $\mathrm{d}t/\mathrm{d}(\Delta E)$ is the reciprocal value of the slope of the discharge or charge curve measured at corresponding constant current density j. This method is correct if there is a linear dependence between $\mathrm{d}t$ and $\mathrm{d}(\Delta E)$ applied. In the case of nonlinearity in $\mathrm{d}t/\mathrm{d}(\Delta E)$ (non-ideal capacitive, i.e., faradic behavior), these curves must be integrated to obtain the charge values accumulated and delivered.

The cycling efficiency, i.e., the so–called round trip coulombic efficiency (RTE) can be calculated as a ratio of capacitances measured, or applying the charge density values delivered or accumulated during discharging and charging steps of EDLCs under study.

From the CCCD curves, the value of internal resistance (R_{int}), can be calculated from the initial potential drop (*IR*–drop, usually vertical line area in CCCD) after changing the current direction. The *IR*-drop is measured usually at 10 ms after the current direction has been changed [97,98].

4.4.3. Impedance spectroscopy measurements

For more advanced and detailed characterization of EDLCs, the electrochemical impedance spectroscopy (EIS) is used. In EIS, an alternating voltage (av) input signal within a wide frequency *f* region (usually from 1mHz to 1kHz) is applied to the electrochemical device under study. The resulting alternating current (ac) current is registered and measured. Due to the fact that the many physical or chemical processes simultaneously taking place in charging or discharging of EDLCs have different time constants and give unalike responses to the input av, it is possible to separate and evaluate them independently. The main processes usually taking place are transport of electrons though the current collectors and electrode material, transport of ions through the electrolyte, transport of ions in the porous electrode and separator, double layer formation at the electrode|electrolyte interface [9,10,99–103].

The input signal of EIS is based on a modulation function:

$$E(t) = E_0 \sin(\omega t), \tag{23}$$

where E_0 is the maximum amplitude of the av signal, ω is the angular frequency and t is the time.

In the case of pure resistance, the following current response can be expressed as:

$$I(t) = I_0 \sin(\omega t), \tag{24}$$

where I_0 is the maximum current and there is no phase difference between $E(t)$ and $I(t)$. For a purely capacitive system, the current response can be expressed as:

$$I(t) = C\frac{\mathrm{d}E(t)}{\mathrm{d}t} = \omega C E_0 \cos(\omega t), \tag{25}$$

where C is the capacitance of the system. In the case of a purely capacitive system, the phase angle θ between the input av signal and resulting ac current is -90°. For further calculations we can rewrite Eqs. 23-25 as:

$$I = I_0 \, e^{\mathrm{i}\theta} e^{\mathrm{i}\omega t} = I(\mathrm{i}\omega) \, e^{\mathrm{i}\omega t} \tag{26}$$

and

$$E = E_0 \, e^{\mathrm{i}\theta} e^{\mathrm{i}\omega t} = I(\mathrm{i}\omega) \, e^{\mathrm{i}\omega t} = RI(\mathrm{i}\omega) \, e^{\mathrm{i}\omega t} + \frac{I(\mathrm{i}\omega) e^{\mathrm{i}\omega t}}{\mathrm{i}\omega C} \tag{27}$$

where i is the imaginary number $\mathrm{i} = \sqrt{-1}$, C is the total capacitance, R is the resistive resistance and $E(\mathrm{i}\omega)$ and $I(\mathrm{i}\omega)$ are voltage and current fasors arising from phase angle, respectively. The impedance Z of the system is defined according to:

$$Z(\omega) = \frac{E(\mathrm{i}\omega)}{\mathrm{i}(\mathrm{i}\omega)} = R(\omega) + \frac{1}{\mathrm{i}\omega C} = Z'(\omega) + \mathrm{i}Z''(\omega), \tag{28}$$

where $Z'(\omega)$ and $Z''(\omega)$ are the real part and the imaginary (so-called capacitive) part of the impedance, respectively [9,10,99,100,102,103].

For EDLC a resistive-capacitive circuit is commonly assumed. In this case it is possible to calculate the series resistance (R_s) as:

$$R_s = Z'(\omega), \tag{29}$$

the series capacitance C_s as:

$$C_s = -\frac{1}{\omega Z''(\omega)}, \tag{30}$$

the parallel resistance (R_p) as:

$$R_p = R_s \left(1 + \frac{1}{\tan^2\left(\frac{Z'(\omega)}{Z''(\omega)} \right)} \right), \tag{31}$$

and parallel capacitance (C_p) as:

$$C_{\mathrm{p}} = C_{\mathrm{s}}\left(1+\tan^2\left(\frac{Z'(\omega)}{Z''(\omega)}\right)\right), \tag{32}$$

It is possible to express C_s also in a complex form:

$$C_{\mathrm{s}}(\omega) = C(\omega) - \mathrm{i}C''(\omega), \tag{33}$$

where the real part (C'(ω)) of the capacitance is:

$$C'(\omega) = \frac{-Z(\omega)''}{\omega\left|Z(\omega)\right|^2}, \tag{34}$$

and the imaginary part of capacitance is:

$$C''(\omega) = \frac{-Z(\omega)'}{\omega\left|Z(\omega)\right|^2}. \tag{35}$$

The low frequency value of $C'(\omega)$ can be associated with the capacitance arising from the charging and discharging of the electric double layer. $C''(\omega)$, however corresponds to the energy dissipation connected with the irreversible faradaic charge transfer processes that can lead to some hysteresis of the electrochemical process [9,10,99,103].

To characterize further the EDLC properties, the complex power dependencies can be constructed. The value of complex power, $S(\omega)$, can be expressed as:

$$S(\omega) = P(\omega) + \mathrm{j}Q(\omega), \tag{36}$$

where the real part $P(\omega)$ of power is given as:

$$P(\omega) = \omega C''(\omega)\left|\Delta E_{\mathrm{rms}}\right|^2, \tag{37}$$

where ΔE_{rms} is the root mean square of the potential, and the imaginary part $Q(\omega)$ of power as:

$$Q(\omega) = -\omega C'(\omega)\left|\Delta E_{\mathrm{rms}}\right|^2, \tag{38}$$

$$\left|\Delta E_{\mathrm{rms}}\right|^2 = \frac{\Delta E_{\max}}{\sqrt{2}}, \tag{39}$$

where V_{max} is the maximum amplitude of ac voltage applied [9,10,99,103,104].

It should be noted that in the ideal cases of either pure capacitive or resistive behavior, the complex power equation (Eq. 36) simplifies since the real or imaginary part of the equation becomes zero, respectively. The ideal EDLCs balance between two states: resistive at very high frequencies ($\omega \to \infty$) and capacitive at very low frequencies ($\omega \to 0$). Between these two limits, the EDLC behaves like a resistance–capacitance (RC) circuit. When plotting both the real and imaginary part of power against frequency, the $P(\omega)$ and $Q(\omega)$ cross when the phase angle $\theta = -45°$. From the corresponding frequency f_R at the intersection point, it is possible to calculate the characteristic time constant τ_R for EDLC:

$$\tau_R = \frac{1}{2\pi f_R} \tag{40}$$

The value of τ_R gives the time needed for the release of half the maximum stored energy in the EDLC. Another possibility to obtain τ_R is to obtain f_R from C'' vs frequency plots as the C'' goes through a maximum at $f = f_R$ [10,99,100].

The maximal specific energy E_{max} (Wh kg^{-1}) and specific power P_{max} (kW kg^{-1}) for EDLCs studied can be estimated using Eqs. (3) and (4), where C is the capacitance of the cell in F cm^{-2}, R_E is the equivalent series resistance in Ω cm^2, obtained from Nyquist plot at ac $f \to \infty$, and m is the total active material weight of two electrodes (g cm^{-2}) [10,100,105].

4.4.4. Constant power measurements

The specific energy and power relationship, so-called Ragone plot, can be experimentally obtained from constant power tests. For correctly selected testing regimes the conditions resemble more real-life applications and can therefore give more adequate insight on the applicability of supercapacitor materials and electrolytes under development. Usually the constant power measurements are conducted for two electrode cell or for bigger EDLC completed. However, for better comparison, the energy and power densities are calculated taking into account the whole mass of two electrode cell (active material mass, binder and current collectors). Electrolyte and cell husk masses are usually not included into E and P calculations because these values depend noticeably on the cell configuration applied. The gravimetric power (kW kg^{-1}) and energy (Wh kg^{-1}) densities as well as the volumetric power (kW dm^{-3}) and energy (Wh dm^{-3}) densities are used [10,98,106].

5. EXPERIMENTAL

5.1. Synthesis of the carbide derived carbons

For the synthesis of CDC materials, a stationary bed furnace with quartz tubes was used. The reactor design and the chlorination technique has been reported previously [14,17,30]. The carbides chosen for the synthesis of CDC materials were titanium carbide (TiC, 99.5 % purity, − 325 mesh powder, Sigma-Aldrich) tungsten carbide (WC, 99 % purity, particle size <10 micron, Sigma-Aldrich) tantalum hafnium carbide (Ta_4HfC_5, 99.0 % purity, 45 micron powder, Goodfellow) and tungsten titanium carbide ($WTiC_2$, 99.5 % purity, 150 micron powder, Goodfellow). The raw carbides used were placed into a quartz stationary bed reactor and reacted with Cl_2 (AGA, 99.99 %), at chosen fixed reaction temperatures from 700 to 1100 °C. In the case of TiC, both Cl_2 and HCl (AGA, 99.99 %) were used as reactants. The flow rate of Cl_2 and HCl was fixed at 50 or 100 ml min^{-1}, respectively. The by-products were led away by the stream of excess Cl_2 or HCl, and after the reaction, the reactor was flushed with a slow stream of argon to remove the excess of residues and gaseous by-products from the carbon formed. During heating and cooling steps, the reactor was flushed with a flow of argon (400 ml min^{-1} for TiC, Ta_4HfC_5 and $WTiC_2$, 500 ml min^{-1} for WC). The resulting carbon powder was thereafter treated with H_2 (TiC, Ta_4HfC_5 and $WTiC_2$) or H_2/Ar (1:4) mixture (WC) at 800 °C during 1.5 h to dechlorinate thoroughly the CDC powder as well as to remove the residual chlorides and oxygen-containing functional groups from the surface of the porous carbon under study [21,107–109].

The extent of conversion ϖ was calculated as:

$$\varpi = \frac{m_i - m_f}{(1-\chi)\times m_i}\times 100\%, \tag{41}$$

where m_i and m_f are the initial and final weights of the sample, respectively, and χ is the mass fraction of carbon in the carbide [37,107].

It should be noted that for WC, $WTiC_2$ and Ta_4HfC_5, the lowest synthesis temperature was 800 °C. This is due to extremely prolonged chlorination process needed caused by the non-linearity of CDC conversion in time probably caused by mixed synthesis/decomposition kinetics. At T_{synth} = 700 °C, conversion of carbides to carbon was incomplete and extent of conversion more than 90 % was not achieved. The exception to this was TiC, which reacted with both Cl_2 and HCl even at 700 °C. Somewhat surprisingly, it was not possible to achieve the extent of reaction higher than 90 % for $WTiC_2$-CDC, synthesized at T_{synth} = 1100 °C. The conducted analysis shows that this is probably due to tight graphite cages forming around the carbide particles, thus, preventing further reaction of Cl_2 with the $WTiC_2$, left inside of the partially reacted carbon particles.

5.2. Physical characterization of TiC-CDC, WC-CDC, Ta_4HfC_5-CDC and $WTiC_2$-CDC powders

5.2.1. XRD and Raman spectroscopy data of CDC powders

XRD analysis of the CDC powder samples was carried out to investigate the structural changes in TiC-CDC that occurred, applying different etching agents at different reaction temperatures. The XRD patterns of all synthesized CDCs showed reflections corresponding to the graphitic basal (002) and (100)/(101) edge planes at $2\theta \sim 26^{\circ}$ and $\sim 43^{\circ}$, respectively. The (002) diffraction peak at $2\theta \sim 26°$, corresponds to parallel graphene layers, while the (100)/(101) diffraction peak at $2\theta \sim 43°$ characterizes the 2D in-plane symmetry along the graphene layers.

The XRD patterns of the synthesized materials were obtained on a Bruker D8 diffractometer (Bruker Corporation) using CuKα radiation with a step size of 0.01° and counting time of 2 s using position sensitive LynxEye detector. The diffraction spectra were recorded at 25 °C and reflections on measured patterns were fitted using the AXES 2.5 code using modified Lorentzian model for all reflections.

In Raman spectroscopy data analysis the presence of D- and G-peaks, ratio of their intensities and full width at half-maximum (FWHM) values has been used to characterize the structure of the mainly amorphous carbon. Raman spectroscopy of all synthesized CDCs show the first-order Raman spectra of the so-called graphite-like (G) peak at ~ 1587 cm^{-1} and the disorder-induced (D) peak at ~ 1348 cm^{-1}.

The Raman spectra were recorded by applying the Renishaw inVia micro-Raman spectrometer using Ar laser excitation (λ = 514 nm). The data were modeled fitting the Lorentzian curves to the G- and D-band using Origin Pro 8 software.

5.2.1.1. Analysis of TiC-CDC powders

As the reaction temperature of TiC-CDC increases from 700 to 1100 °C, the (002) peak becomes narrower (Figure 1), indicating intensification of the ordering processes on the surface of the mainly amorphous CDC. Comparison of the XRD patterns for Cl_2 treated TiC-CDC(Cl_2) and HCl treated TiC-CDC(HCl) materials shows that TiC-CDC(HCl) carbons are more ordered as evident from the shape of (002) and (100)/(101) more intense and narrower peaks. In addition, TiC-CDC(HCl) materials, synthesized at lower temperatures ($T \leq 800$ °C) contain some traces of initial titanium carbide.

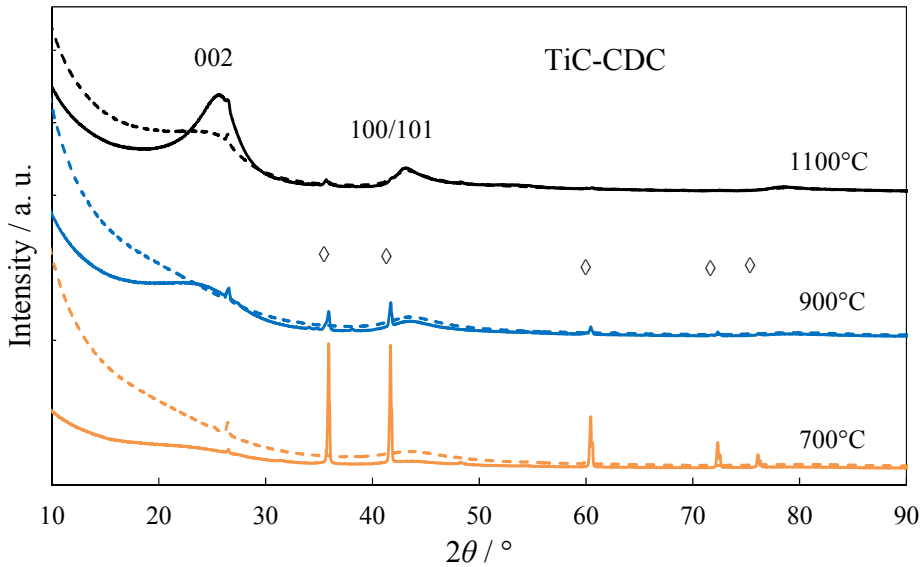

Figure 1. Characteristic XRD patterns for porous TiC-CDC prepared by using different reactants (dashed line denotes Cl_2, solid line denotes HCl) at different reaction temperatures (given in the figure). Diamonds denote crystallographic reflections of residual TiC.

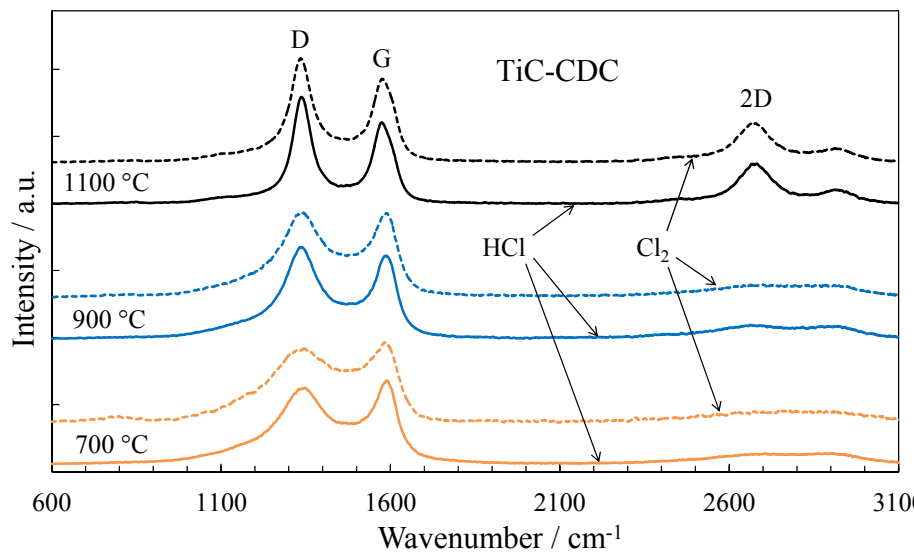

Figure 2. Raman spectra of porous TiC-CDC prepared by using Cl_2 and HCl as reactants at different reaction temperatures (given in the figure).

Raman spectroscopy data (Figure 2) also indicate that as the reaction temperature for TiC-CDC increased from 700 to 1100 °C, amorphous CDC becomes more ordered, evident from a decrease in full width at half-maximum (FWHM) values of the D- and G-bands. According to the data in Table 1, very small narrowing of the G-band takes place indicating the beginning of graphitization of porous CDCs.

As the chlorination temperature increases the crystallite size also slightly increases indicating some ordering of the amorphous CDC structure with temperature.

Table 1. Raman analysis of TiC-CDCs.

Reactant	Synthesis temperature (°C)	D-peak FWHM (cm^{-1})	G-peak FWHM (cm^{-1})	I_D/I_G	L_a (nm)
HCl	700	205	76	0.96	1.32
HCl	800	180	75	1.03	1.37
HCl	900	154	74	1.08	1.40
HCl	1000	97	75	1.34	1.56
HCl	1100	73	72	1.32	1.55
Cl_2	700	240	89	1.08	1.40
Cl_2	800	205	80	0.99	1.34
Cl_2	900	185	79	1.03	1.37
Cl_2	1000	109	78	1.24	1.50
Cl_2	1100	87	75	1.22	1.49

5.2.1.2. Analysis of WC-CDC powders prepared

The XRD patterns for WC-CDC (Figure 3) showed largely diffused reflections corresponding to the graphite-like basal (002) and (100)/(101) planes at 2θ ~26º and ~43º, respectively. However, surprisingly, as the chlorination temperature of tungsten carbide increased from 800 °C to 1100 °C, the intensities of (002) and (100)/(101) peaks were practically same and only very slight increase in intensities was observed (Figure 3a), indicating initiation of the very weak ordering processes in the mainly amorphous carbon.

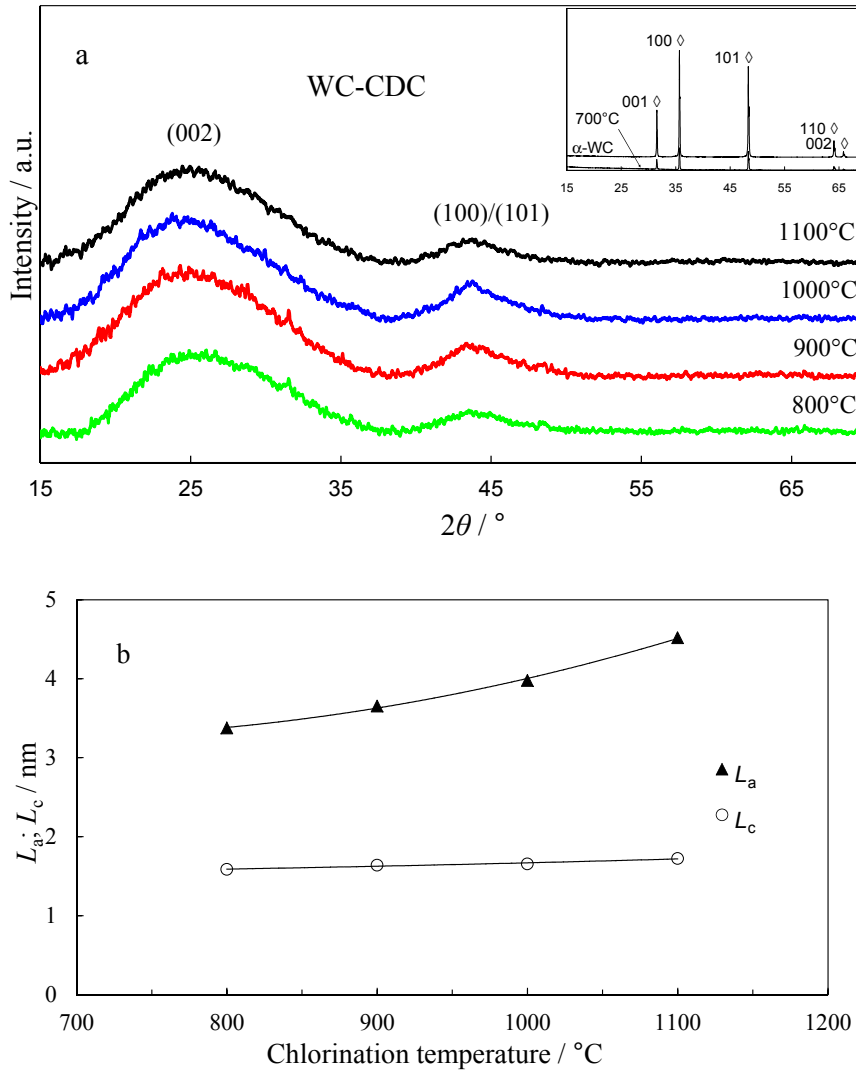

Figure 3. Characteristic XRD patterns for porous WC-CDC prepared at various chlorination temperatures (◊ – hollow triangles corresponding to the initial tungsten carbide reflections) (a) and apparent crystallite size L_a(L_c) along the a(c)-directions of the graphite structure vs. chlorination temperature (b).

It can be seen in Figure 3b, that for WC-CDC, prepared at from T_{synth} = 800 °C to T_{synth} = 1100 °C, L_a and L_c are practically independent of the synthesis temperature and only slightly increase with the synthesis temperature applied. Considering that for the regular graphite structure c = 0.6708 nm and a = 0.2461 nm, the magnitudes of L_c and L_a obtained yield that the carbon structures consist of graphitic crystallites of about 2 graphite cell lengths along the c-direction (obtained from the (100) peak shape) and about 16 cell lengths along the a-

direction (obtained from the (100) peak shape). The Raman spectra for WC-CDCs, in addition to the G- and D-peaks also show the second-order peak of D-band (2D) at ~ 2700 cm^{-1} (Figure 4a). The appearance and increase of 2D peak for WC-CDCs synthesized at $T_{synth} \geq 1000$ °C, compared with $T_{synth} = 800$ °C, is related to the three-dimensional ordering of the graphitic structure. In accordance with data in Figure 4b, as the chlorination temperature for tungsten carbide increases from 800 to 1100 °C, amorphous WC-CDC became more ordered as evident from the increase in L_a values. According to the data, some ordering of porous, mainly amorphous, WC-CDC structure takes place already at moderate $T_{synth} \geq 900$ °C temperatures.

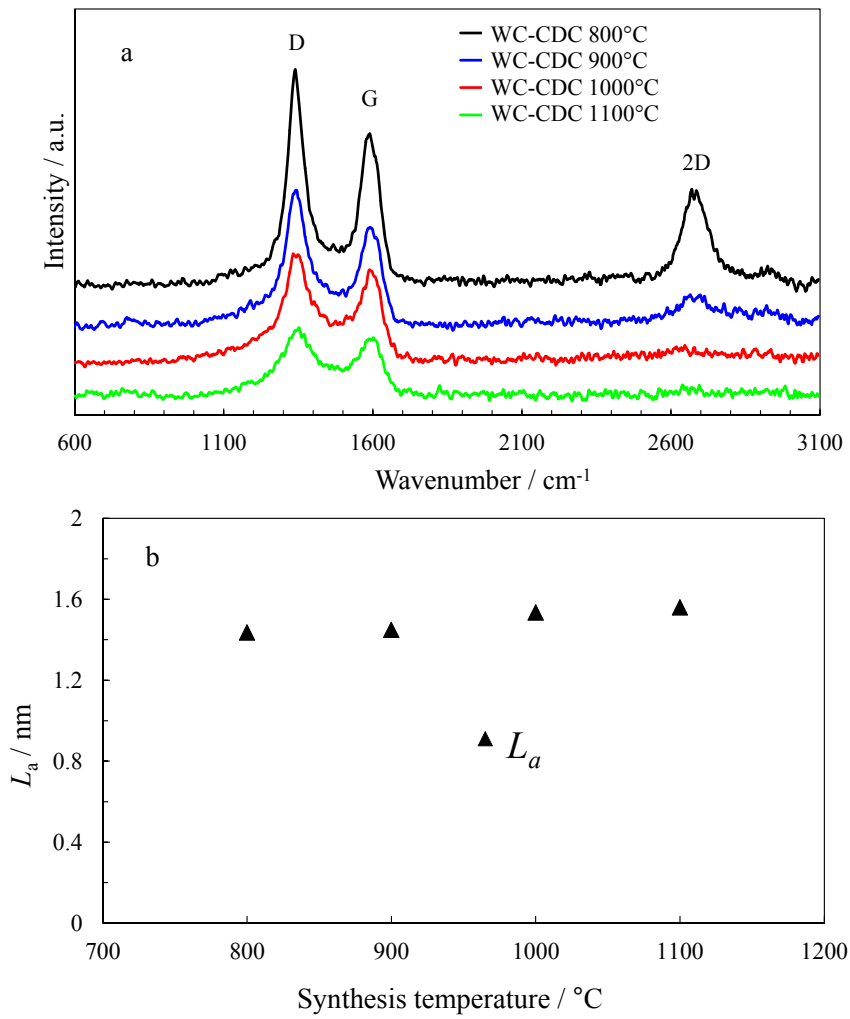

Figure 4. Raman spectra for WC-CDC powders prepared at various chlorination temperatures (a) and apparent crystallite size L_a (calculated according to the Ferrari–Robertson equation) vs. chlorination temperature (b).

5.2.1.3. Analysis of Ta_4HfC_5-CDC and $WTiC_2$-CDC powders

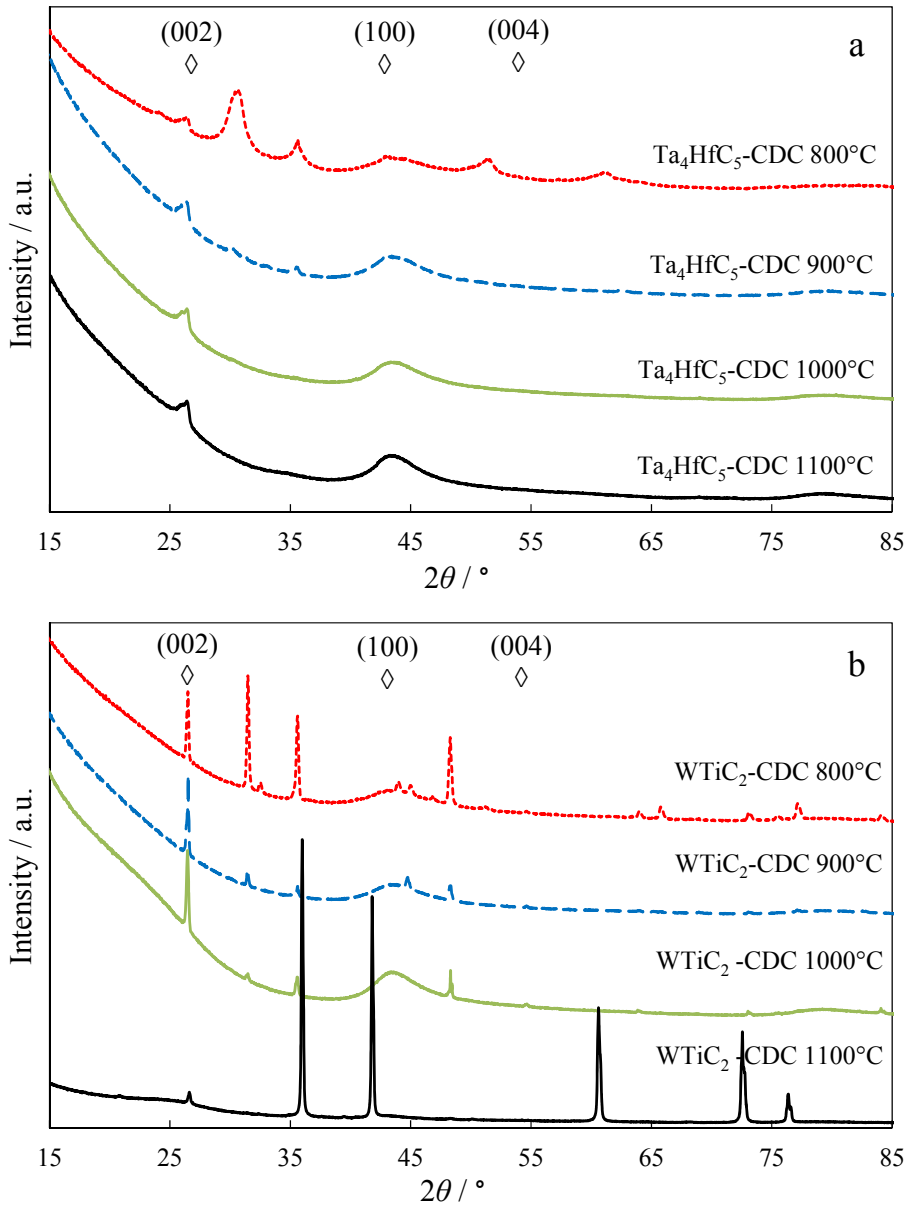

Figure 5. Characteristic XRD patterns for porous Ta_4HfC_5-CDC (a) and $WTiC_2$-CDC (b), synthesized at various chlorination temperatures (rhombic marks denote the graphite plane reflections, given with corresponding indexes).

In addition to the diffraction peaks associated with CDC-like carbon, we can detect some peaks originated from the initial unreacted carbide, indicating that the extent of reaction from carbide to CDC was not 100% for some CDC powders prepared. This was the case for Ta_4HfC_5-CDC, synthesized at lower temperatures ($T_{synth} \leq 900$ °C) (Figure 5a). However, surprisingly, there are traces of initial ternary carbide detectable also for CDC synthesized from $WTiC_2$ at $T_{synth} = 1100$ °C (Figure 5b). Based on the analysis of the XRD data, these peaks can be associated to WC synthesized from $WTiC_2$ at lower temperatures ($T_{synth} \leq 900$ °C) and TiC synthesized from $WTiC_2$ at 1100 °C, respectively. The explanations for these results are that the raw $WTiC_2$ consists of both TiC and WC particles and at lower synthesis temperatures TiC reacts with chlorine more easily than WC and therefore some traces of WC are left in the CDC. However, at 1100 °C, it is possible that the tight nanocage-like graphitic structure has been formed around some larger carbide particles and therefore, preventing the further reaction of the residual TiC (or WC) to CDC. Thus, blocking the full transformation of $WTiC_2$ to CDC, even at 1100 °C. In addition it should be noted, that since TiC gives diffraction peaks with much higher intensity than WC, it is impossible to distinguish, whether the carbide left in the CDC particles is TiC or $WTiC_2$.

The medium diameter of the graphitic particles, L_a, has been calculated from XRD data based on the Rietfeld approximation, and the L_a values are given in Figure 6. These data demonstrate that L_a increases with CDC synthesis temperature and L_a only slightly depends on the initial ternary carbide used.

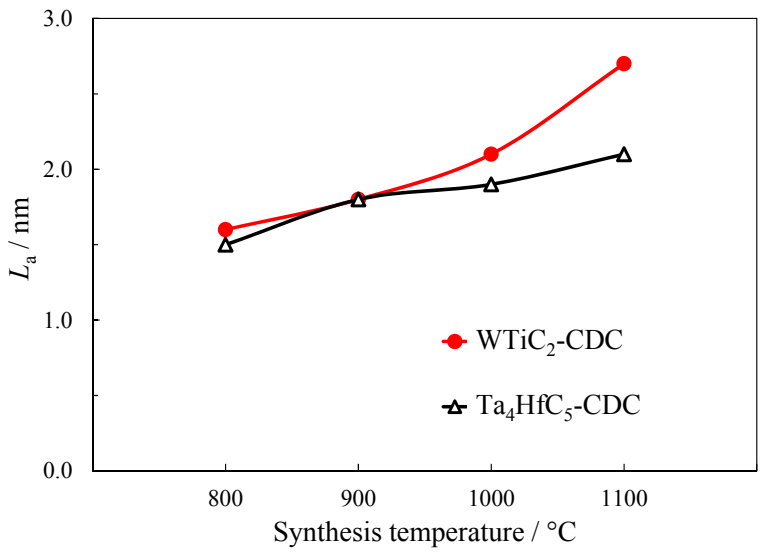

Figure 6. The apparent crystallite size L_a vs. chlorination temperature plots, calculated from XRD measurements data, for porous Ta_4HfC_5-CDC and $WTiC_2$-CDC.

Raman spectroscopy data, given in Figure 7, indicate that as the reaction temperature for Ta_4HfC_5-CDC increased from 800 to 1100 °C, the amorphous CDC became more ordered as evident from narrowing of the G- and D-peaks, in agreement with increasing 2D peak intensities. The same trends have been established also for $WTiC_2$-CDC.

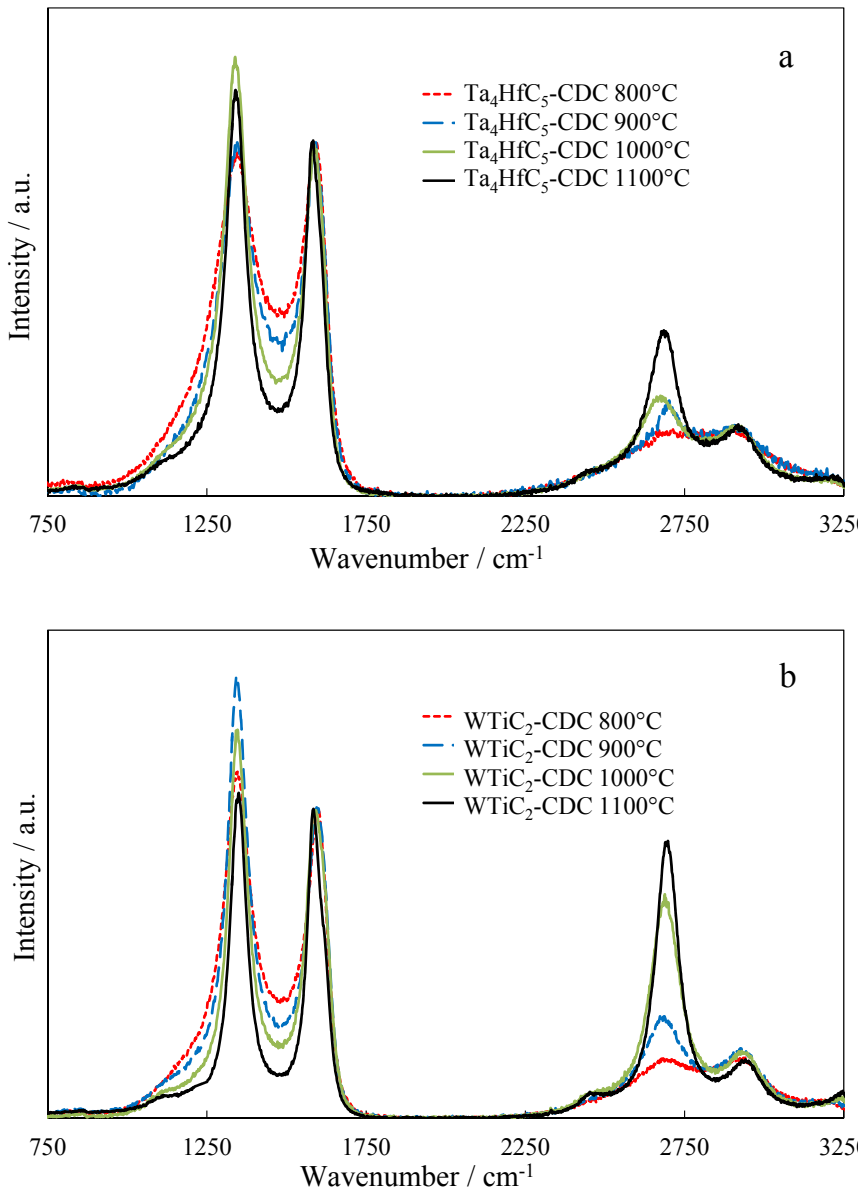

Figure 7. Characteristic Raman spectra for porous Ta_4HfC_5-CDC (a) and $WTiC_2$-CDC (b), synthesized at various chlorination temperatures.

The calculated crystallite sizes are shown in Figure 8. It can be seen, that in an agreement with XRD data, with the increase of the synthesis temperature, the noticeable increase of graphitic particle grains (areas) takes place. CDCs prepared from $WTiC_2$ have slightly larger crystallite sizes than CDC materials prepared from Ta_4HfC_5.

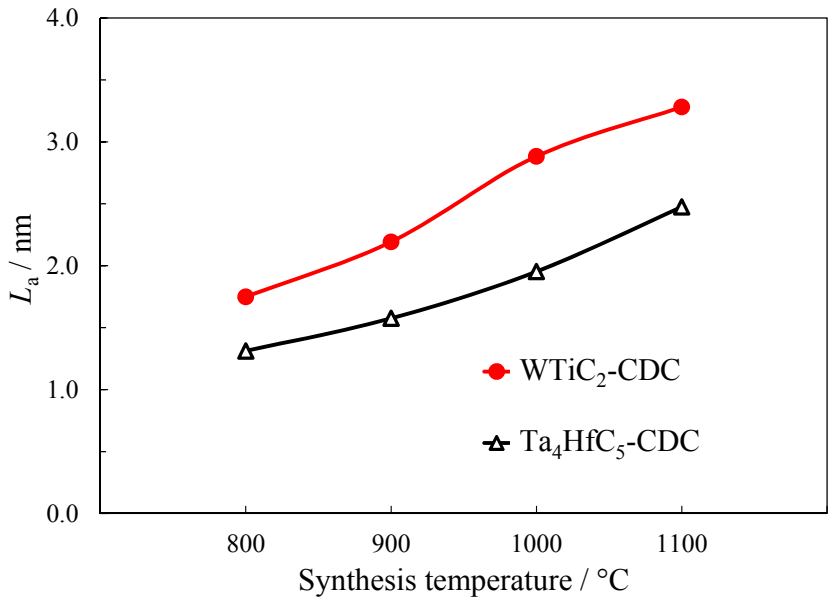

Figure 8. The apparent crystallite size L_a vs. chlorination temperature plots, calculated from Raman spectroscopy data, for porous Ta_4HfC_5-CDC and $WTiC_2$-CDC.

5.2.2. Surface area and pore size distribution measurements of CDC powders

The porous structure of CDC, prepared from TiC, WC, $WTiC_2$ and Ta_4HfC_5 was characterized using low-temperature nitrogen sorption method. The N_2 sorption experiments were performed at the boiling temperature of liquid nitrogen (−195.8 °C) using the ASAP 2020 system (Micromeritics). The specific surface area S_{BET} and other parameters for porous CDC carbon materials were calculated according to BET and DFT theories, at relative nitrogen pressure (P/P_0) up to 0.2. The total volume of pores (V_{tot}) was obtained at the conditions near to saturation pressure p/p_0 = 0.995. Micropore area (S_{micro}) and micropore volume (V_{micro}) were calculated using *t*-plot method. The pore size distributions plots were determined using NLDFT and the so-called slit-shaped pores model.

The summarized data of N_2 sorption measurements are given in Table 2.

Table 2. Results of sorption measurements of different CDCs prepared at different temperatures.

Carbon material	Chlorination temperature (°C)	S_{BET} (m^2 g^{-1})	T_{plot} micro-pore area (m^2 g^{-1})	T_{plot} micro-pore volume (cm^3 g^{-1})	Total pore volume (cm^3 g^{-1})
TiC-CDC(HCl)	700	1085	1073	0.50	0.54
	800	1214	1180	0.57	0.66
	900	1170	1131	0.61	0.73
	1000	1087	1009	0.68	0.88
	1100	874	765	0.70	0.96
TiC-CDC(Cl_2)	700	1320	1300	0.59	0.69
	800	1443	1418	0.64	0.77
	900	1544	1503	0.71	0.87
	1000	1538	1489	0.71	0.88
	1100	1448	1377	0.81	1.01
WC-CDC	800	1270	1260	0.56	0.59
	900	1290	1280	0.60	0.64
	1000	1280	1260	0.61	0.66
	1100	1580	1550	0.83	0.89
Ta_4HfC_5-CDC	800	1810	1780	0.79	0.85
	900	1780	1760	0.81	0.85
	1000	1990	1960	0.91	0.88
	1100	1980	1950	0.95	1.01
$WTiC_2$-CDC	800	1640	1630	0.72	0.74
	900	1840	1830	0.83	0.85
	1000	1880	1860	0.84	0.88
	1100	360	350	0.19	0.21

5.2.2.1. Porosity characteristics for TiC-CDC powders

According to the data, given in Table 2, TiC-CDC materials synthesized have micro-mesoporous structure and the specific surface areas up to 1210 m^2 g^{-1} for TiC-CDC(HCl) synthesized at T_{synth} = 800 °C and S_{BET} = 1540 m^2 g^{-1} for TiC-CDC(Cl_2), synthesized at T_{synth} = 900 °C, were obtained, respectively. The total amount of nitrogen adsorbed increases with the synthesis temperature, having a maximal value of 1.01 cm^3 g^{-1} for TiC-CDC(Cl_2) and 0.70 cm^3 g^{-1} for TiC-CDC(HCl) synthesized at T_{synth} = 1100 °C. However, surprisingly, the S_{BET} values did not change in the same direction. This is probably caused by the increase of percentage of larger mesopores in porous TiC-CDC material with increasing the synthesis temperature applied.

5.2.2.2. Porosity characteristics for WC-CDC powders

The N_2 sorption isotherms, given in Figure 9 for porous WC-CDC, prepared at temperature $T_{synth} \leq 900$ °C, show that the sorption data can be approximated by the isotherm of *type I* according to the Brunauer classification, characteristic of the microporous material structure with the medium pore size less than 2 nm.

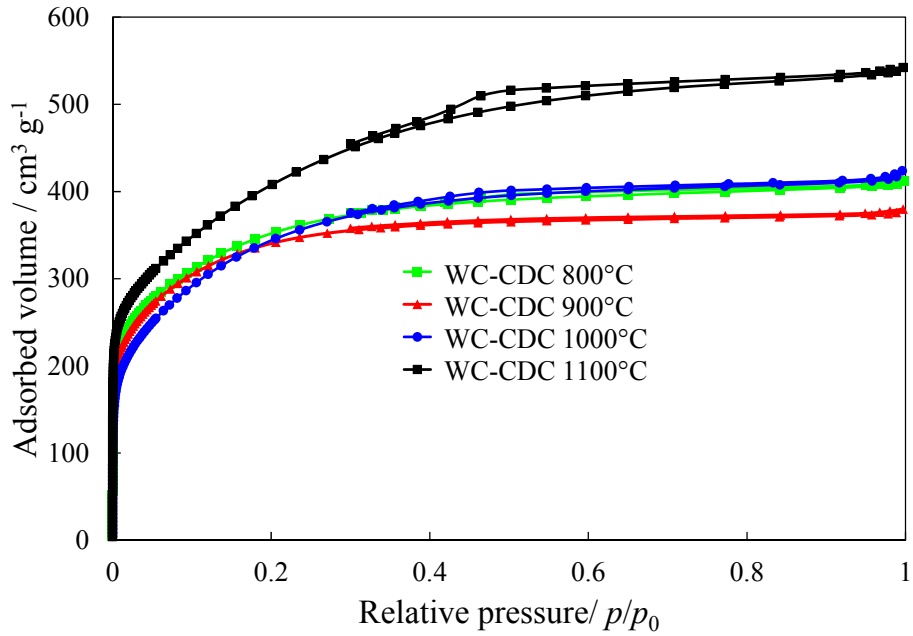

Figure 9. Low-temperature N_2 adsorption/desorption isotherms for WC-CDC prepared at various chlorination temperatures.

The adsorption/desorption isotherms for WC-CDC synthesized at higher temperatures $T_{synth} \geq 1000$ °C can be approximated to the *type IV* isotherm with *H4 type* hysteresis, caused by the capillary condensation of nitrogen in mesopores, determining the steep slope at higher relative pressures p/p_0. The hysteresis associated with *type IV* isotherm correlates with the narrowing of G-band and D-band peaks and formation of the 2D peak in Raman spectra caused by the beginning of ordering (graphitization) and by the development of mesopores into WC-CDC powders at higher temperatures.

Calculated pore size distributions are given in Figure 10. According to the data in Table 2, WC-CDC materials synthesized are mainly microporous, but small increase in mesopores area with increasing synthesis temperature can be observed.

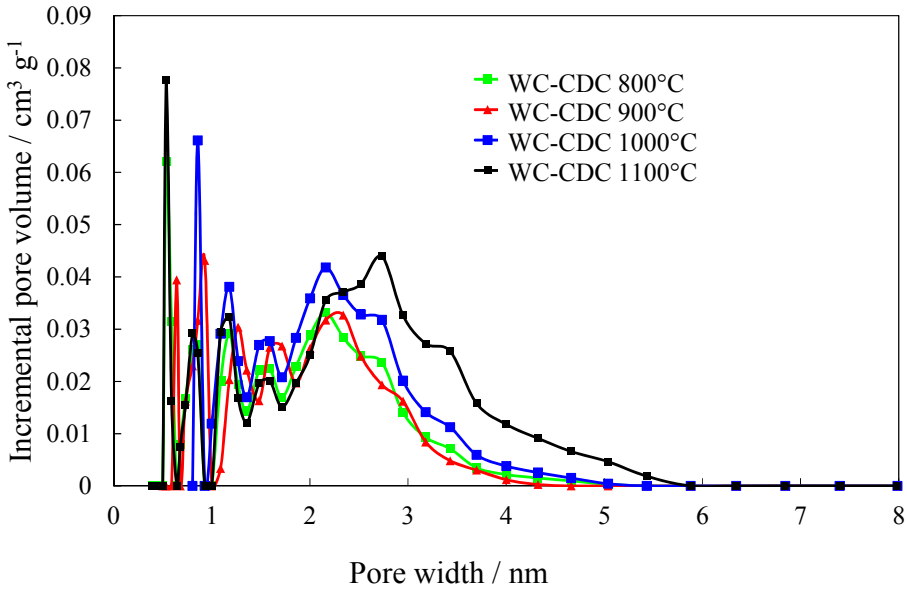

Figure 10. Incremental pore size distribution vs. pore width plots obtained using NLDFT method for WC-CDC prepared at various chlorination temperatures.

The total amount of N_2 adsorbed increases with the chlorination temperature, having maximal value 0.89 cm^3 g^{-1} for WC-CDC synthesized at 1100 °C. The specific surface area values change in the same direction and relatively high value 1580 m^2 g^{-1} for WC-CDC synthesized at 1100 °C has been established. Thus, substantial increase in pore volume and specific surface area values for WC-CDC materials synthesized in the temperature range from 1000 °C to 1100 °C has been observed, probably caused mainly by increase of ordering and opening of the smaller pores, i.e., by the development of pores accessible for nitrogen adsorption. The pore size distribution plots in Figure 10 have nearly similar shapes. However, some development of larger pores with increasing synthesis temperatures has been established.

5.2.2.3. Porosity characteristics for Ta_4HfC_5-CDC and $WTiC_2$-CDC powders

The porous structure characteristics for Ta_4HfC_5-CDC and $WTiC_2$-CDC are given in Figures 11 and 12 and Table 2.

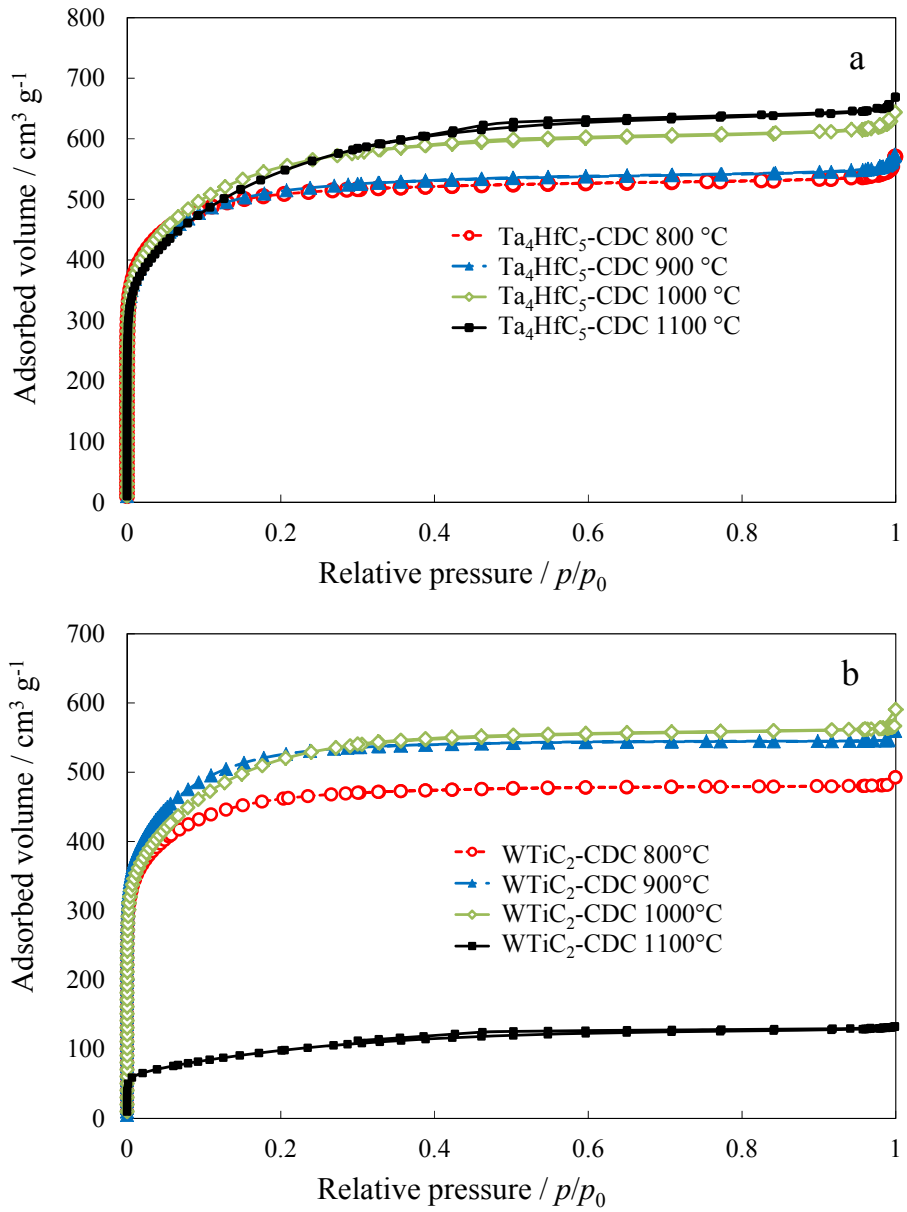

Figure 11. Low-temperature N_2 adsorption/desorption isotherms for Ta_4HfC_5-CDC (a) and $WTiC_2$-CDC (b), synthesized at various chlorination temperatures.

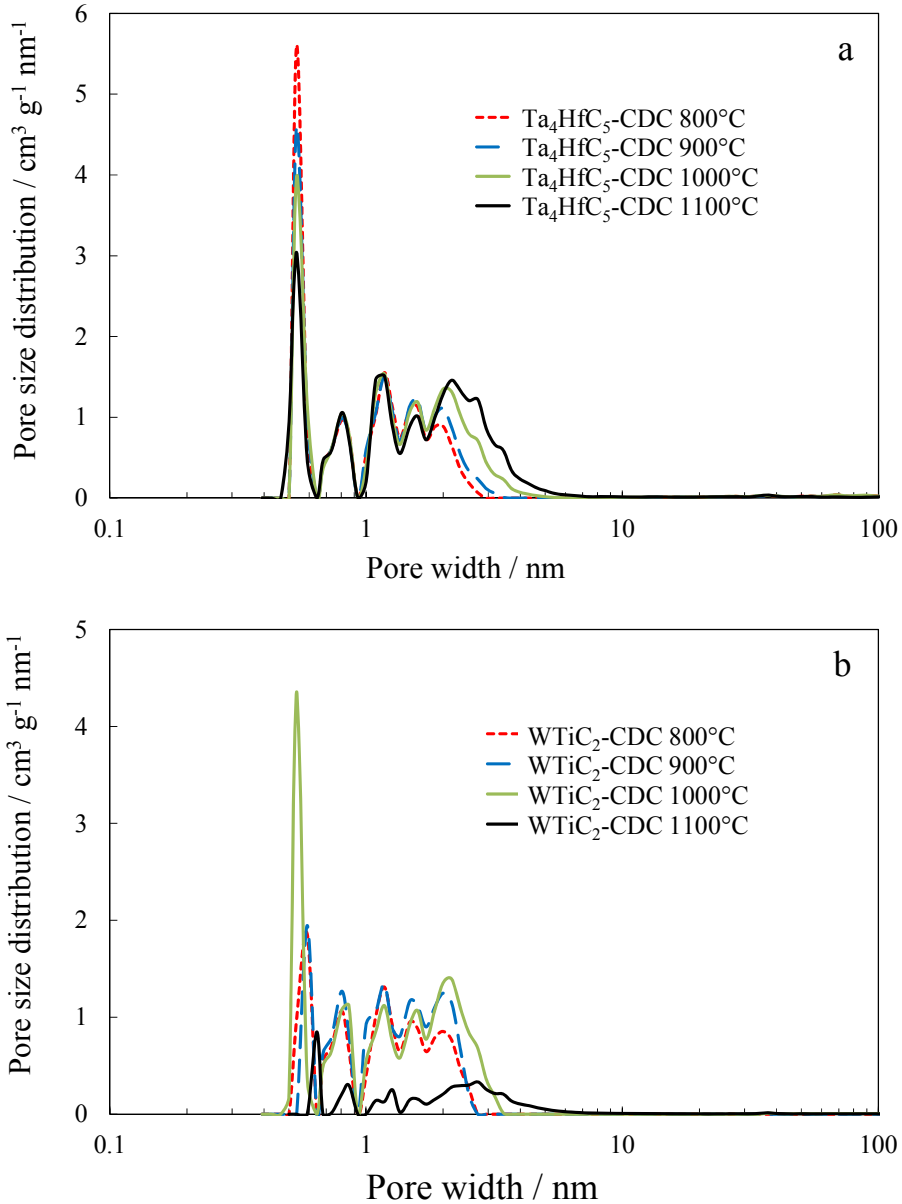

Figure 12. Differential pore size distribution vs. pore width plots, obtained using the NLDFT method for Ta_4HfC_5-CDC (a) and $WTiC_2$-CDC (b), synthesized at various chlorination temperatures.

According to the data in Table 2, the materials synthesized have the complicated hierarchical micro-mesoporous structure. The specific surface area up to 1990 m^2 g^{-1} for Ta_4HfC_5-CDC, synthesized at T_{synth} = 1000 °C, and S_{BET} = 1880 m^2 g^{-1} for $WTiC_2$-CDC, synthesized at T_{synth} = 1000 °C, were

obtained. Thus, compared to the previously studied TiC-CDC, the CDCs prepared from ternary carbides under study demonstrate higher specific surface areas and higher degree of mesoporosity, desirable for supercapacitor applications. The total amount of nitrogen adsorbed and hence, the total pore volume, increases with the reaction temperature, having a maximal value of 0.95 cm^3 g^{-1} for Ta_4HfC_5-CDC (T_{synth} = 1100 °C) and 0.84 cm^3 g^{-1} for $WTiC_2$-CDC (T_{synth} = 1000 °C), respectively. The somewhat lower S_{BET}, V_{pore}, S_{micro} and etc., values obtained for $WTiC_2$-CDC, synthesized at T_{synth} = 1100 °C, are probably due to the unreacted carbide inside the CDC particles observed using XRD analysis method.

5.2.3. HRTEM. and SEM analysis of the carbon powders under study

For the morphological studies, the CDC were examined using HRTEM on a Tecnai 12 instrument operated at the 120 kV accelerating voltage. TEM specimens were prepared from ultrasonic dispersions of the corresponding samples in 1-butanol. One drop of each suspension was deposited onto a copper grid covered with a holey carbon film.

To investigate further the morphological changes that occurred during the synthesis, the scanning electron microscopy (SEM) images were taken of the synthesized materials. For the measurements HeliosTM Nanolab 600 system was used.

5.2.3.1. HRTEM analysis of TiC-CDC powders

HRTEM studies of TiC-CDC formed at various reaction temperatures revealed the microstructure at the atomic scale. Reaction with Cl_2 and HCl at 700 °C results in a formation of completely amorphous carbon (Figure 13). Some ordering of carbon and formation of graphitic structures starts at $T_{synth} \geq 900$ °C. However, only at 900 °C and above, both Raman spectroscopy and XRD detected increased ordering of mainly amorphous carbon. In a good agreement with XRD data, a HRTEM micrograph of a sample processed at T_{synth} = 1100 °C shows clearly a network of well-ordered graphitic sheets (mainly at the surface) within amorphous TiC-CDC carbon particles.

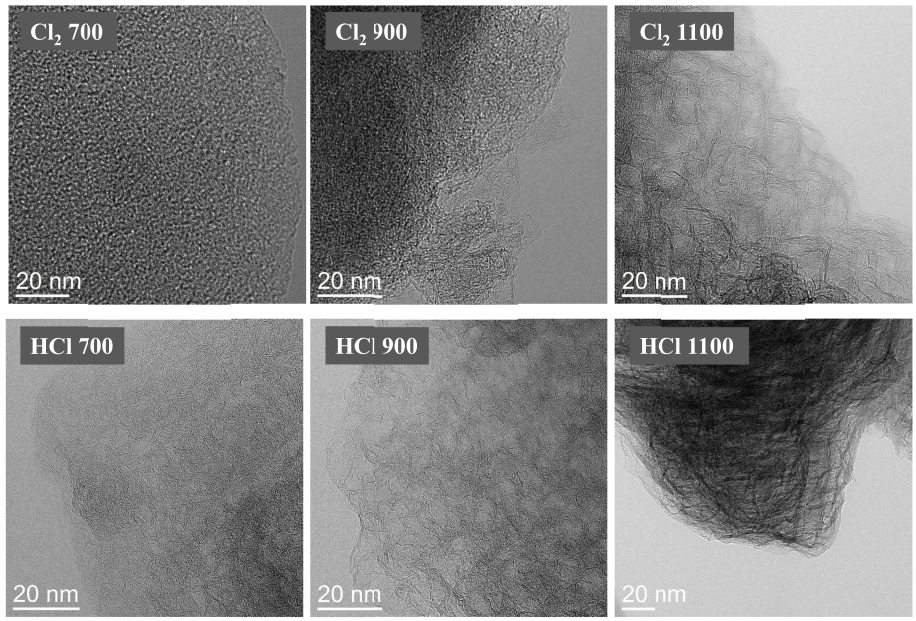

Figure 13. HRTEM images for porous TiC-CDC prepared by using Cl_2 and HCl as reactants at different reaction temperatures (given in the figure).

5.2.3.2. HRTEM analysis of WC-CDC powders

HRTEM micrographs of the WC-CDC sample prepared at 800 °C reveal that the sample consists of mostly amorphous carbon (Figure 14a). The HRTEM images are supported by the diffused diffraction rings of the selected-area electron diffraction (SAED) pattern (Figure 14b). The energy loss near edge structure (ELNES) of the carbon-K ionization edge presents the characteristic π* and σ* peaks of carbon, as it can be seen in Figure 14c. The ELNES spectrum has two characteristic features: the 1s → π* transition peak at ~ 286 eV and 1s → σ* transition peak occurring at ~ 296 eV. In this case, the featureless and wide (flat) σ* peak is indicative of the low crystallinity of the particle, in agreement with the HRTEM information.

HRTEM micrograph of a graphene-like WC-CDC (Figure 15a) particle from the sample prepared at 1100 °C reveal the existence of a somewhat ordered graphitic particle areas in the sample. Their nanostructure consists of graphitic agglomerates that are intergrown in a disordered fashion, as it is displayed in Figure 15a. The ELNES of the carbon-K ionization edge presents the characteristic π* and σ* peaks of graphite-like carbons, as it can be seen in Figure 15c. For the sample prepared at 1100 °C the 1s → π* peak becomes more narrow, while the height of the peak increases, which is in an agreement with the more ordered structure of CDC, based on the HRTEM images, XRD and Raman spectroscopy data. The SAED pattern displays *hk*0-type diffraction rings of

graphite (Figure 15b), which are consistent with a nanostructure consisting of poorly-stacked graphene layers as previously stated. Thus, the EEL spectra of the carbon-K ionization edge, analyzed in this work, give important information about the bonding nature and the crystallinity of the material under study.

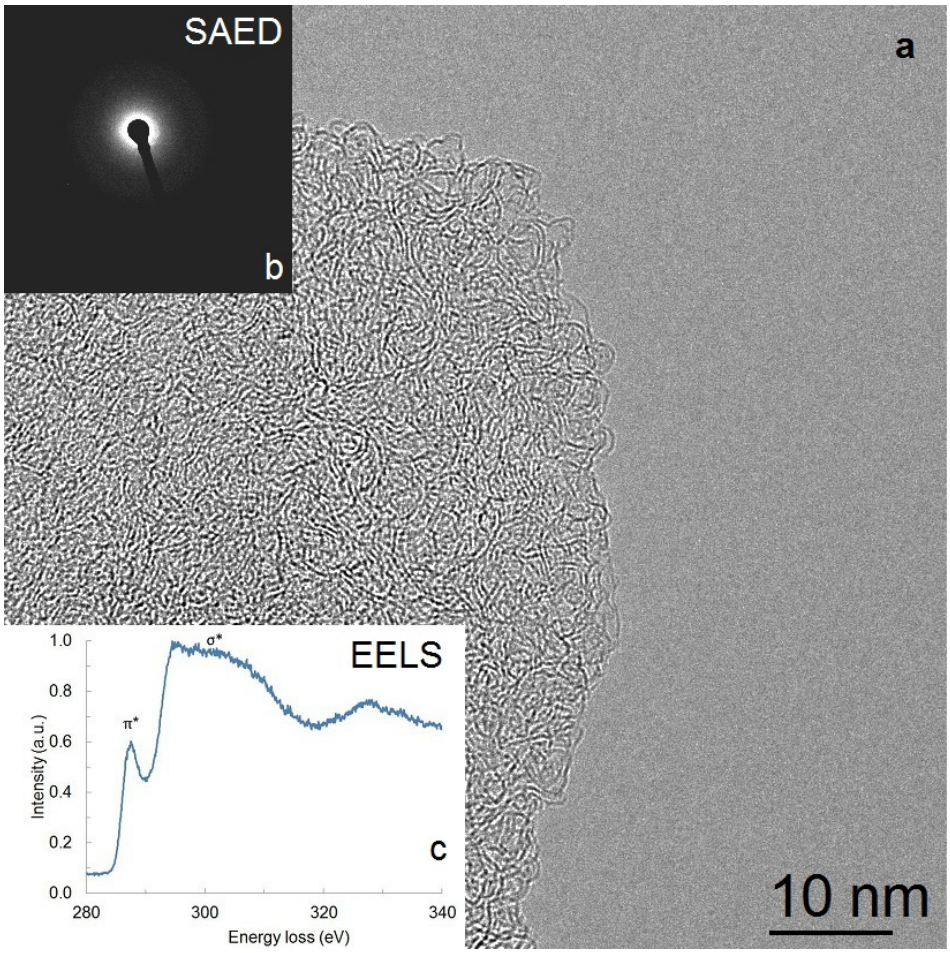

Figure 14. HRTEM micrograph (a) SAED pattern (b) and corresponding carbon-K ELNES (c) for amorphous WC-CDC prepared at 800 °C.

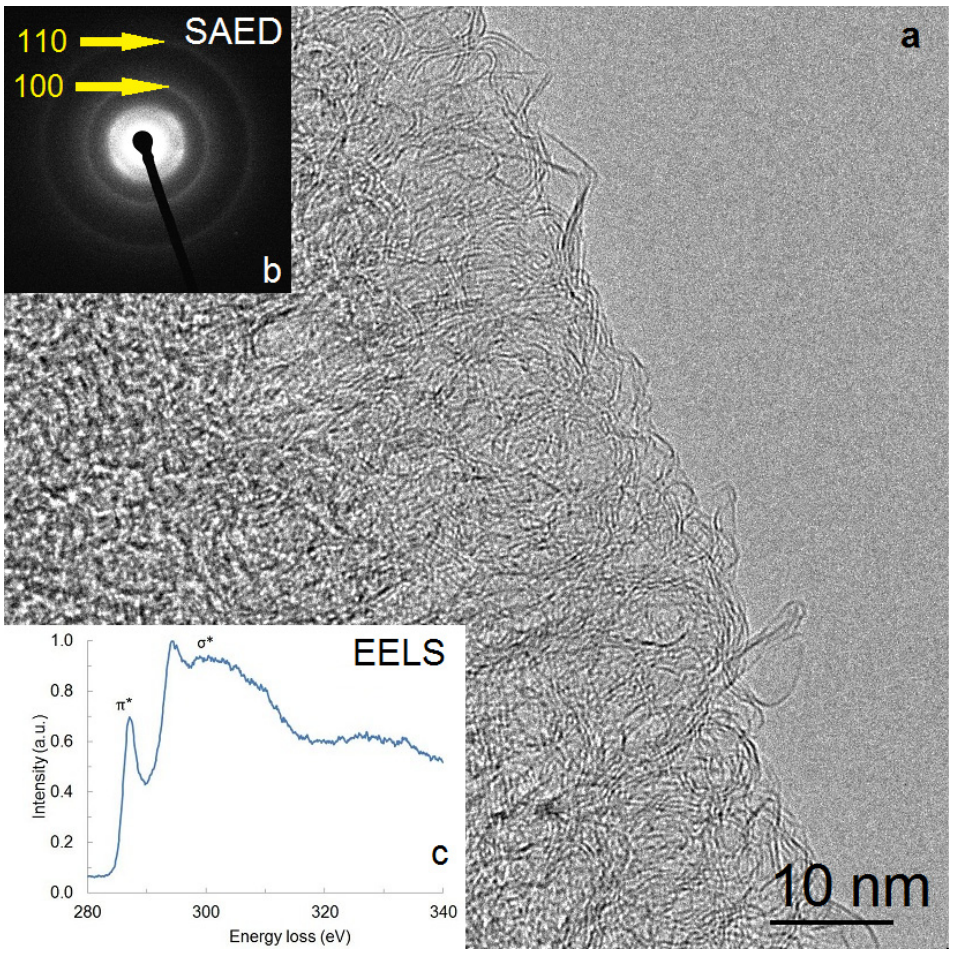

Figure 15. HRTEM micrograph (a) SAED pattern (b) and corresponding carbon-K ELNES (c) for partially graphitized WC-CDC prepared at 1100 °C.

5.2.3.3. HRTEM and SEM analysis of Ta_4HfC_5-CDC and $WTiC_2$-CDC powders

HRTEM studies of Ta_4HfC_5-CDC and $WTiC_2$-CDC powders, synthesized at various reaction temperatures, demonstrate the formation of the CDC graphitic layers onto a mostly amorphous carbon (Figure 16). However, slight ordering of carbon particles and the formation of the graphitic structures occurs at higher synthesis temperatures. A HRTEM micrograph for $WTiC_2$-CDC, synthesized at T_{synth} = 1100 °C shows the particle centers of few nanometers in diameter, surrounded by the carbon layers, which appear to be about 5 layers thick graphite like formations. This result is in agreement with the XRD data, indicating the limited mass transport of chlorine to the raw ternary carbide particles (block inside of the partially graphitized CDC) at higher synthesis temperatures.

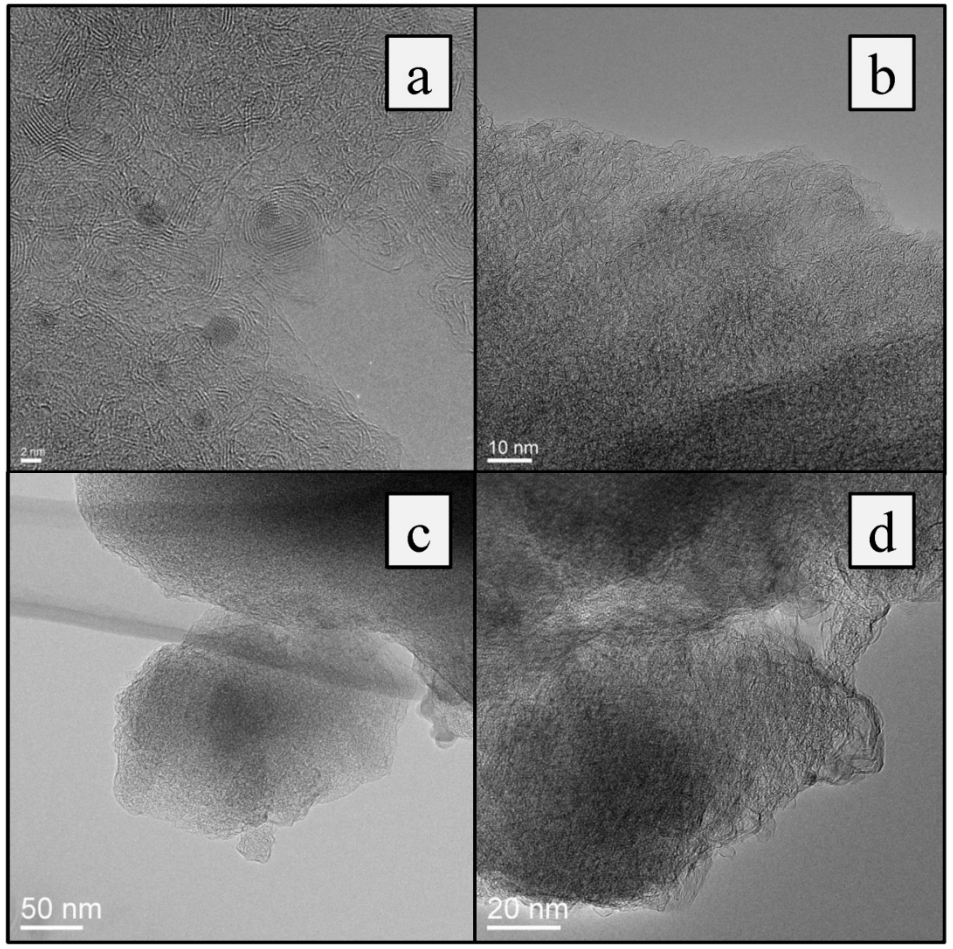

Figure 16. TEM micrographs for $WTiC_2$-CDC, synthesized at 1100 °C (a) and 900 °C (b), and Ta_4HfC_5-CDC, synthesized at 1000 °C (c) and 900 °C (d).

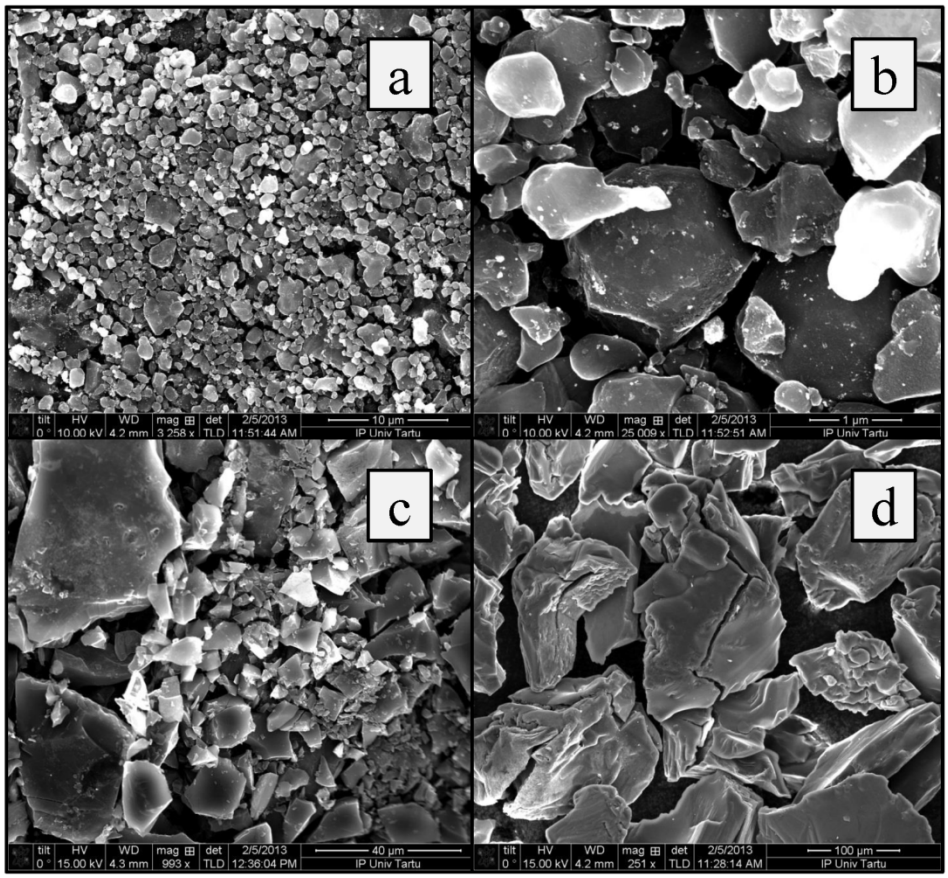

Figure 17. SEM images for Ta_4HfC_5-CDC, synthesized at 800 °C (a and b), and for $WTiC_2$-CDC, synthesized at 800 °C (c) and 1100 °C (d), respectively.

The SEM images for Ta_4HfC_5-CDC and $WTiC_2$-CDC (Figure 17) demonstrate the breaking down of the initial carbide particles into smaller ones. This is uncommon for the binary carbides, however, demonstrated for ternary carbides [110]. It can be explained by variations in the bond strengths (i.e., chemical reactivity) between the carbon and different metal atoms, or also by the chemical inhomogeneity of the initial ternary carbide phases. The average particle size of Ta_4HfC_5 was 45 μm, while the Ta_4HfC_5-CDC powder had decomposed into particles ranging from 0.2 to 2 μm with an average size of around 1 μm, as can be seen in Figure 17a and 17b. The initial particle size of $WTiC_2$ was 150 μm, however the $WTiC_2$-CDC had decomposed into powders having very variable particle sizes ranging from 1 to 50 μm, if the synthesis temperatures up to 1000 °C have been applied (Figure 17c). Surprisingly, there were no smaller particles (less than 50 μm) and only some bigger cracks had been formed into $WTiC_2$-CDC powder particles, synthesized at T_{synth} = 1100 °C

(Figure 17d). Based on XRD data discussed above, the synthesis of $WTiC_2$-CDC at T_{synth} = 1100 °C was not complete. Thus, probably the breaking down of carbon particles occurred mainly at the very end of the chlorination reaction of ternary carbides, when the internal stresses reached to some critical value.

5.3. Electrochemical characterization

5.3.1. Electrode preparation

The supercapacitor electrodes were composed of an aluminum (Al) current collector and a mixture of the active CDC layer with 6 % binder (PTFE, 60 % dispersion in H_2O). This mixture was laminated and roll–pressed (HS–160N, Hohsen Corporation, Japan) together to form a flexible layer of the active electrode material with thickness 100 ± 5 μm. After drying under vacuum, the pure Al layer (2 μm) was deposited onto one side of the CDC by the magnetron sputtering method. The electrode flat-cross section surface area used was 2.0 ± 0.1 cm^2.

5.3.2. Electrochemical cells completed

The electrolyte used was prepared from very pure acetonitrile (AN, H_2O < 20 ppm), and from dry $(C_2H_5)_3CH_3NBF_4$ (Stella Chemifa). The two–electrode standard Al test cell (HS Test Cell, Hohsen Corporation) with two identical CDC electrodes (geometric area ~2.0 cm^2) was completed inside a glove box (Labmaster sp, MBraun; O_2 and H_2O concentrations lower than 0.1 ppm) and all electrochemical experiments were carried out at temperature T = 20 °C. Carefully dried 25 μm thick TF4425 (Nippon Kodoshi) separator sheet was used for mechanical separation of the working CDC electrodes.

Electrochemical characteristics for the supercapacitors, consisting of the TiC-CDC(Cl_2), TiC-CDC(HCl), WC-CDC, $WTiC_2$-CDC or Ta_4HfC_5-CDC electrodes and 1 M $(C_2H_5)_3CH_3NBF_4$ solution in AN, have been studied by cyclic voltammetry (CV), constant current charge/discharge (CCCD), and by electrochemical impedance spectroscopy (EIS) methods using a SI1287 Solartron potentiostat and 1252A frequency response analyser over *ac* frequency *f* range from 1 mHz to 300 kHz at 5 mV modulation. Constant power (CP) method using a BT2000 testing system (Arbin Instruments, USA) has been applied for determination of the experimental Ragone plots.

5.3.3. Cyclic voltammetry data for TiC-CDC based EDLC

The CV curves for supercapacitors based on TiC-CDC(Cl_2) or TiC-CDC(HCl) electrodes in 1 M $(C_2H_5)_3CH_3NBF_4$ acetonitrile solution, presented in Figure 18 have nearly mirror image symmetry of the current responses about the zero current line obtained at potential scan rates $v \leq 50$ mV s^{-1}.

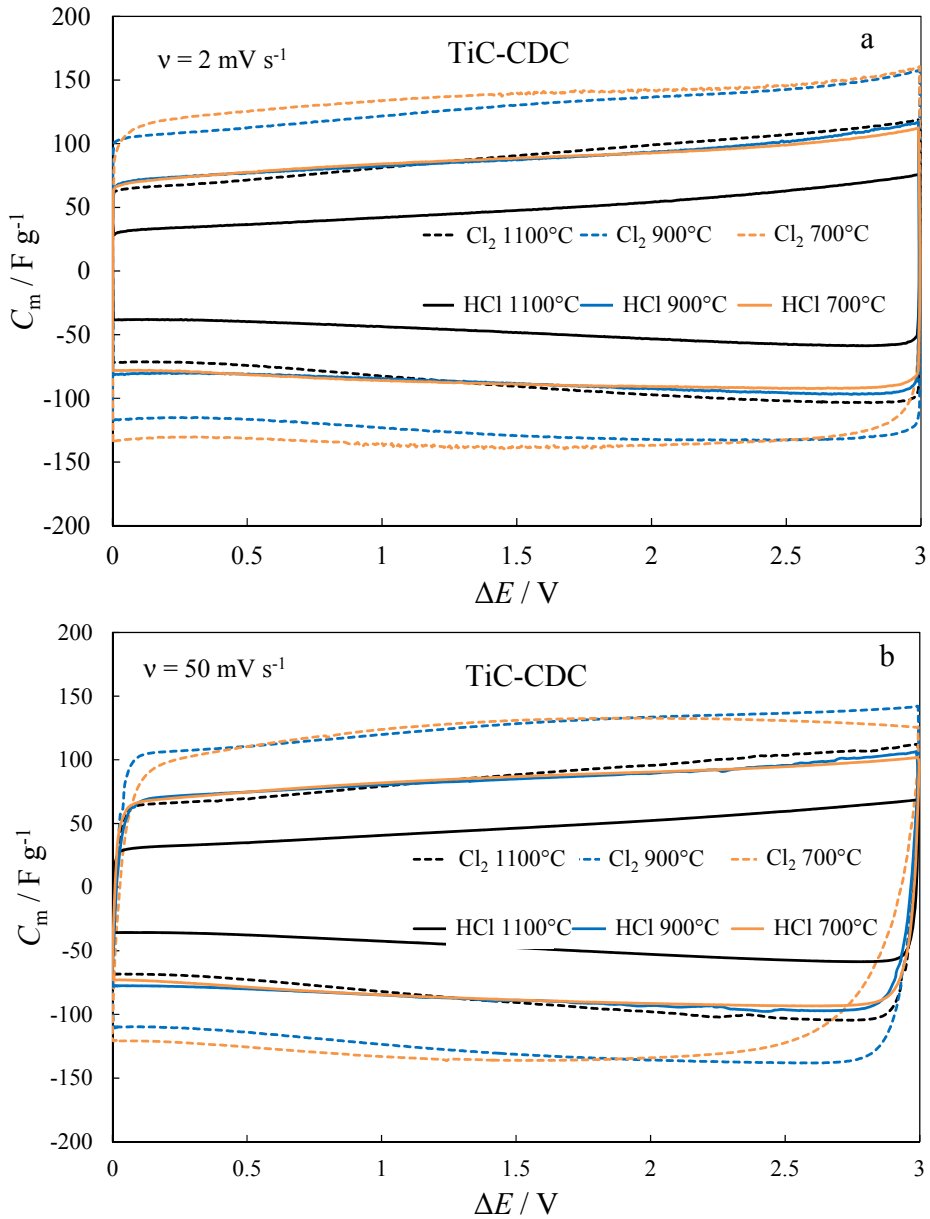

Figure 18. Specific capacitance vs. cell potential curves calculated from CV curves at potential scan rates $v = 2$ (a) and 50 mV s^{-1} (b) for the supercapacitors, completed using TiC-CDC electrodes, prepared at different synthesis temperatures by using different reactants.

The data given in Figure 18 show that there is some dependence of specific capacitance C_m on CDC under study. The calculated C_m capacitance values 136 F g^{-1} for TiC-CDC(Cl_2), synthesized at 900 °C, and 97 F g^{-1} for TiC-

CDC(HCl), synthesized at 900 °C, have been established. The decrease in C_m can probably be explained by the lower V_{micro} and V_{tot} values for TiC-CDC(HCl), given in Table 2 and demonstrated in Figure 18.

For both CDCs the values of C_m start to increase at $\Delta E \geq 3.2$ V, caused by the electroreduction of O_2 and H_2O traces at a negatively charged electrode and by the oxidation of surface functionalities at a positively charged electrode. However, electroreduction of complex BF_4^- anions is possible as well [13,30,95,96]. With increasing v over 50 mV s^{-1}, the cyclic voltammograms, i.e., the specific capacitance vs. cell potential dependencies, become distorted in the region of potential switchover for all materials studied, demonstrating the moderate adsorption/desorption and mass transfer rate of ions into TiC-CDC porous electrode structure under study.

5.3.4. Constant current charge/discharge data for TiC-CDC

The supercapacitors were tested at CCCD regimes (from 1 to 50 mA cm^{-2}) within the cell potentials range from 0 to 2.7 V (this range of ΔE has been selected for better comparison with literature data). The discharge and charge capacitances were calculated from the data of the third charging/discharging cycle.

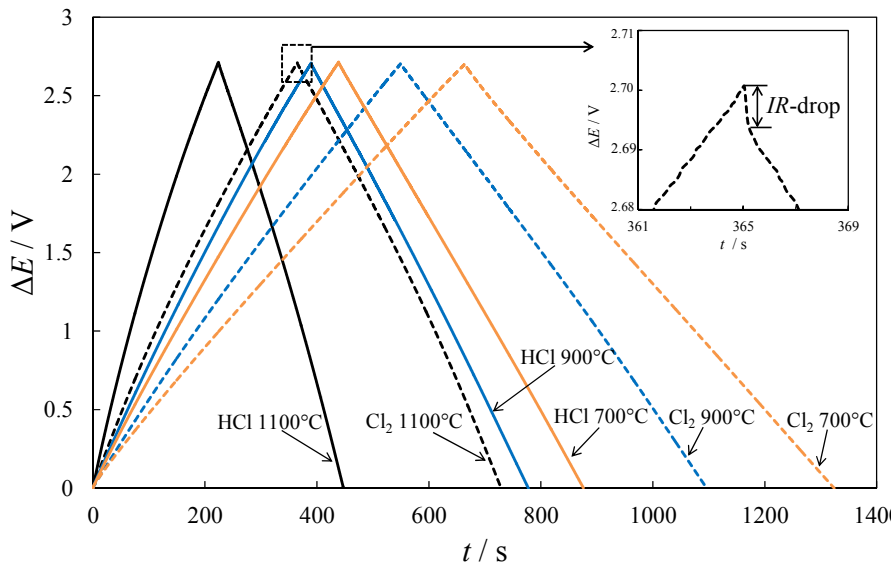

Figure 19. Constant current charge/discharge cycles at current density $j = 2$ mA cm^{-2} for supercapacitors, completed using TiC-CDC electrodes, prepared at different synthesis temperatures (given in the figure) by using different reactants. Magnification of constant current charge/discharge cycle near the IR-drop region at $\Delta E = 2.7$ V.

The capacitance of the cell C (F cm^{-2}) was obtained from the nearly linear region (slope) of the discharge (or charge) curve (Figure 19). As for simplicity the discharging (or charging) curves were approximated by a linear function, therefore the medium integral capacitance C values were calculated. The longest charge/discharge cycle has been observed for TiC-CDC(Cl_2) synthesized at 700 °C (Figure 14) corresponding to the highest specific capacitance value calculated from CCCD–curves, C_m = 129 F g^{-1}. This value is in a good agreement with C_m value calculated from CV–curves at $j \leq 50$ mV s^{-1}. For all TiC-CDC based systems, the calculated RTE value remained in the range from 98 to 99 %.

From the CCCD curves the value of internal resistance, R_{int}, has been calculated from the *IR*–drop after the changing the current direction ($R_{int} = d(\Delta E_1/2j$, where $d(\Delta E_1)$ is the value of cell potential for 10 ms). The lowest R_{int} value has been calculated for TiC-CDC(Cl_2) synthesized at 1100 °C or for TiC-CDC(HCl) synthesized at 1100 °C, which is in agreement with the analysis of impedance data, discussed below.

5.3.5. EIS for TiC-CDC based EDLC

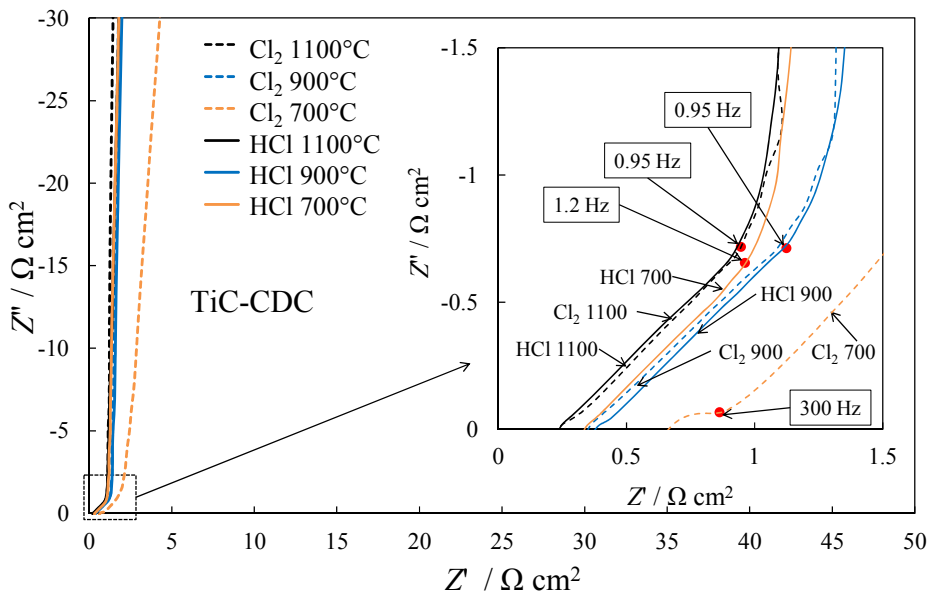

Figure 20. Nyquist plots and magnification of the Nyquist plots (inset) at higher and medium frequency values at cell potential ΔE = 3.0 V for EDLCs, completed using TiC-CDC electrodes, prepared at different synthesis temperatures (given in the figure) by using different reactants for synthesis of TiC-CDC (noted in the figure).

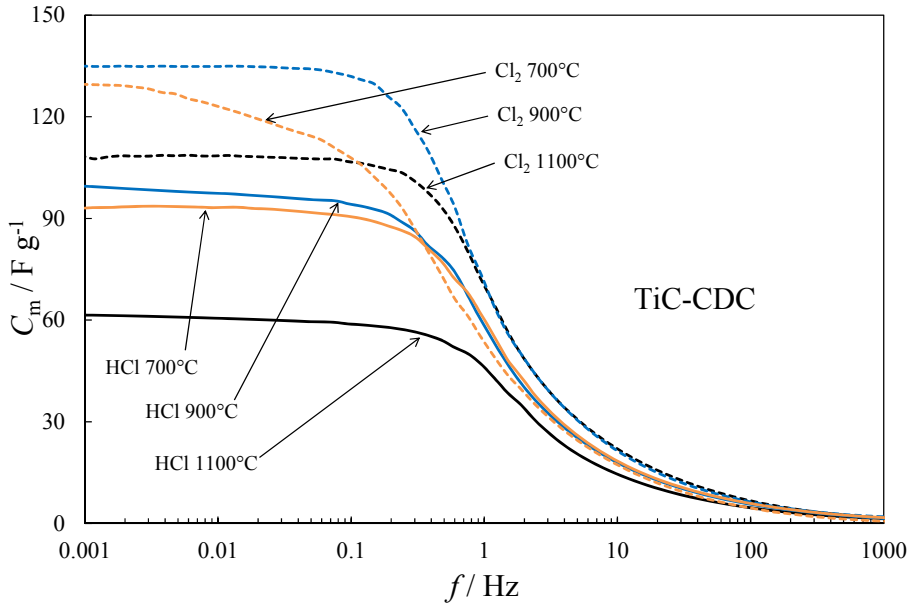

Figure 21. Specific gravimetric series capacitance C_m vs. ac frequency dependencies at cell potential ΔE = 3.0 V for EDLCs, completed using TiC-CDC electrodes, prepared at different synthesis temperatures (given in the figure) by using different reactants for synthesis of TiC-CDC (noted in the figure).

The Nyquist (Z", Z') plots for TiC-CDC based EDLC have been measured within the range of ac frequency f from 1 mHz to 300 kHz at fixed cell potentials ΔE from 0 to 3.2 V. The shape of Z'', Z' plots depends noticeably on the CDC material characteristics, but is practically independent of ΔE applied, if $\Delta E \leq 3.2$ V. The Nyquist plots consist mainly of three parts: (1) the small semicircle at higher ac frequency $f \geq 300$ Hz, which is more expressed only for TiC-CDC(HCl) synthesized at 700 °C (semicircle shape depends on the adsorption kinetics of ions at micro/mesoporous TiC-CDC electrode and on the series resistance of a material, charge transfer resistance inside the macro/meso-porous carbon structure as well as on the mass transfer resistance in the porous carbon electrode); (2) very well expressed so–called "porous" region with a slope of $\alpha \approx -45°$, within *ac* frequency region $1 < f < 300$ Hz, characteristic of the mass transfer limited process in the micro/mesoporous carbon electrode matrix of an electrode and (3) the double–layer capacitance region with a slope of $\alpha \approx -89°$ ("knee" at low frequencies $f < 1$ Hz), obtained by the finite length effect.

According to the data in Figure 20, equivalent series resistance (ESR), obtained by extrapolation of high frequency part of the Nyquist plot to the condition $Z''(\omega) = 0$ gives the ESR for of the cell (ESR = $Z'(\omega)$; $\omega \to \infty$). ESR depends noticeably on the CDC synthesis conditions and temperature, which

determine the porosity and graphitization level, i.e., on the amount of graphitic sp^2–carbon in TiC-CDC. The increase of ESR for TiC–CDC(Cl_2) prepared at lower temperatures ($T \leq 900$ °C) is probably mainly caused by the bigger fraction of micropores or more curved pores, where the mass transfer rate of ions is somewhat limited.

The specific series capacitance C_m values at ac frequency $f \sim 1$ mHz, calculated from the Z'', Z' plots (Figure 21) , are in a good agreement with the values obtained by CV and CCCD methods. The calculated capacitance data are comparable with parameters obtained for other CDC materials previously studied [13,55,59].

5.3.6. Specific energy and power plots for TiC-CDC based EDLCs

The maximum specific energy E_{max} (W h kg^{-1}) and power P_{max} (kW kg^{-1}) for supercapacitors studied have been calculated using Eqs. (16a) and (16b). The specific energy, calculated at cell potential $\Delta E = 3.0$ V, is maximal for TiC-CDC(Cl_2)800 °C and TiC-CDC(HCl) 900 °C, being 43.1 W h kg^{-1} and 31.1 W h kg^{-1}, respectively. The specific power, calculated at cell potential $\Delta E = 3.0$ V, is maximal for TiC-CDC(Cl_2)1000 °C and TiC-CDC(HCl) 1000 °C (Figure 22), 805.2 kW kg^{-1} and 847.5 kW kg^{-1}, respectively. Comparison of these values with the data obtained previously shows that the calculated P_{max} values are very high.

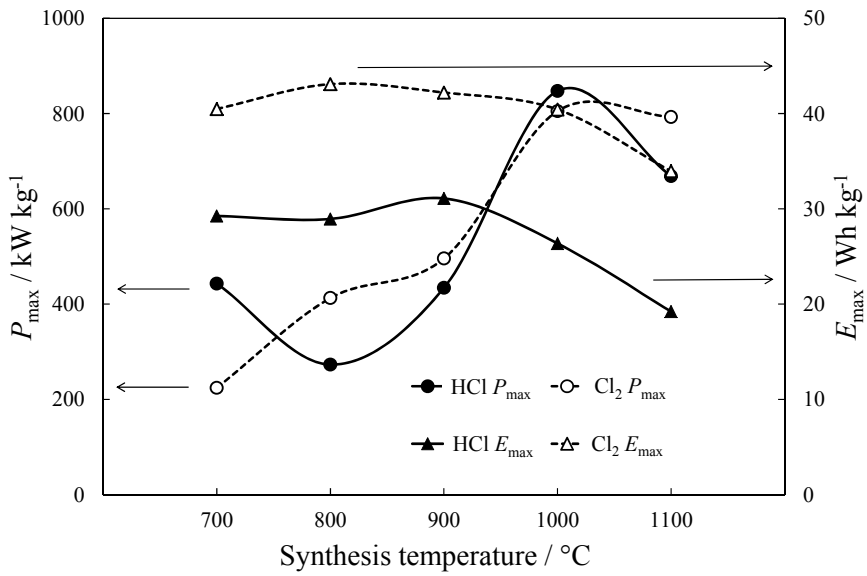

Figure 22. Maximal specific energy and power vs. synthesis temperature plots for the EDLCs, completed using TiC-CDC electrodes, prepared at different synthesis temperatures (given in the figure) by using different reactants (open marks denote Cl_2, filled marks denote HCl).

The experimental Ragone plots (calculated to the total active material weight of two electrodes) of the supercapacitors based on TiC-CDC(Cl_2) and TiC-CDC(HCl) electrodes have been obtained from constant power tests within the cell potential range from 3.0 V to 1.5 V and are shown in Figure 23. The experimental Ragone plots for carbide-derived carbons prepared using different reactants (Cl_2, HCl) are quite similar. However, at higher power loads TiC-CDC(Cl_2) material based cells, synthesized at 900 °C, (cells, based on materials with optimal micro- and mesopore fraction) deliver somewhat higher power at constant energy applied than other TiC-CDC materials based 2 electrode cells.

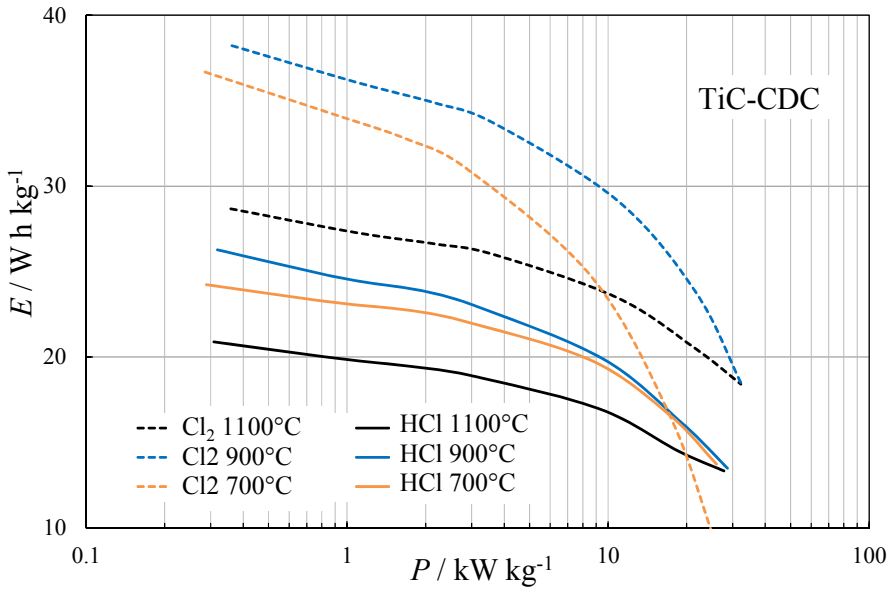

Figure 23. Ragone plots for the EDLCs completed using TiC-CDC electrodes.

5.3.7. Cyclic voltammetry data for WC-CDC based EDLC

The cyclic voltammetry (CV) curves for WC–CDC electrodes in 1 M $(C_2H_5)_3CH_3NBF_4$ + AN solution presented in Figures 24 – 26 have nearly mirror image symmetry of the current responses about the zero current line obtained at potential scan rates $v \leq 50$ mV s^{-1} ($v = d(\Delta E)/dt$) (Figure 25) and cell potential $\Delta E \leq 3.2$ V (Figure 26).

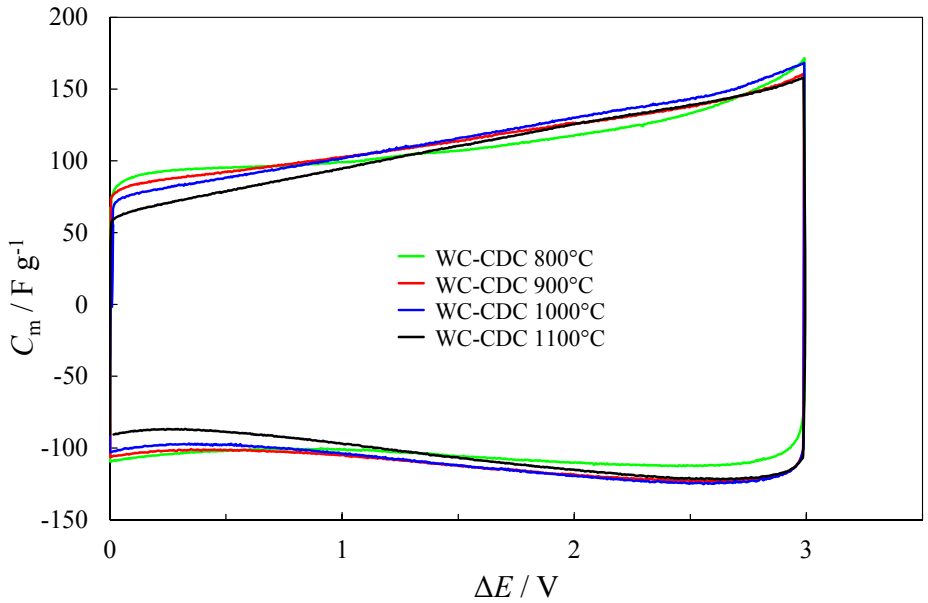

Figure 24. Specific capacitance vs. cell potential curves, calculated from CV–curves at potential scan rate $v = 1$ mV s^{-1} for the EDLCs completed using WC–CDC electrodes, prepared at different temperatures.

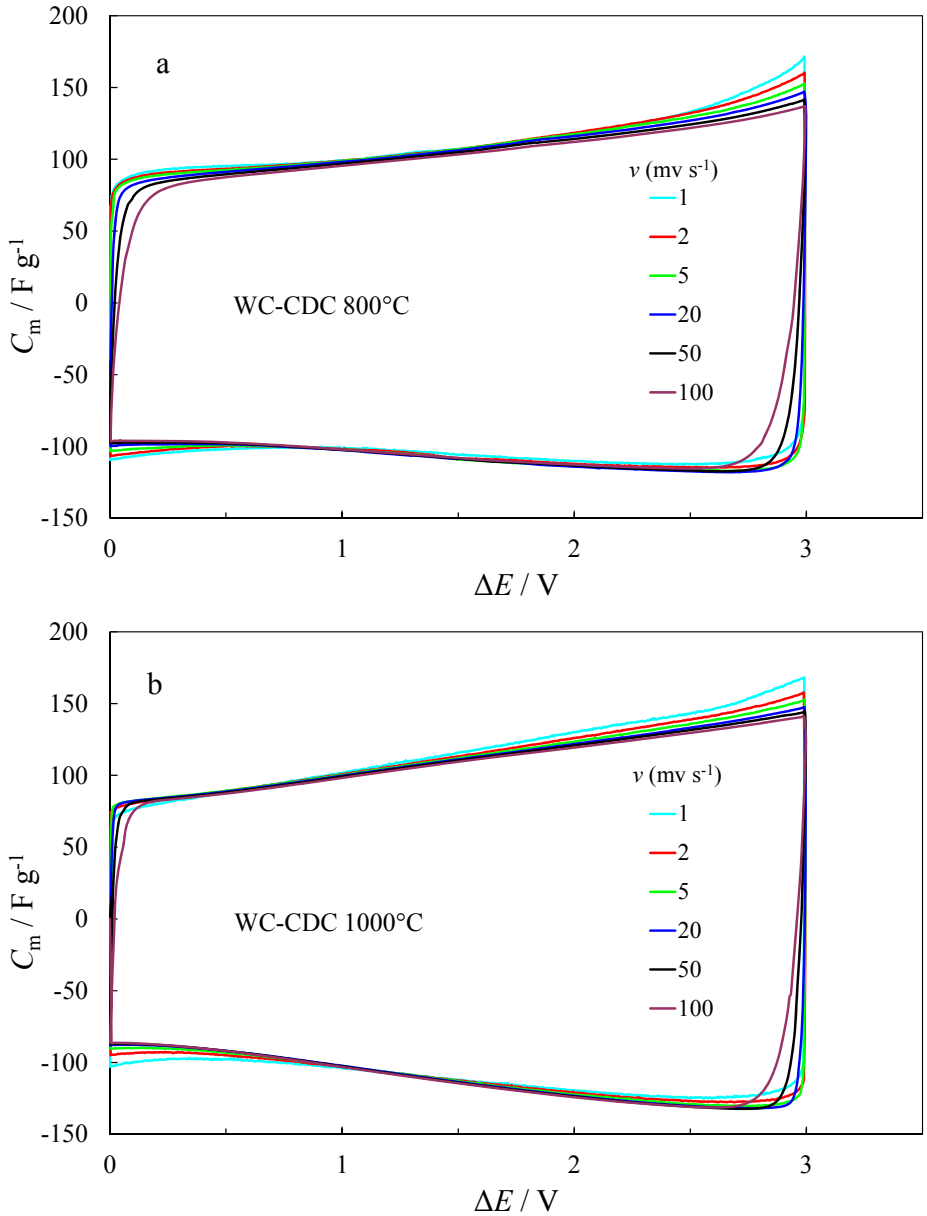

Figure 25. Specific capacitance vs. cell potential curves, calculated from CV–curves at different potential scan rates (mV s^{-1}) for the EDLCs, completed using WC–CDC electrodes, prepared at (a) 800 °C and (b) 1000 °C.

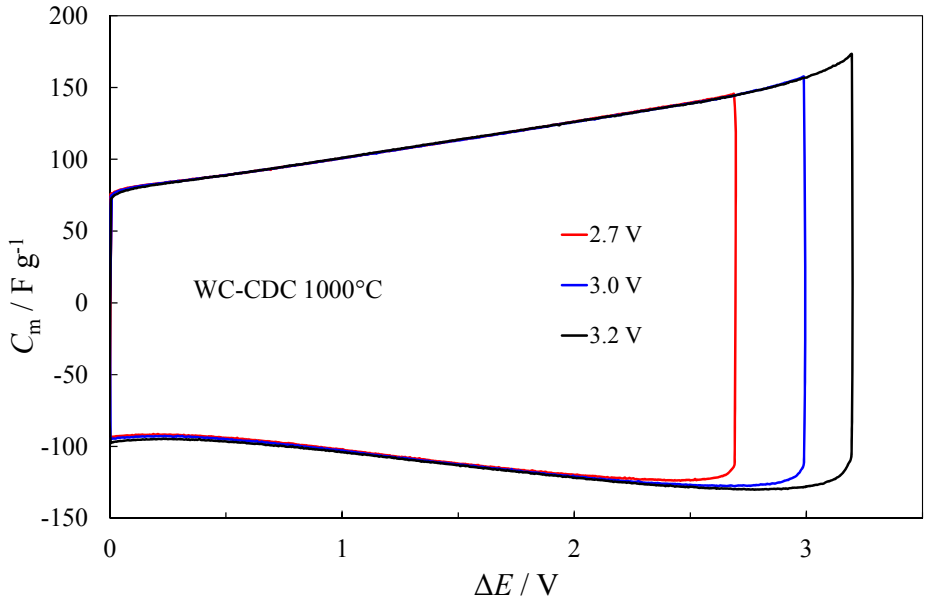

Figure 26. Specific capacitance vs. cell potential curves, calculated from CV–curves at potential scan rate v = 2 mV s^{-1}, for the EDLC, completed using WC–CDC electrodes, prepared at 1000 °C, at different cell potentials.

The values of specific capacitance C_m = 120 F g^{-1}(Figure 24) calculated from CV–curves at $\Delta E \leq 3.0$ V are practically independent of synthesis temperature T_{synt} within the range from 900 to 1100 °C. Only somewhat lower C_m values have been calculated for WC–CDC, synthesized at 800 °C. The decrease in C_m can probably explained by the lower V_{micro} and V_{tot} values, i.e., by the presence of smaller pores not accessible for electrolyte ions, indicating that for $(C_2H_5)_3CH_3NBF_4$ + AN electrolyte system an optimal pore size for ions adsorption is above $d \sim 0.7$ nm and the micropores with diameter below $d \sim 0.7$ nm are too small for the quick effective adsorption of ions. Similarly to TiC-CDC based SCs, the values of C_m start to increase at $\Delta E \geq 3.2$ V, which is caused by the electroreduction of O_2 and H_2O traces at the negatively charged electrode and by oxidation of surface functionalities at the positively charged electrode. With increasing v over 50 mV s^{-1} the cyclic voltammograms, i.e., specific capacitance vs. cell potential dependencies, became distorted in the region of potential switchover for all systems studied. However, differently from TiC-CDC(HCl) electrodes, this effect is quite small even for WC–CDC synthesized at 800 °C, which is the most microporous carbon material among WC–CDC under study.

5.3.8. Constant current charge/discharge data for WC-CDC based EDLC

The EDLCs were tested at CCCD regimes (from 1 to 50 mA cm^{-2}) within the cell potentials range from 0 to 2.7 V. The discharge and charge capacitances were calculated from the data of the third cycle. For simplicity the discharging curve was approximated by a linear function within the region of ΔE from 0.7 to 2.0 V. Therefore, the medium integral capacitance C_m values were calculated. The longest charge/discharge cycle has been observed for WC–CDC material synthesized at 900 °C (Figure 27) corresponding to the highest specific capacitance value calculated from CCCD curves, C_m = 114 F g^{-1}. However, surprisingly, the specific capacitance values, calculated for EDLCs based on WC–CDC materials, synthesized at different temperatures, were practically independent of material synthesis T under study and vary only 5 %. This is mainly caused by the weak variation of the porosity data (S_{BET}, V_{micro}, V_{tot} etc.) with T_{synt} applied.

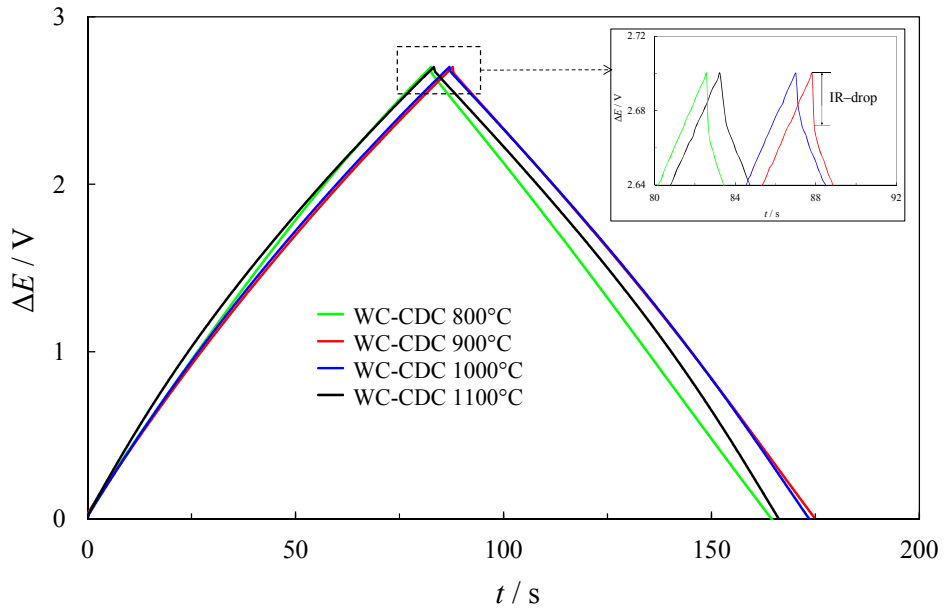

Figure 27. Constant current charge/discharge cycles at current density j = 10 mA cm^{-2} for the EDLCs, completed using WC–CDC electrodes prepared at different temperatures.

The round trip coulombic efficiency (RTE) has been calculated as a ratio of capacitances measured during discharging and charging of WC-CDC based EDLCs. For all systems calculated RTE value remained in the range from 98 to 99% showing that WC–CDC materials are promising materials for energy storage application.

From the constant current charge/discharge curves the value of internal resistance, R_{int}, has been calculated being lowest for WC–CDC 1000 °C in agreement with the analysis of impedance data (discussed below).

5.3.9. EIS for WC-CDC based EDLC

The impedance complex plane (Z'', Z') plots for EDLCs completed from WC–CDC electrodes and 1 M $(C_2H_5)_3CH_3NBF_4$ + AN solution have been measured within the range of *ac* frequency f from 1 mHz to 300 kHz and at fixed cell potentials from 0 to 3.2 V. The shape of Z'', Z' plots depends noticeably on the micro-mesoporous WC–CDC material characteristics, but is practically independent of ΔE applied, if $\Delta E \leq 3.0$ V. Thus, the Z'', Z'-plot slope at $f \rightarrow 0$ is practically independent of T_{synt}.

According to the data in Figures 28 and 29 and Table 3, ESR depends noticeably on the WC–CDC synthesis temperature, i.e., on the porosity and amount of graphitic sp^2–carbon in WC–CDC. The increase of ESR for WC–CDC prepared at lower temperatures ($T \leq 800$ °C) is probably mainly caused by the bigger fraction of micropores or more curved pores, where the mass transfer rate of ions is limited.

The values of C_s obtained at *ac* frequency $f \sim 1$ mHz are in a good agreement with the values obtained by CV and CC methods and data obtained for other CDC materials studied. Surprisingly, all WC–CDC materials show very quick frequency response and nearly ideal capacitive behavior already at relatively high *ac* frequency $f \sim 1$ Hz compared to the TiC-CDC(Cl_2), or TiC-CDC(HCl) and other carbon materials synthesized and studied in various non–aqueous electrolyte systems earlier by Tartu group [13,55,59] as well as by other groups [19,111,112]. However, more pronounced dependence of C_s on f at $f \geq 1$ Hz has been observed for WC–CDC synthesized at 800 °C, which is the most microporous carbon material (Table 1) among WC–CDC under study.

Comparison of the data for the cells completed using different WC–CDC electrodes indicates only a small influence of the electrode material synthesis temperature, i.e., porous structure and parameters like micro– and mesopore volume, pore size distribution etc., on the τ_R values. Characteristic time constant values decrease in the same order as ESR (i.e., with values of synthesis temperature) being minimal for WC–CDC synthesized at 1000 °C (Table 3).

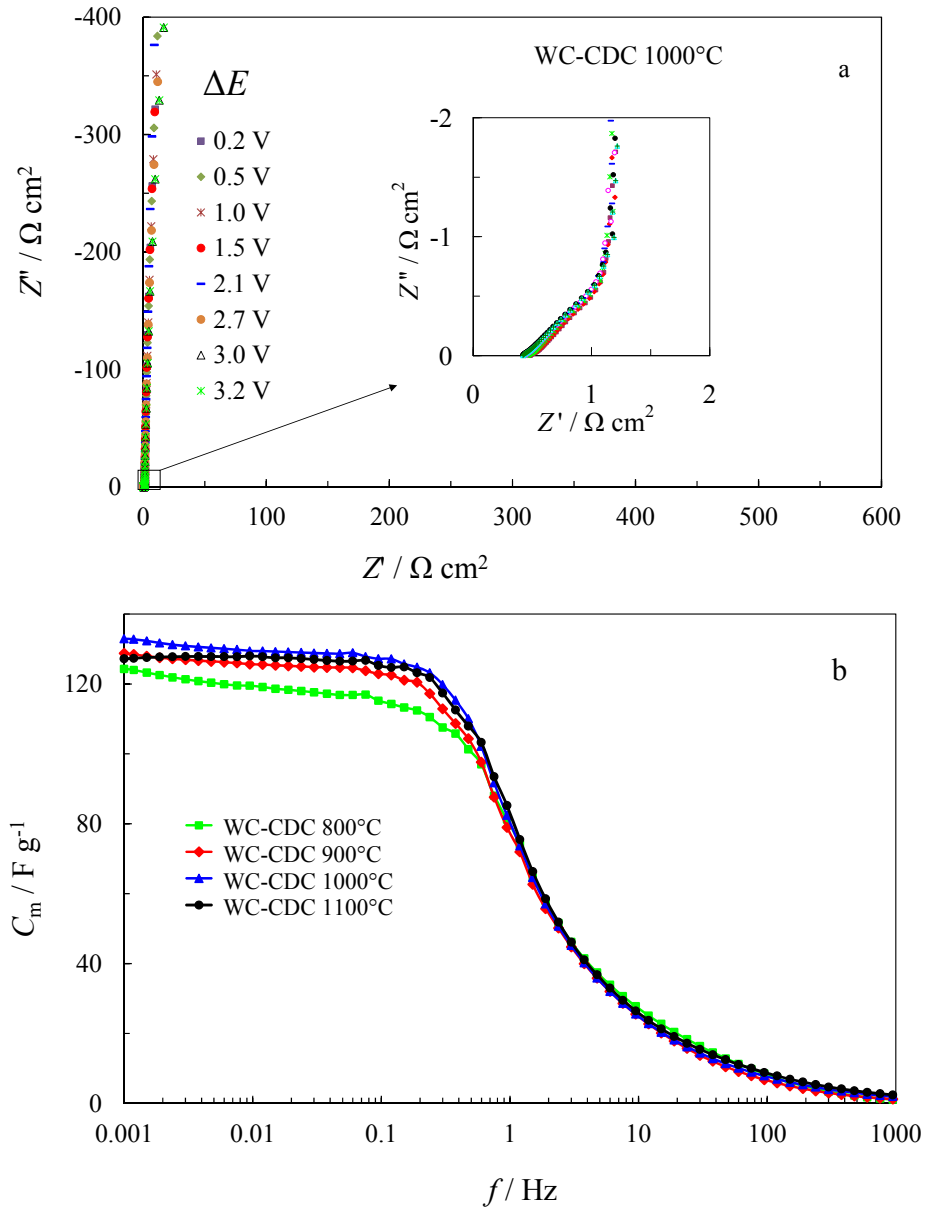

Figure 28. Impedance complex plane plots (a) for the EDLCs completed using WC–CDC electrodes, prepared at 1000 °C and at different cell potentials. Specific series capacitance C_m vs. ac frequency dependencies (b) at cell potential ΔE = 3.0 V for the EDLCs, completed using WC–CDC electrodes, prepared at different temperatures (°C).

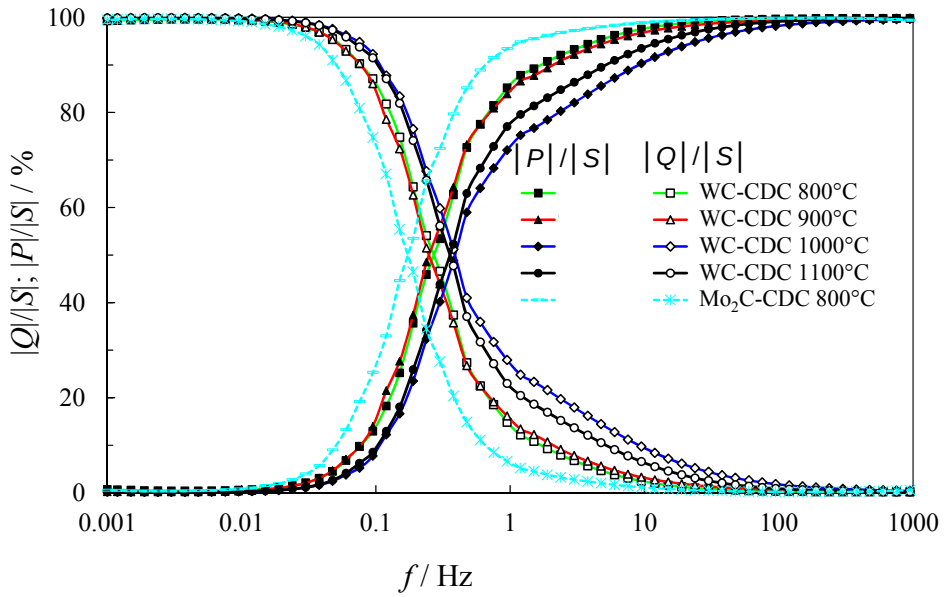

Figure 29. Normalized reactive power |Q|/|S| and active power |P|/|S| vs. ac frequency plots at cell potential ΔE = 3.0 V for the EDLCs completed using WC–CDC electrodes, prepared at different temperatures and Mo_2C–CDC electrodes prepared at temperature 800 °C (dashed lines).

Table 3. Electrochemical parameters for EDLCs based WC–CDC electrodes.

T_{synt} (°C)	R_E (Ω cm^2)	C_m (F g^{-1})	τ_R (s)	E_{max} (W h kg^{-1})	P_{max} (kW kg^{-1})
800	0.90	124	0.59	39	200
900	0.81	128	0.64	40	210
1000	0.42	132	0.41	41	430
1100	0.63	127	0.45	40	310

R_E – equivalent series resistance calculated from impedance data at $f \rightarrow \infty$, C_m – specific series capacitance calculated from electrochemical impedance data at cell potential ΔE = 3.0 V and *ac* frequency f = 1 mHz, τ_R – characteristic time constant, E_{max} – maximum specific energy, P_{max} – maximum specific power.

5.3.10. Specific energy and power plots for WC-CDC based EDLCs

The maximum specific energy E_{max} (W h kg^{-1}) and specific power P_{max} (kW kg^{-1}) for EDLCs studied can be estimated using Eqs. (3) and (4). The specific energy and specific power, calculated at cell potential ΔE = 3.0 V, are maximal for WC–CDC synthesized at 1000 °C (Table 2), 41 W h kg^{-1} and 430 kW kg^{-1}, respectively.

The specific energy and power relationship (calculated for the total active material weight of two electrodes), i.e., experimental Ragone plots, of the EDLCs based on WC–CDC electrodes have been obtained from constant power tests within the cell potential range from 3.0 V to 1.5 V and are shown in Figure 30. The Ragone plots for EDLCs based on different WC–CDC material synthesized at different temperatures are nearly comparable and E_{max} values are practically independent of WC–CDC material synthesis temperature at low and moderate specific power loads. At higher power loads WC–CDC materials, which are synthesized at higher temperatures (especially at $T \geq 1000$ °C) (i.e., the more mesoporous systems), deliver somewhat higher power at constant energy.

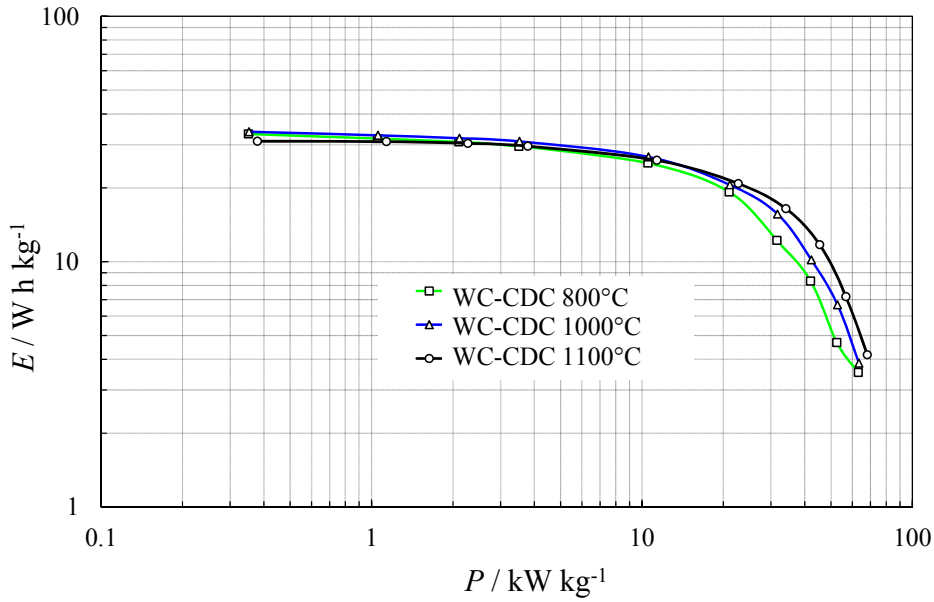

Figure 30. Ragone plots for the EDLCs completed using WC–CDC electrodes, prepared at different temperatures.

5.3.11. Cyclic voltammetry data for $WTiC_2$-CDC and Ta_4HfC_5-CDC based EDLC

The CV curves for supercapacitors based on Ta_4HfC_5-CDC and $WTiC_2$-CDC electrodes and 1 M $(C_2H_5)_3CH_3NBF_4$ solution in acetonitrile, presented in Figure 31, have nearly mirror image symmetry of the current responses about the zero current line, obtained at potential scan rates $v \leq 50$ mV s^{-1}.

There are only very slight differences in specific capacitance C_m, calculated from CV–curves at cell potential 3.0 V with the capacitance values 110 ± 10 F g^{-1} for the obtained carbon materials (Figure 31 and Table 4). Only some-

what lower C_m values were obtained for electrodes made from $WTiC_2$-CDC synthesized at 800 °C, and for Ta_4HfC_5-CDC, synthesized at 1100 °C, characterized by lower S_{BET} values.

Table 4. Calculated specific capacitance values from cyclic voltammetry ($\Delta E = 3$V; $v = 1$ mV s^{-1}), constant current ($\Delta E = 2.7$ V; $j = 1$ mA cm^{-2}) and impedance spectroscopy measurements ($\Delta E = 3$V; $f = 1$mHz) for the supercapacitors, completed using Ta_4HfC_5-CDC and $WTiC_2$-CDC electrodes, prepared at different synthesis temperatures.

Precursor	Synthesis temperature (°C)	Cyclic voltammetry (F g^{-1})	Constant current (F g^{-1})	Impedance spectroscopy (F g^{-1})
Ta_4HfC_5	800	116.0	113.1	119.0
	900	115.2	113.0	124.7
	1000	111.3	102.8	120.4
	1100	105.6	93.1	115.3
$WTiC_2$	800	98.4	93.3	97.3
	900	113.4	105.7	120.7
	1000	111.3	97.1	119.0

Similarly to TiC-CDC(Cl_2), TiC-CDC(HCl) and WC-CDC materials based EDLCs, the values of C_m start to increase at cell potentials over 3.2 V, which is caused by the electroreduction of O_2 and H_2O traces at a negatively charged electrode and by oxidation of the surface functionalities at a positively charged electrode [2,31-33]. With increasing v over 50 mV s^{-1}, the cyclic voltammograms and the calculated specific capacitance vs. cell potential dependencies became distorted in the region of potential switchover for all materials studied, probably due to the slow mass-transfer step in the porous CDC matrix. Another possible explanation is that the breaking down of particles, as established using SEM data, creates many new boundaries increasing the overall resistance of the CDC material layer. Surprisingly, the formed cracks and macropores are not significantly lowering the mass-transfer resistance values within the material porous structure, thus, not acting as extra pores for mass transport.

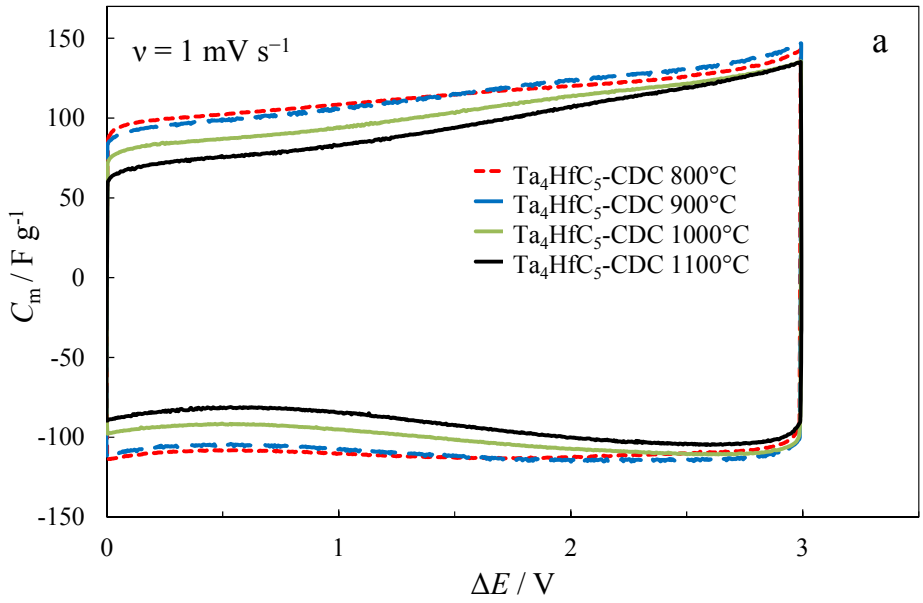

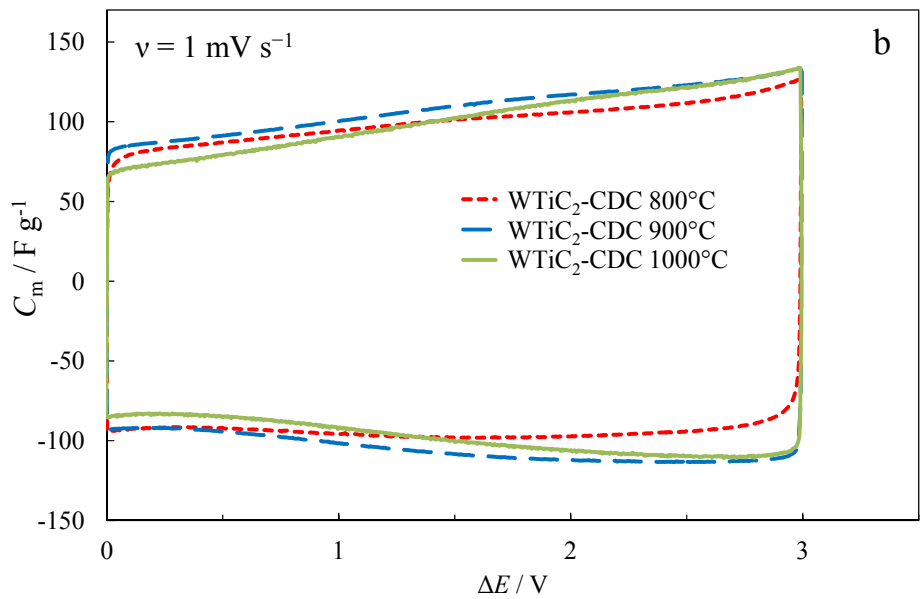

Figure 31. Continued

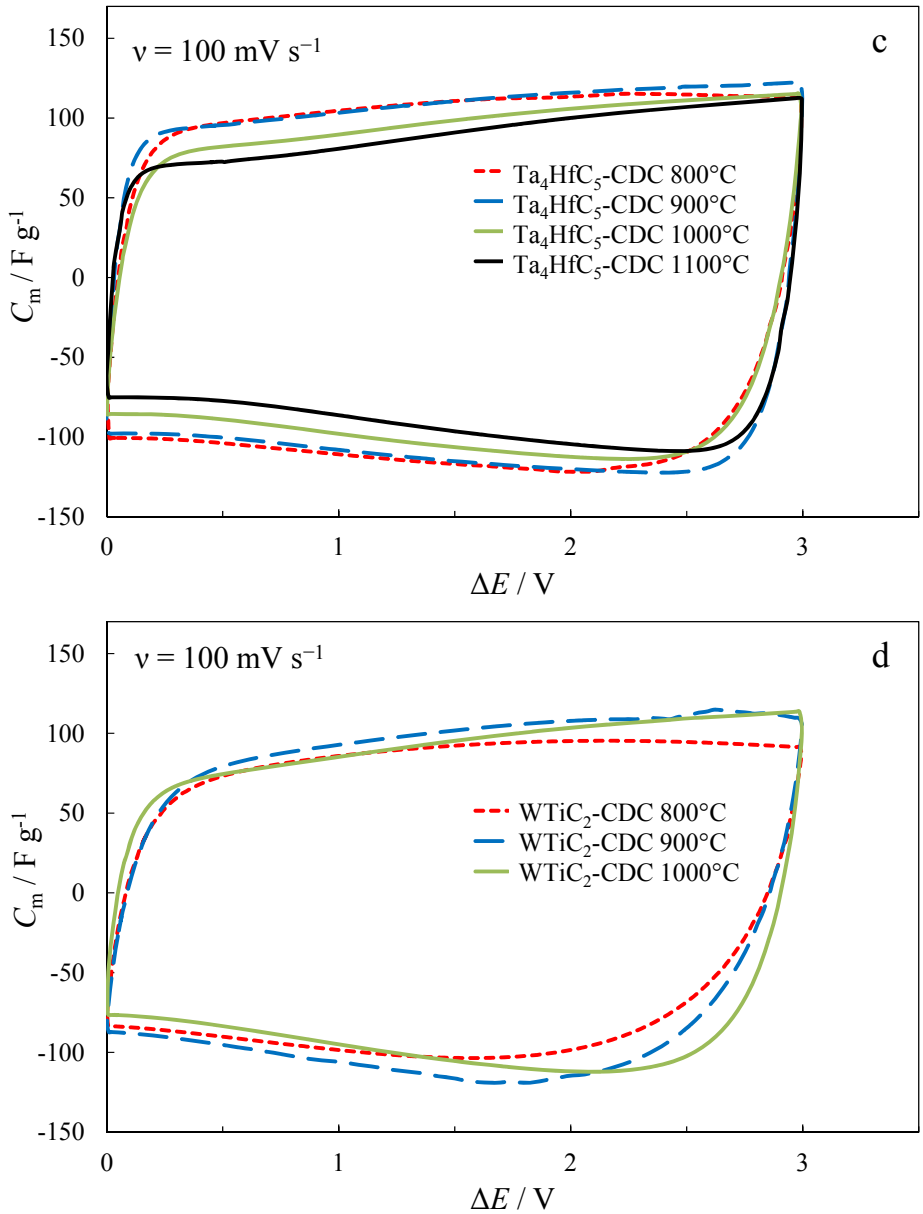

Figure 31. Specific capacitance vs. cell potential curves, calculated from CV curves at potential scan rates ν = 1 (a, b) and 100 mV s^{-1} (c, d) for the supercapacitors, completed using Ta_4HfC_5-CDC and $WTiC_2$-CDC electrodes, prepared at different synthesis temperatures.

5.3.12. Constant current charge/discharge data for $WTiC_2$-CDC and Ta_4HfC_5-CDC based EDLC

The supercapacitors were tested at CCCD regimes (from 1 to 50 mA cm^{-2}) at the cell potentials from 0 to 2.7 V (Figure 32).

For simplicity, the nearly linear experimental discharging (and charging) curve was approximated by a linear function within the cell potential region from 1.3 to 2.5 V. The obtained medium integral specific capacitance values (Table 4) are slightly lower than those calculated from CVs, but are nevertheless in a good accordance with the C_m values, obtained from the CV data. The lower capacitance values can be explained by physical differences in methods applied as well as by not totally linear shape of the discharging curves used for the calculation of C_m.

The round trip coulombic efficiency (RTE) has been calculated as a ratio of capacitances measured during discharging and charging of the supercapacitor cells under examination. For all the systems analyzed, the calculated RTE values remained within the range from 98 to 99 %.

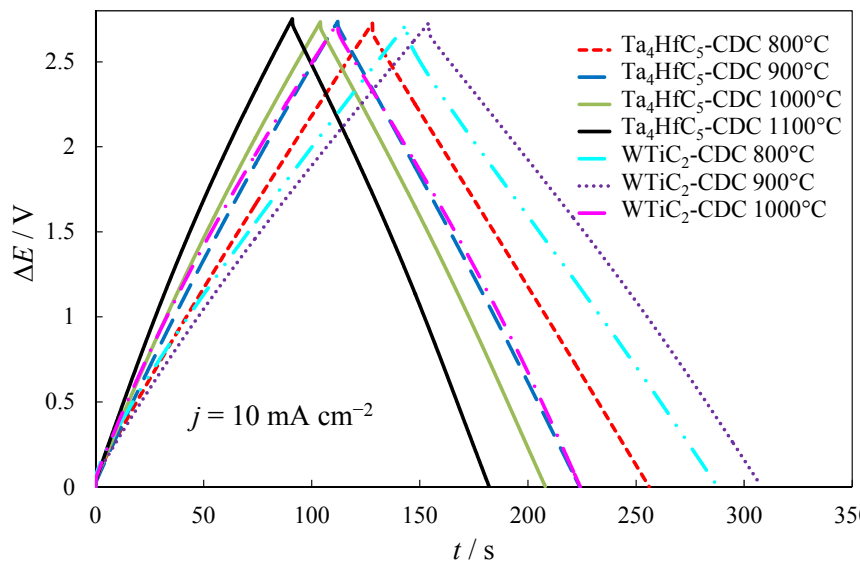

Figure 32. Constant current charge/discharge cycles at current density $j = 10$ mA cm^{-2} for the supercapacitors, completed using Ta_4HfC_5-CDC and $WTiC_2$-CDC based electrodes, synthesized at different temperatures.

5.3.13. EIS for $WTiC_2$-CDC and Ta_4HfC_5-CDC based EDLC

The shape of Nyquist (Z'', Z') plots (Figure 33) measured within the range of ac frequency, f, from 1 mHz to 300 kHz at fixed cell potentials from 0 to 3.2 V depends noticeably on the CDC material characteristics.

According to the data in Figure 33, ESR depends noticeably on the CDC synthesis conditions and temperature, decreasing with the amount of graphitic sp^2–carbon in CDC. Differences in ESR for the synthesized CDC materials are probably mainly caused by the bigger fraction of the micropores or more curved pores, where the mass transfer rate of the ions is limited.

The specific series capacitance values, C_m, calculated from the Z'', Z' plots at ac frequency $f \leq 1$ mHz (Figure 34) are somewhat higher, but nevertheless in a good agreement with the values obtained using CV and CC methods, and with data obtained for TiC-CDC(Cl_2), TiC-CDC(HCl) and other CDC materials studied [13,55,59]. It is also possible that these small differences can be explained by the fact that the capacitance values calculated using the CV and CCCD conditions are slightly lower due to the problem that the electrochemical equilibrium has not completely established due to the lower mass transfer of ions in micro-mesoporous materials. Taking into account that the phase angle values for TiC-CDC(Cl_2), TiC-CDC(HCl), WC-CDC, $WTiC_2$-CDC and Ta_4HfC_5-CDC based EDLCs are comparable, different time constants calculated can be explained by variation of the micro-mesoporosity of materials under study. Therefore, the maximum C_m value has been calculated for Ta_4HfC_5-CDC (900 °C) or $WTiC_2$-CDC (800 °C), i.e., for CDC with optimal ratio of micro- and mesopores in carbon used.

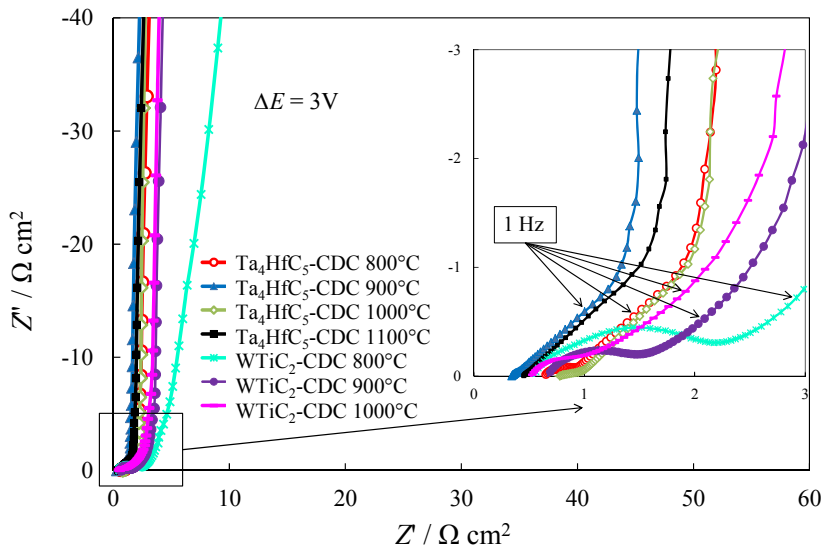

Figure 33. Impedance complex plane plots at cell potential 3.0 V for the super-capacitors, completed using Ta_4HfC_5-CDC and $WTiC_2$-CDC electrodes, synthesized at different temperatures.

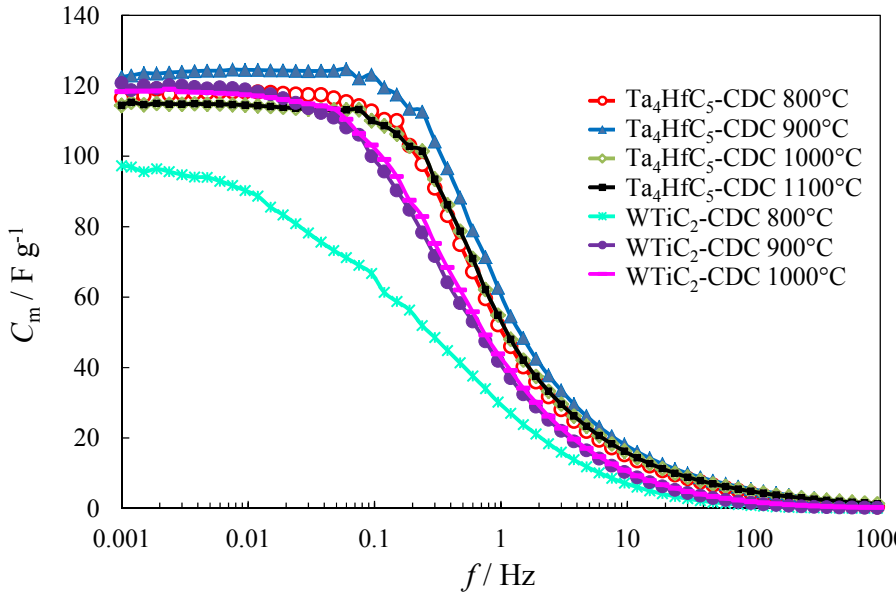

Figure 34. Specific series capacitance C_m vs. ac frequency dependencies at cell potential 3.0 V for the supercapacitors, completed using Ta_4HfC_5-CDC and $WTiC_2$-CDC electrodes, synthesized at different temperatures.

5.3.14. Ragone plots $WTiC_2$-CDC and Ta_4HfC_5-CDC

The Ragone plots for the supercapacitors based on Ta_4HfC_5-CDC and $WTiC_2$-CDC electrodes have been obtained from the constant power tests within the cell potential range from 3.0 V to 1.5 V and are shown in Figure 35a and 35b. The mass and volume conversion factors between active carbon and total electrode are 0.9 and 0.85, for Ta_4HfC_5-CDC and $WTiC_2$-CDC, respectively.

The highest energy density E_{max} value 28 Wh kg^{-1} at high power P density 10 kW kg^{-1} has been calculated for the Ta_4HfC_5-CDC (900 °C) based system. The experimental Ragone plots for the electrodes made from the synthesized CDCs show that at high power density $P \geq 10$ kW kg^{-1}, $WTiC_2$-CDC materials are inferior than those prepared from Ta_4HfC_5. It can be explained by the chemical inhomogeneity of the raw carbide and $WTiC_2$-CDC powder material and breaking down of initial $WTiC_2$ particles, verified by XRD, SEM and HRTEM data.

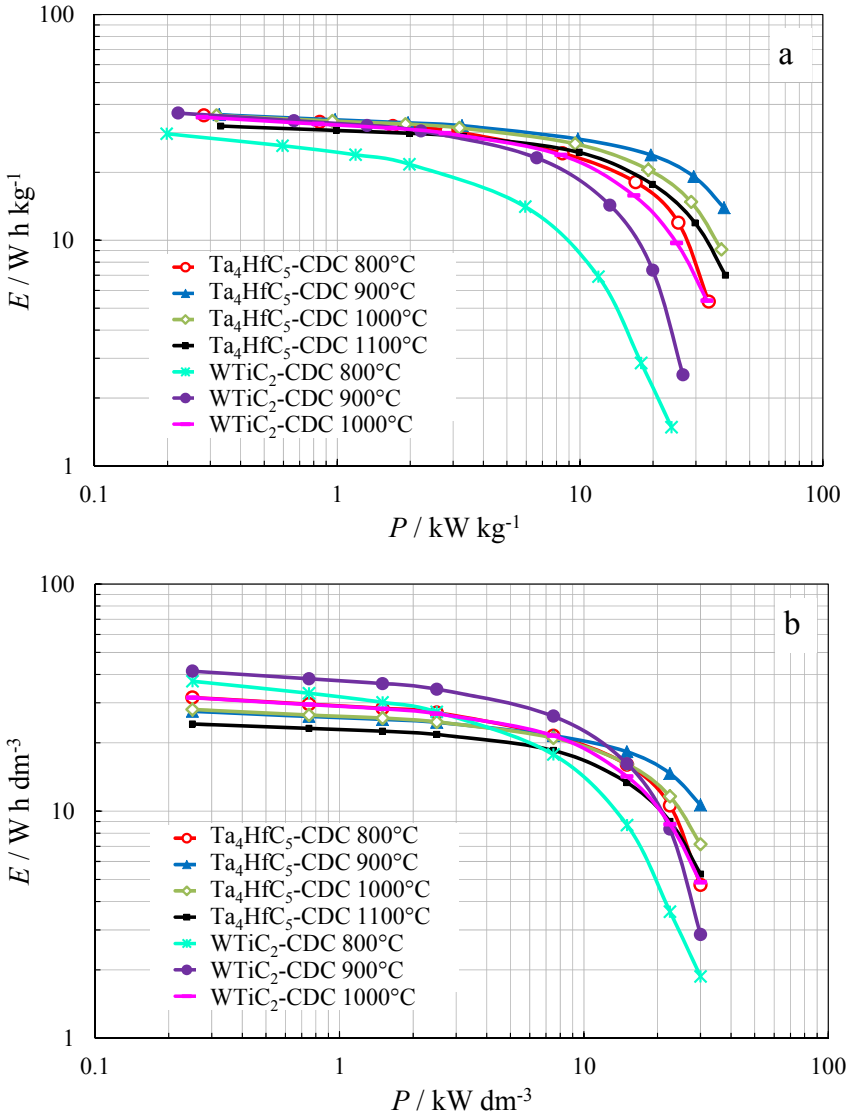

Figure 35. Gravimetric (a) and volumetric (b) Ragone plots for the supercapacitors completed using Ta_4HfC_5-CDC and $WTiC_2$-CDC electrodes, synthesized at different temperatures.

5.4. Comparative analysis of selected EDLC electrode materials

5.4.1. Physical characteristics of CDCs with optimal electrochemical characteristics

Comparison of XRD, Raman and gas adsorption data for selected materials with optimal electrochemical characteristics indicates that there is noticeable dependence of the crystallographic structure, graphitization level and micro-mesoporosity, on the raw carbide used.

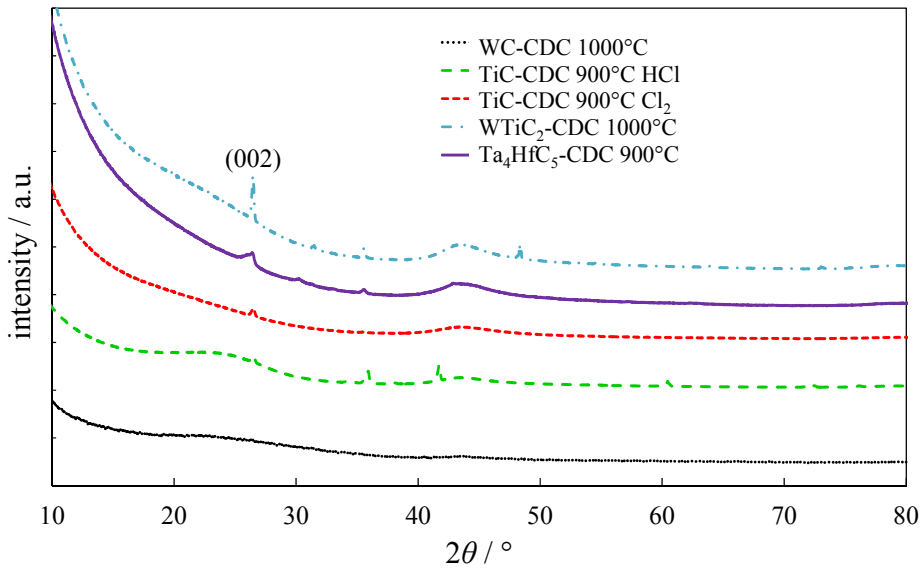

Figure 36. Comparison of XRD diffractograms for selected most promising CDCs, synthesized from WC, TiC, $WTiC_2$ and Ta_4HfC_5.

XRD data given in Figure 36 show that the shape of XRD diffractograms depends noticeably on the chemical composition and crystallographic structure of the raw carbide as well as on the synthesis temperature applied. Surprisingly, more clearly visible (002) reflections at 26°, characterizing graphitized areas in mainly amorphous CDC, can be seen in diffractograms for $WTiC_2$-CDC (1000 °C), differently for WC-CDC (1000 °C), where practically amorphous structure has been observed. The materials, synthesized at 900 °C, demonstrate the intermediate graphitization levels, however, somewhat more clearly visible graphitization has been established for TiC-CDC(HCl) and TiC-CDC(Cl_2) powders.

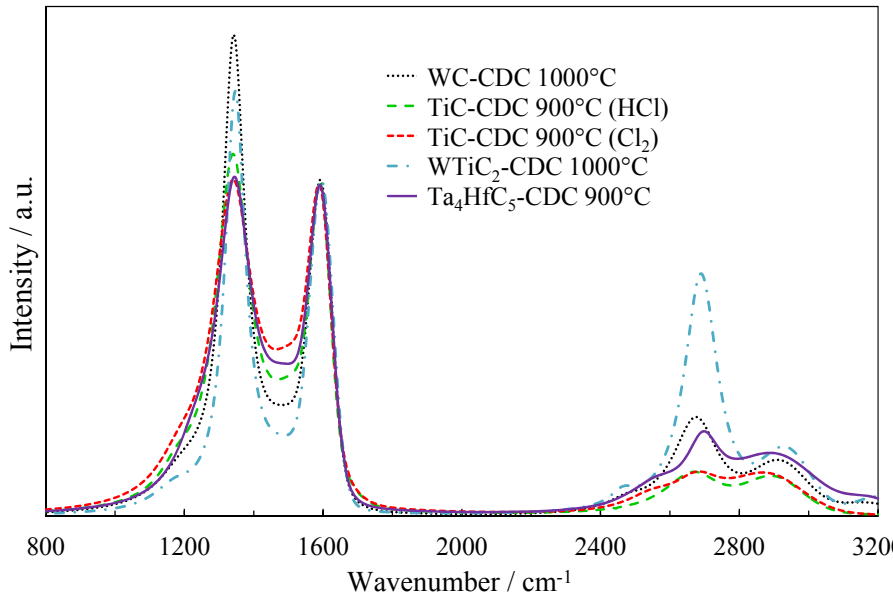

Figure 37. Raman specters for selected most promising CDCs, synthesized from WC, TiC, $WTiC_2$ and Ta_4HfC_5.

The XRD data discussed are in a good agreement with Raman spectroscopy data (Figure 37), indicating that the more clearly visible 2D peak (characterizing the existence of graphitic areas inside or on the surface of powder particles has been established for $WTiC_2$-CDC and Ta_4HfC_5-CDC. The 2D peaks are very wide and not fully developed for all TiC-CDC based carbon powders, independent of the reactant (Cl_2 or HCl) used for the synthesis of CDC.

The gas adsorption isotherms for optimal CDC powders are strongly dependent on the raw carbide used. Highest adsorbed gas volume V_{ads} has been calculated for $WTiC_2$-CDC and V_{ads} decreases in the order: $WTiC_2$-CDC > Ta_4HfC_5-CDC > TiC-CDC(Cl2) > TiC-CDC(HCl) > WC-CDC. The TiC-CDC(Cl_2), WC-CDC and especially TiC-CDC(HCl) are characterized by the hierarchical micro-mesoporous structure demonstrating the H4-type hysteresis, observed in Figure 38. The pore size distribution, pore width plots (Figure 39) have very complicated shape and surprisingly the shape of these plots is practically independent of the raw carbide used for CDC synthesis. However, clearly visible peaks can be seen in the so-called ultra-micropore region (pore width < 0.7 nm), micropore region (pore with ≤ 2 nm) and mesopore region wth (pore width > 2 nm) for all CDC under study (Figure 39).

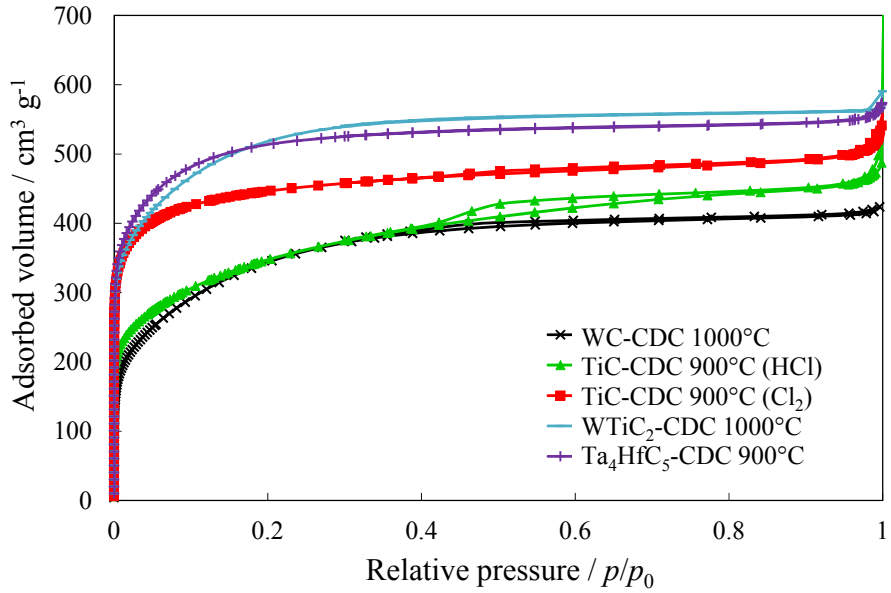

Figure 38. Sorption isotherms for selected most promising CDCs, synthesized from WC, TiC (Cl_2 or HCl), $WTiC_2$ and Ta_4HfC_5.

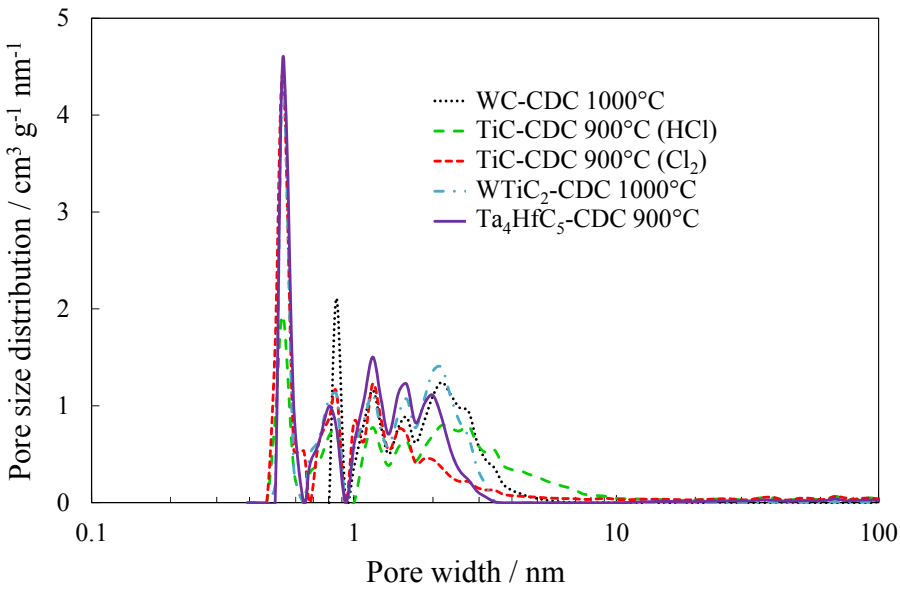

Figure 39. Pore size distributions, calculated using the NLDFT method, for selected most promising CDCs, synthesized from WC, TiC, $WTiC_2$ and Ta_4HfC_5.

5.4.2. Electrochemical characteristics of CDC with optimal electrochemical characteristics

Cell capacitance vs. potential plots, given in Figures 40 and 41, show that the cell capacitance values depend noticeably on the raw material and synthesis technology, selected for the synthesis of CDC, demonstrating that the TiC-CDC(Cl_2) has the highest and TiC-CDC(HCl) the lowest capacitance values.

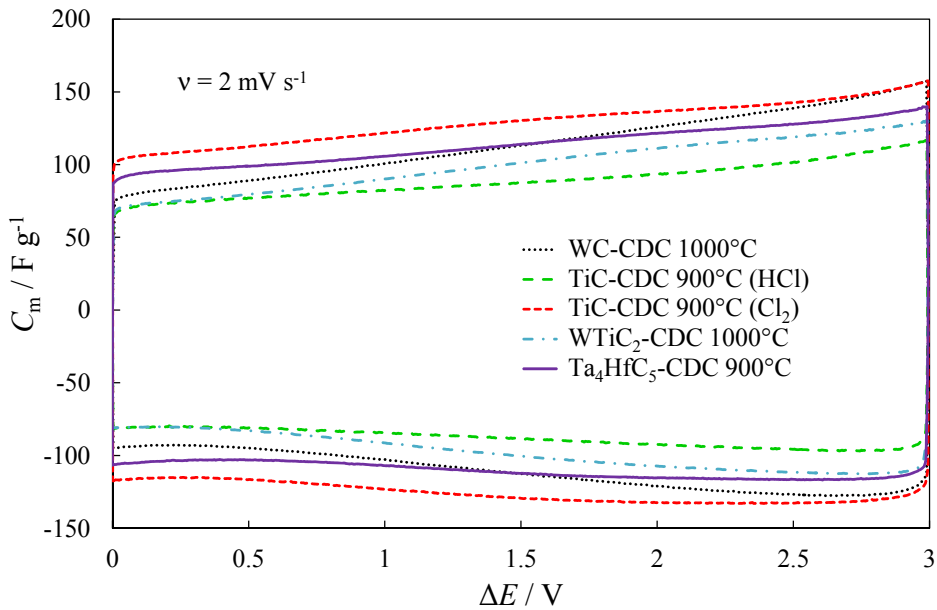

Figure 40. Specific capacitances vs. cell potential plots, calculated from cyclic voltammograms, at potential scan rate v = 2 mV s^{-1}, for selected most promising CDCs, synthesized from WC, TiC, $WTiC_2$ and Ta_4HfC_5.

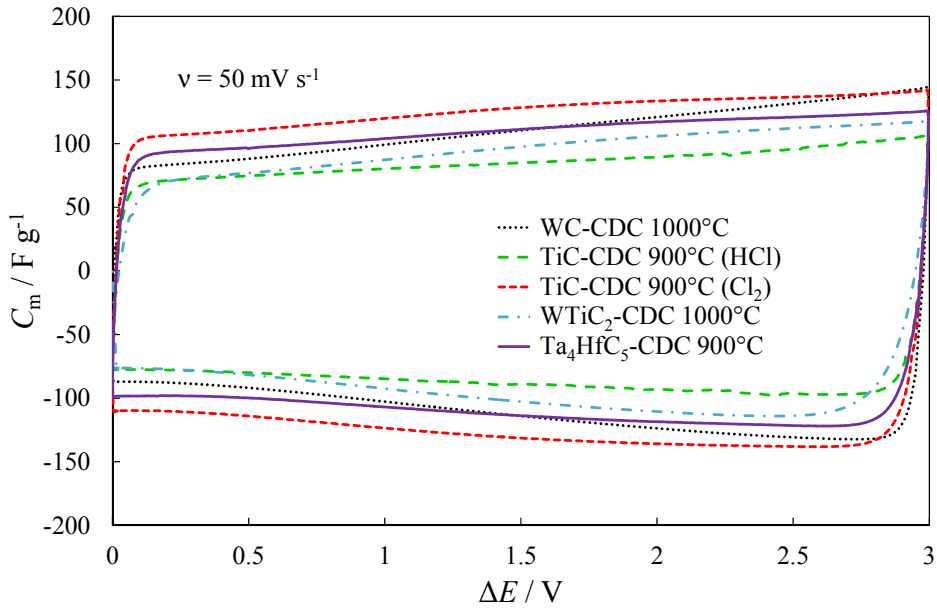

Figure 41. Specific capacitances vs. cell potential plots, calculated from cyclic voltammograms, at potential scan rate v = 50 mV s^{-1}, for selected most promising CDCs, synthesized from WC, TiC (Cl_2 and HCl), $WTiC_2$ and Ta_4HfC_5.

CDCs synthesized from WC and ternary carbides have intermediate capacitance values. The same order of series capacitance values (Figure 42) has been calculated from Nyquist plots and at ΔE = 3.0 V the C_{CV} and C_s values are overlapping for all materials prepared and selected as the best for EDLC within the experimental measurement errors (± 10 F g^{-1}).

However, the characteristic time constant τ_R values, calculated from C'' vs. f plots (Figure 43), increase in the order WC-CDC < TiC-CDC(HCl) < TiC-CDC(Cl_2) < Ta4HfC_5-CDC < $WTiC_2$-CDC.

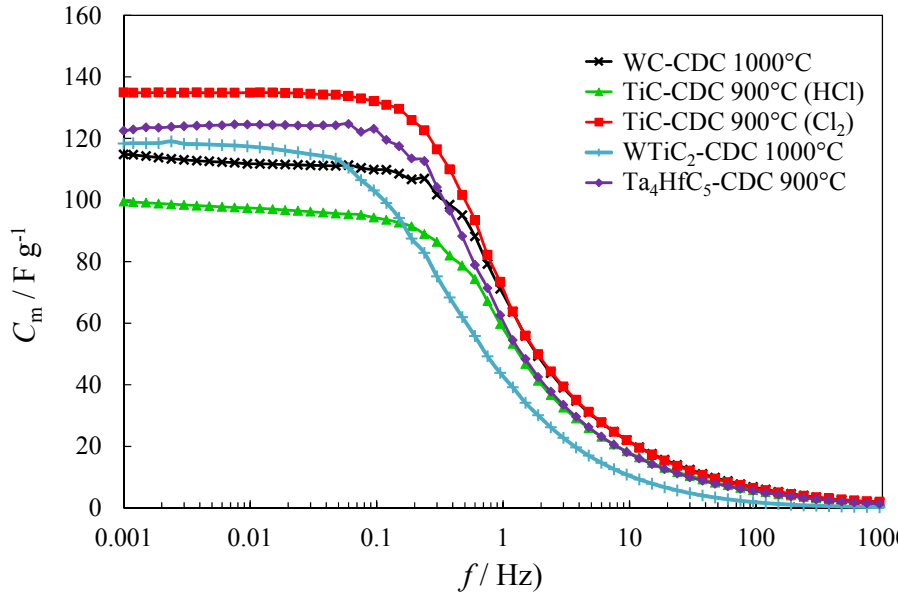

Figure 42. Specific capacitances vs. frequency plots, calculated from impedance spectroscopy at cell potential 3V, for selected most promising CDCs, synthesized from WC, TiC (Cl_2 and HCl), $WTiC_2$ and Ta_4HfC_5.

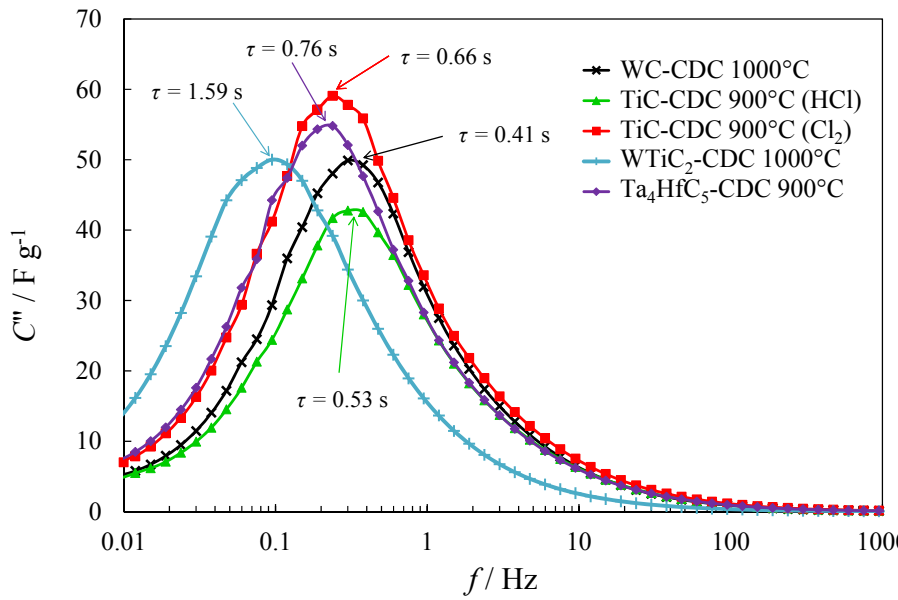

Figure 43. C'' vs. frequency plots, calculated from impedance spectroscopy at cell potential 3V, for selected most promising CDCs, synthesized from WC, TiC (Cl_2 and HCl), $WTiC_2$ and Ta_4HfC_5.

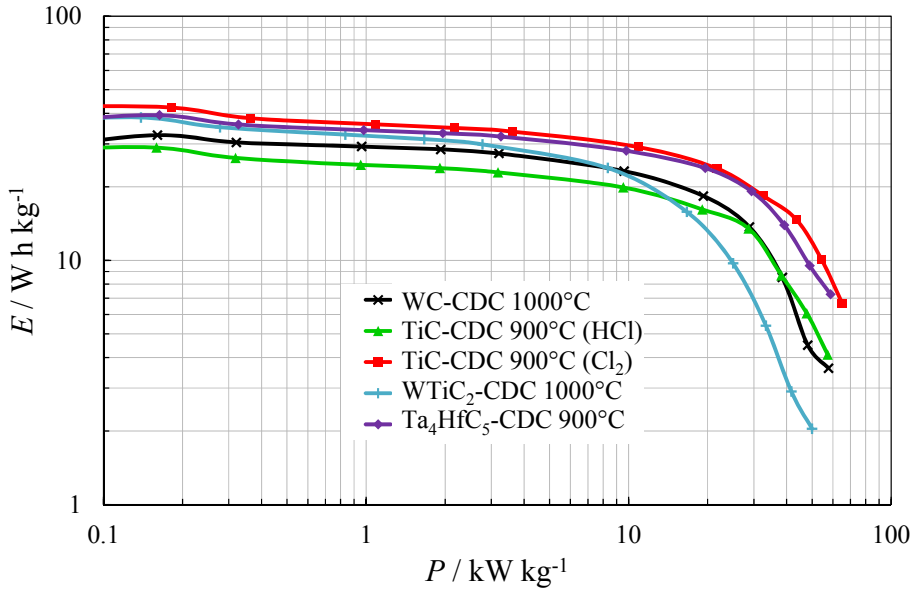

Figure 43. Gravimetric Ragone plots for selected most promising CDCs, synthesized from WC, TiC (Cl_2 and HCl), $WTiC_2$ and Ta_4HfC_5.

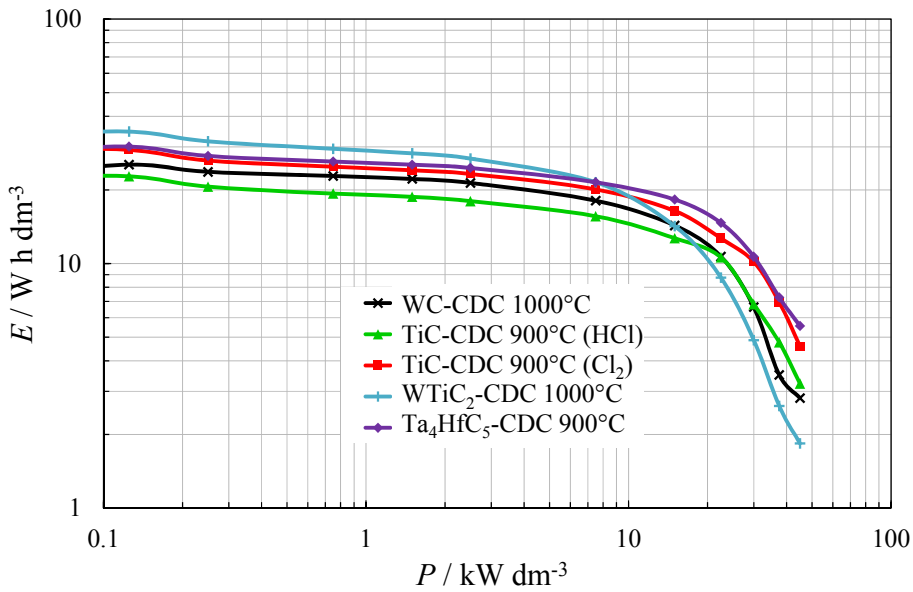

Figure 44. Volumetric Ragone plots for selected most promising CDCs, synthesized from WC, TiC (Cl_2 and HCl), $WTiC_2$ and Ta_4HfC_5.

High gravimetric energy densities at fixed power density 10 kW kg^{-1} for different CDC based single cells have been established (Figure 43), only slightly decreasing in the order: TiC-CDC(Cl_2) > Ta_4HfC_5-CDC > $WTiC_2$-CDC > WC-CDC > TiC-CDC(HCl). Due to the very strongly different density values calculated for CDC under study, the volumetric energy density increases in slightly different order (Figure 44): $WTiC_2$-CDC > Ta_4HfC_5-CDC > TiC-CDC(Cl_2) > WC-CDC > TiC-CDC(HCl). Thus, for specific applications, where the volume is limited, the ternary carbide derived carbons can have some advantages.

4. SUMMARY

Several carbide derived carbon (CDC) materials were synthesized from different binary (WC, TiC) and ternary carbides ($WTiC_2$, Ta_4HfC_5) at fixed temperatures from 700 °C to 1100 C°. For the synthesis the high temperature halogenation method was applied, while using Cl_2 (WC, TiC, $WTiC_2$, Ta_4HfC_5) or HCl (TiC) as the reactant.

The CDC materials were systematically characterized by X-ray diffraction (XRD), Raman spectroscopy, high resolution transmission electron microscopy (HRTEM), scanning electron microscopy (SEM) and low temperature N_2 sorption methods. The results of the analysis made, demonstrated that the synthesized CDC materials are mostly amorphous, with some partially graphitized areas, exposed mainly at the CDC surface regions. The degree of graphitization slightly increases with the rise of the synthesis temperature. All of the materials studied showed a complex porous structure containing both micro- and mesopores. The specific surface area, average pore size, and pore volume depend on the initial carbide used, synthesis temperature and on the chemical reactant used for synthesis of CDC. It should be noted, that the biggest change in CDC properties was the specific surface area which varied between 360 $m^2 g^{-1}$ and 1990 $m^2 g^{-1}$.

The electrochemical properties of the CDC materials under study were also investigated to evaluate their potential as an electrode material in electrical double layer capacitors (EDLC). The carbon materials were roll-pressed together with polytetrafluoroethylene as a binder after which several two-electrode test cells were completed. The electrochemical behavior of the EDLC cells has been characterized using cyclic voltammetry (CV), electrochemical impedance spectroscopy (EIS), constant current charging and discharging (CCCD) and constant power (Ragone) methods. Most of the synthesized materials demonstrated nearly ideal capacitive behavior when used as an electrode material for EDLC. However, some materials showed deviation of this ideal behavior, especially at applied higher charging and discharging currents or potential scan rates. However, somewhat surprisingly there were only small differences in specific capacitance values (120 ± 15 F g^{-1}) when comparing different CDC materials synthesized and studied. Most notable differences were demonstrated in constant power measurements, especially at very high power densities (~ 50 kW kg^{-1}).

Clear correlations have been established between the electrochemical and physical characteristics of the CDC materials synthesized. There is a strong influence of the pore size distribution on the electrochemical behavior of the CDC. Additional influence on the behavior of the completed EDLC test cells can be attributed to the graphitization and hierarchical porous structure of the CDC materials synthesized. Surprisingly, however, the effect of specific surface area of the CDC on the EDLC test cell capacitance was lower than expected.

It was found that all of the studied materials could be used as an electrode material for EDLC. However, further work should be carried out to make CDC materials from abundant carbides, while focusing the main attention on the control of the pore size distribution and graphitization level of CDC rather than only on the development of very large specific surface area.

5. REFERENCES

[1] H.O. Pierson, Handbook of Carbon, Graphite, Diamond and Fullerenes, Noyes Publications, New Jersey, 1993.

[2] F. Schuth, S.W.K. Sing, J. Weitkamp, Handb. Porous Solids 4 (2002) 1766–1960.

[3] A.G. Pandolfo, A.F. Hollenkamp, J. Power Sources 157 (2006) 11–27.

[4] T.D. Burchell, Carbon Materials for Advanced Technologies, Elsevier, Oxford, 1999.

[5] H. Marsh, Introduction to Carbon Science, Butterworths, London 1989.

[6] P. Simon, Y. Gogotsi, Nat. Mater. 7 (2008) 845–854.

[7] E. Frackowiak, F. Béguin, Carbon 39 (2001) 937–950.

[8] Y. Gogotsi, A. Nikitin, H. Ye, W. Zhou, J.E. Fischer, B. Yi, H.C. Foley, M.W. Barsoum, Nat. Mater. 2 (2003) 591–594.

[9] M. Eikerling, A.A. Kornyshev, E. Lust, J. Electrochem. Soc. 152 (2005) E24–E33.

[10] B.E. Conway, Electrochemical Supercapacitors—Scientific Fundamentals and Technological Applications, Kluwer, New York, 1999.

[11] P.J. Mahon, C.J. Drummond, Aust. J. Chem. 54 (2001) 473–476.

[12] A. Nikitin, Y. Gogotsi, Encycl. Nanosci. Nanotechnol. 7 (2004) 553–574.

[13] A. Jänes, L. Permann, M. Arulepp, E. Lust, Electrochem. Commun. 6 (2004) 313–318.

[14] T. Thomberg, H. Kurig, A. Jänes, E. Lust, Micropor. Mesopor. Mater. 141 (2011) 88–93.

[15] E.N. Hoffman, G. Yushin, T. El-Raghy, Y. Gogotsi, M.W. Barsoum, Micropor. Mesopor. Mater. 112 (2008) 526–532.

[16] R. Dash, J. Chmiola, G. Yushin, Y. Gogotsi, G. Laudisio, J. Singer, J. Fischer, S. Kucheyev, Carbon 44 (2006) 2489–2497.

[17] A. Jänes, T. Thomberg, E. Lust, Carbon 45 (2007) 2717–2722.

[18] T. Thomberg, A. Jänes, E. Lust, Electrochim. Acta 55 (2010) 3138–3143.

[19] Y. Korenblit, M. Rose, E. Kockrick, L. Borchardt, A. Kvit, S. Kaskel, G. Yushin, ACS Nano 4 (2010) 1337–1344.

[20] P. González-García, E. Urones-Garrote, D. Ávila-Brande, A. Gómez-Herrero, L.C. Otero-Díaz, Carbon 48 (2010) 3667–3675.

[21] I. Tallo, T. Thomberg, H. Kurig, K. Kontturi, A. Jänes, E. Lust, Carbon 67 (2014) 607–616.

[22] A. Burke, J. Power Sources 91 (2000) 37–50.

[23] M. Inagaki, L.R. Radovic, Nanocarbons, Carbon 40 (2002) 2263–2284.

[24] X. Bourrat, Science of Carbon Materials, Publicaciones de la Universidad de Alicante, Alicante, 2000.

[25] J. Chmiola, G. Yushin, Y. Gogotsi, C. Portet, P. Simon, P.L. Taberna, Science 313 (2006) 1760–1763.

[26] E. Frackowiak, S. Delpeux, K. Jurewicz, K. Szostak, D. Cazorla-Amoros, F. Béguin, Chem. Phys. Lett. 361 (2002) 35–41.

[27] V. Presser, M. Heon, Y. Gogotsi, Adv. Funct. Mater. 21 (2011) 810–833.

[28] S. Urbonaite, L. Hälldahl, G. Svensson, Carbon 46 (2008) 1942–1947.

[29] S. Urbonaite, J.M. Juárez-Galán, J. Leis, F. Rodríguez-Reinoso, G. Svensson, Micropor. Mesopor. Mater. 113 (2008) 14–21.

[30] A. Jänes, T. Thomberg, H. Kurig, E. Lust, Carbon 47 (2009) 23–29.

[31] J. Eskusson, A. Jänes, A. Kikas, L. Matisen, E. Lust, J. Power Sources 196 (2011) 4109–4116.
[32] A. Jänes, J. Eskusson, R. Kanarbik, A. Saar, E. Lust, J. Electrochem. Soc. 159 (2012) A1141–A1147.
[33] B.P. Bakhmatyuk, B.Y. Venhryn, I.I. Grygorchak, M.M. Micov, J. Power Sources 180 (2008) 890–895.
[34] A.K. Shukla, Resonance 6 (2001) 72–81.
[35] A. Nishino, J. Power Sources 60 (1996) 137–147.
[36] A. Kajdos, A. Kvit, F. Jones, J. Jagiello, G. Yushin, J. Am. Chem. Soc. 132 (2010) 3252–3253.
[37] A.E. Kravchik, J.A. Kukushkina, V.V. Sokolov, G.F. Tereshchenko, Carbon 44 (2006) 3263–3268.
[38] A.S. Aricò, P. Bruce, B. Scrosati, J.M. Tarascon, W. Van Schalkwijk, Nat. Mater. 4 (2005) 366–377.
[39] H. Helmholtz, Ann. Phys. Chem. 89 (1853) 211–233.
[40] S. Trasatti, J. Electroanal. Chem. 33 (1971) 351–378.
[41] S. Trasatti, Pure Appl. Chem. 58 (1986) 955–966.
[42] G. Gouy, J. Phys. 9 (1910) 457–468.
[43] D.L. Chapman, Philos. Mag. 25 (1913) 475–481.
[44] O. Stern, Z. Elektrochem. 30 (1924) 508–516.
[45] A.N. Frumkin, O.A. Petrii, B.B. Damaskin, Potentials of Zero Charge, In: Comprehensive Treatise of Electrochemistry, Plenum, New York, 1980.
[46] D.G. Grahame, Chem. Rev. 41 (1947) 441–501.
[47] W. Kohn, L.J. Sham, Phys. Rev. 140 (1965) A1133–A1138.
[48] O.K. Rice, J. Am. Chem. Soc. 49 (1927) 1617–1629.
[49] L.H. Thomas, Math. Proc. Camb. Philos. Soc. 23 (1927) 542–548.
[50] E. Fermi, Rend. Accad. Naz. Lincei. 6 (1927) 602–607.
[51] S. Amokrane, J.P. Badiali, J. Electroanal. Chem. 266 (1989) 21–35.
[52] A.A. Kornyshev, W. Schmickler, M.A. Vorotyntsev, Phys. Rev. B 25 (1982) 5244–5256.
[53] E. Lust, A. Jänes, V. Sammelselg, P. Miidla, K. Lust, Electrochim. Acta 44 (1998) 373–383.
[54] B.B. Damaskin, V.A. Safonov, Electrochim. Acta 42 (1997) 737–746.
[55] K. Tõnurist, T. Thomberg, A. Jänes, T. Romann, V. Sammelselg, E. Lust, J. Electroanal. Chem. 689 (2013) 8–20.
[56] B.E. Conway, W.G. Pell, J. Solid State Electrochem. 7 (2003) 637–644.
[57] A.F. Burke, T.C. Murphy, Mat. Res. Soc. Symp. Proc 393 (1995) 375–95.
[58] A. Burke, M. Arulepp, Electrochem. Soc. Proc. PV 2001-21 (2001) 576–591.
[59] A. Laheäär, A.L. Peikolainen, M. Koel, A. Jänes, E. Lust, J. Solid State Electrochem. 16 (2012) 2717–2722.
[60] R. Palm, H. Kurig, K. Tõnurist, A. Jänes, E. Lust, Electrochim. Acta 85 (2012) 139–144.
[61] K. Tõnurist, I. Vaas, T. Thomberg, A. Jänes, H. Kurig, T. Romann, E. Lust, Electrochim. Acta 119 (2014) 72–77.
[62] S. Brunauer, L.S. Deming, W.E. Deming, E. Teller, J. Am. Chem. Soc. 62 (1940) 1723–1732.
[63] B.C. Lippens, J.H. de Boer, Studies on pore systems in catalysts. V. The t method, J. Catal. 4 (1965) 319–323.
[64] S. Brunauer, P.H. Emmett, E. Teller, J. Am. Chem. Soc. 60 (1938) 309–319.

[65] A.A. Isirikyan, A.V. Kiselev, J. Phys. Chem. 65 (1961) 601–607.
[66] P.I. Ravikovitch, A.V. Neimark, Colloids Surf. Physicochem. Eng. Asp. 187-188 (2001) 11–21.
[67] S.J. Gregg, K.S.W. Sing, Adsorption, surface area, and porosity, Academic Press, London, 1982.
[68] J.H. de Boer, B.C. Lippens, B.G. Linsen, J.C.P. Broekhoff, A. van den Heuvel, T.J. Osinga, J. Colloid Interf. Sci. 21 (1966) 405–414.
[69] J.H. de Boer, B.G. Linsen, T. van der Plas, G.J. Zondervan, J. Catal. 4 (1965) 649–653.
[70] M.M. Dubinin, L.V. Radushkevich, Chem. Zentr. 1 (1947) 875–889.
[71] H. Marsh, B. Rand, J. Colloid Interf. Sci. 33 (1970) 101–116.
[72] M.J.G. Janssen, C.W.M. van Oorschot, The Characterization of Zeolites by Gas Adsorption, in Zeolites: Facts, Figures, Future, Elsevier, London, 1989.
[73] R. Evans, U.M.B. Marconi, P. Tarazona, J. Chem. Phys. 84 (1986) 2376–2399.
[74] P.I. Ravikovitch, A. Vishnyakov, A.V. Neimark, Phys. Rev. E 64 (2001) 011602/1–011602/20.
[75] F. Rouquerol, J. Rouquerol, K. Sing, Adsorption by Powders and Porous Solids, Academic Press, London, 1999.
[76] H.P. Klug, L.E. Alexander, X-ray Diffraction Procedures for Polycrystalline and Amorphous Materials, John Wiley, New York, 1974.
[77] M.S. Seehra, A.S. Pavlovic, Carbon 31 (1993) 557–564.
[78] V. Suresh Babu, M.S. Seehra, Carbon 34 (1996) 1259–1265.
[79] M. Inagaki, New Carbons - Control of Structure and Functions, Elsevier, New York, 2000.
[80] A. Cuesta, P. Dhamelincourt, J. Laureyns, A. Martínez-Alonso, J.M.D. Tascón, Appl. Spectrosc. 52 (1998) 356–360.
[81] A. Sharma, T. Kyotani, A. Tomita, Carbon 38 (2000) 1977–1984.
[82] G.A. Zickler, B. Smarsly, N. Gierlinger, H. Peterlik, O. Paris, Carbon 44 (2006) 3239–3246.
[83] A.C. Ferrari, J. Robertson, Phys. Rev. B 61 (2000) 14095–14107.
[84] A.C. Ferrari, Solid State Commun. 143 (2007) 47–57.
[85] D. Roy, M. Chhowalla, H. Wang, N. Sano, I. Alexandrou, T.W. Clyne, G.A.J. Amaratunga, Chem. Phys. Lett. 373 (2003) 52–56.
[86] D. McCulloch, S. Prawer, A. Hoffman, Phys. Rev. B. 50 (1994) 5905–5917.
[87] F. Tuinstra, J.L. Koenig, J. Chem. Phys. 53 (1970) 1126–1130.
[88] R.J. Nemanich, S.A. Solin, Phys. Rev. B 20 (1979) 392–401.
[89] R.P. Vidano, D.B. Fischbach, L.J. Willis, T.M. Loehr, Solid State Commun. 39 (1981) 341–344.
[90] M.S. Dresselhaus, G. Dresselhaus, M. Hofmann, Vib. Spectrosc. 45 (2007) 71–81.
[91] D.B. Williams, C.B. Carter, Transmission Electron Microscopy, Plenum Press, New York, 1996.
[92] B. Jouffrey, P. Schattschneider, C. Hébert, Ultramicroscopy 102 (2004) 61–66.
[93] R.F. Egerton, Electron Energy-Loss Spectroscopy in the Electron Microscope, Plenum Press, New York, 1996.
[94] S. Urbonaite, S. Wachtmeister, C. Mirguet, E. Coronel, W.Y. Zou, S. Csillag, G. Svensson, Carbon 45 (2007) 2047–2053.
[95] W.G. Pell, B.E. Conway, J. Electroanal. Chem. 500 (2001) 121–133.

[96] E. Gileadi, Electrode Kinetics for Chemists, Chemical Engineers, and Materials Scientists, VCH Publishers, New York, 1993.
[97] V.S. Bagotsky, Fundamentals of Electrochemistry, John Wiley & Sons Incorporated, New York, 2005.
[98] J.R. Miller, P. Simon, Science 321 (2008) 651–652.
[99] E. Barsoukov, J.R. Macdonald, Impedance spectroscopy: theory, experiment, and applications, Wiley, John & Sons, Incorporated, 2005.
[100] P.L. Taberna, P. Simon, J.F. Fauvarque, J. Electrochem. Soc. 150 (2003) A292–A300.
[101] E. Lust, A. Jänes, M. Arulepp, J. Solid State Electrochem. 8 (2004) 488–496.
[102] R. Kötz, M. Carlen, Electrochim. Acta 45 (2000) 2483–2498.
[103] F. Beguin, E. Frackowiak, Supercapacitors: Materials, Systems and Applications, John Wiley & Sons, 2013.
[104] J.P. Meyers, M. Doyle, R.M. Darling, J. Newman, J. Electrochem. Soc. 147 (2000) 2930–2940.
[105] P. Simon, A. Burke, Electrochem. Soc. Interf. 17 (2008) 38–43.
[106] M. Arulepp, J. Leis, M. Lätt, F. Miller, K. Rumma, E. Lust, A.F. Burke, J. Power Sources 162 (2006) 1460–1466.
[107] I. Tallo, T. Thomberg, K. Kontturi, A. Jänes, E. Lust, Carbon 49 (2011) 4427–4433.
[108] I. Tallo, T. Thomberg, A. Jänes, E. Lust, J. Electrochem. Soc. 159 (2012) A208–A213.
[109] I. Tallo, T. Thomberg, H. Kurig, A. Jänes, K. Kontturi, E. Lust, J. Solid State Electrochem. 17 (2013) 19–28.
[110] M. Naguib, O. Mashtalir, J. Carle, V. Presser, J. Lu, L. Hultman, et al., ACS Nano 6 (2012) 1322–1331.
[111] C.R. Pérez, S.H. Yeon, J. Ségalini, V. Presser, P.L. Taberna, P. Simon, Y. Gogotsi, Adv. Funct. Mater. 23 (2013) 1081–1089.
[112] J. Chmiola, G. Yushin, R. Dash, Y. Gogotsi, J. Power Sources 158 (2006) 765–772.

6. SUMMARY IN ESTONIAN

Uute mikro-mesopoorsete karbiididest sünteesitud süsinikmaterjalide valmistamine ning karakteriseerimine kõrge energia- ja võimsustihedusega elektrilise kaksikkihi kondensaatori elektroodimaterjalina

Uurimustöö käigus valmistati erinevaid karbiididest sünteesitud süsinikmaterjale (KSS) binaarsetest (WC, TiC) ja ternaarsetest ($WTiC_2$, Ta_4HfC_4) karbiididest. Kõrgtemperatuurne karbiidide halogeenimine teostati kindlatel temperatuuridel vahemikus 700 °C kuni 1100 °C. Halogeenimise käigus kasutati reagendina kloori (WC, TiC, $WTiC_2$, Ta_4HfC_4) või vesinikkloriidi (TiC).

Sünteesitud KSS materjalide karakteriseerimiseks kasutati röntgendifraktsiooni, Raman spektroskoopia, skaneeriva elektronmikroskoopia ja madaltemperatuurse N_2 sorptsiooni meetodeid. Teostatud analüüside tulemused näitasid, et sünteesitud KSS materjalid on peamiselt amorfsed, kuid sisaldavad mõningal määral ka grafiitsemaid alasid, mis esinesid peamiselt osakeste pinnal. KSS sünteesi temperatuuri kasvuga suurenes grafitiseerunud süsiniku osakaal materjalis. Sünteesitud materjalidel oli kompleksne poorne struktuur, milles esinesid nii mikro- kui mesopoorid. Sõltuvalt lähtekarbiidi ja regendi valikust ning sünteesi temperatuurist, varieerusid saadud KSS materjalidel eripind, keskmine poori suurus ja pooride koguruumala. Kõige suurem erinevus KSS materjalide puhul oli BET meetodil arvutatud eripinna väärtus, mis varieerus vahemikus 360 $m^2 g^{-1}$ kuni 1990 $m^2 g^{-1}$.

Hindamaks sünteesitud KSS materjalide sobivust elektrilise kaksikkihi kondensaatori (EKKK) elektroodimaterjalina, uuriti nende elektrokeemilist käitumist tsüklilise voltamperomeetria, konstantse voolu, konstantse võimsuse ning elektrokeemilise impedantsspektroskoopia meetoditega. Enamus sünteesitud KSS materjalidest valmistatud elektroodidega EKKKd demonstreerisid peaaegu ideaalset mahtuvuslikku käitumist. Siiski esines mõne materjali puhul suuremaid kõrvalekaldeid ideaalsest mahtuvuslikust käitumisest ning seda just eelkõige täis- ja tühjakslaadimisel suurtel voolutihedustel või suurtel potentsiaali laotuskiirustel. Enamasti jäid sünteesitud KSS materjalidest tehtud elektroodide mahtuvuse väärtused vahemikku 120 ± 15 F g^{-1}. Kõige tähelepanuväärsemad erinevused materjalide elektrokeemilisel käitumisel ilmnesid konstantse võimsuse mõõtmistel, eriti suurtel võimsustihedustel (~ 50 kW kg^{-1}).

Töö käigus leiti selgepiirilised korrelatsioonid sünteesitud KSS materjalide füüsikaliste karakteristikute ning valmistatud elektroodidega EKKK elektrokeemiliste omaduste vahel. Väga tugevalt mõjutab EKKK elektrokeemilist käitumist tühjaks- ja täislaadimisel elektroodis kasutatava süsinikmaterjali poorijaotus. Samuti on võimalik täheldada grafitiseerunud süsiniku osakaalu ja sellest tuleneva juhtivuse mõju uuritud EKKK käitumisele. Mõnevõrra üllatuslikult ei mõjutanud sünteesitud materjalide eripinna väärtuse mitmekordne erinevus oluliselt koostatud EKKK mahtuvuse väärtusi.

Leiti, et kõiki uuritud süsinikmaterjale on võimalik kasutada elektrilise kaksikkihi kondensaatori elektroodimaterjalina. Tuginedes uurimustöö käigus saadud andmetele ja tehtud analüüsile, tuleks edaspidi keskenduda KSS valmistamisel odavatele ning laialt kättesaadavatele karbiididele ning pöörata põhitähelepanu sobiva grafitiseerituse ulatuse, poorijaotuse ja selle hierarhilise struktuuri saavutamisele ning mitte keskenduma ainult ülisuure eripinna saavutamisele.

7. ACKNOWLEDGEMENTS

I would like to express my greatest gratitude to my supervisors Professor Enn Lust, Dr. Alar Jänes and Dr Thomas Thomberg for all their guidance, encouragement, support and above all patience during the time of my studies in the University of Tartu. Additionally I would like to thank Dr. Heisi Kurig and Rait Kanarbik for all the scientific discussions and technical support during all these years.

Most of all I would like to thank my family who has always stood by my side.

This research is financially supported by the Estonian Ministry of Education and Research project SF0180002s08 and by the Estonian Science Foundation under Project Nos. 8172 and 7606, COST Action MP1004, by the graduate school ‘‘Functional materials and technologies’’, receiving funding from the European Social Fund under project 1.2.0401.09-0079 in Estonia, by the Estonian Center of Excellence in Science project 3.2.0101.11-0030, Estonian Energy Technology Program project 3.2.0501.10-0015, Material Technology Program project 3.2.1101.12-0019, Project of European Structure Funds 3.2.0601.11-0001, Estonian target research project IUT20–13, Ministry of Education and Research Personal Research Grant PUT55 and project 3.2.0302.10-0169.

8. PUBLICATIONS

CURRICULUM VITAE

Name:	Indrek Tallo
Date of birth:	August 30, 1984
Citizenship:	Estonian
Address:	Institute of Chemistry, University of Tartu Ravila 14a, 50411 Tartu, Estonia
Current position:	University of Tartu, Institute of Chemistry, Chemist
Telephone:	+372 737 6625
E-mail:	indrek.tallo@ut.ee

Education:

2011–…	University of Tartu, Institute of Chemistry, PhD student in Chemistry
2010–2011	University of Tartu – Master's degree in materials science
2007–2010	University of Tartu – Bachelor degree in materials science
2003–2007	University of Tartu – Unfinished Bachelor studies in physics
2000–2003	Tallinna Reaalkool – secondary education
1997–2000	Tallinna 21. Kool – higher basic education
1991–1997	Tallinna Kuristiku Gümnaasium – basic education

Language skill:

Estonian	native language
English	very good in speech and writing
Finnish	average in speech, bad in writing
Russian	bad in speech and writing

Professional career:

2009–...	University of Tartu, Institute of Chemistry, Chemist
2005–2006	Estonian Nanotechnology Competence Centre; Lab worker (0.50)

Main field of research:

Natural sciences and engineering, Chemistry and chemical technology, Electrochemistry, Supercapacitors

A list of publications:

Tallo, T. Thomberg, K. Kontturi, A. Jänes, E. Lust, Nanostructured carbide-derived carbon synthesized by chlorination of tungsten carbide, Carbon 49 (2011) 4427–4433.

Tallo, T. Thomberg, A. Jänes, E. Lust. Electrochemical Behaviour of α–Tungsten Carbide–Derived Carbon Based Electric Double–Layer Capacitors, Journal of Electrochemical Society 159 (2012) A208–A213.

Tallo, T. Thomberg, A. Jänes, E. Lust, Comparative study of using chlorine and hydrogen chloride for synthesis of titanium carbide derived karbon, ECS Transactions 50(43) (2012) 3–12.

Tallo, T. Thomberg, H. Kurig, A. Jänes, K. Kontturi, E. Lust. Supercapacitors based on carbide-derived carbons synthesised using HCl and Cl2 as reactants, Journal of Solid State Chemistry 17(1) (2013) 19–28.

Tallo, T. Thomberg, A. Jänes, E. Lust, Replacing Chlorine with Hydrogen Chloride as a Possible Reactant for Synthesis of Titanium Carbide Derived Carbon Powders for High-Technology Devices, IOP Conference Series: Materials Science and Engineering 49 (1) (2013) art. no. 012018.

K. Vaarmets, S. Sepp, J. Nerut, E. Härk, I. Tallo, E. Lust, Electrochemical and physical characterization of Pt–Ru alloy catalyst deposited onto micro-porous–mesoporous carbon support derived from Mo2C at 600 °C, Journal of Solid State Electrochemistry 17(6) (2013) 1729–1741.

E. Härk, J. Nerut, K. Vaarmets, I. Tallo, H. Kurig, J. Eskusson, K. Kontturi, E. Lust, Electrochemical Impedance Characteristics and Electroreduction of Oxygen at Tungsten Carbide Derived Micromesoporous Carbon Electrodes, Journal of Electroanalytical Chemistry 689 (2013) 176–184.

Tallo, T. Thomberg, H. Kurig, K. Kontturi, A. Jänes, E. Lust. Novel micro-mesoporous carbon materials synthesized from tantalum hafnium carbide and tungsten titanium carbide, Carbon 67 (2014) 607–616.

E. Lust, K. Vaarmets, J. Nerut, I. Tallo, P. Valk, S. Sepp, E. Härk,. Influence of specific surface area and microporosity-mesoporosity of pristine and Pt-nanoclusters modified carbide derived carbon electrodes on the oxygen electroreduction, Electrochimica Acta 140(SI) (2014) 294–303.

E. Tee, I. Tallo, H. Kurig, T. Thomberg, A. Jänes, E. Lust, Huge enhancement of energy storage capacity and power density of supercapacitors based on the carbon dioxide activated microporous SiC-CDC, Electrochimica Acta 161 (2015) 364–370.

Participation in international conferences:

Tallo, T. Thomberg, A. Jänes, E. Lust, Optimisation of Tungsten Carbide-derived Carbon as Electrode Material for Supercapacitors. 221st ECS Meeting, USA, Seattle, 6–10 May 2012 (oral presentation).

Tallo, T. Thomberg, A. Jänes, E. Lust, Comparative Study of Using Chlorine and Hydrogen Chloride for Synthesis of Titanium Carbide Derived Carbon, PRiME 2012, Honolulu, Hawaii, 7–12 Oct. 2012 (poster presentation).

Tallo, T. Thomberg, A. Jänes, E. Lust, (2013). Hydrogen chloride as a possible reactant for synthesis of titanium carbide derived carbon powders for high-technology devices, Functional materials and Nanotechnologies-2013, Tartu, Estonia, 21–24 April 2013 (poster presentation).

Tallo, A. Jänes, E. Lust New micromesoporous carbon material for super-capacitors synthesized from Ta4HfC5 and WTiC2, International Conference on Advanced Capacitors, Osaka, Japan, 27–30 May 2013 (oral presentation).

A list of projects:

Development of materials and single cells for solid oxide and polymer electrolyte fuel cells, high temperature electrolyzers and supercapacitors SLOKT10209T.

Development of micro/mesoporous carbon materials and electrolytes for high energy and power density electrical double layer capacitors, hybrid supercapacitors and lithium-ion batteries ETF8172.

European Spallation Source: Estonian Partition in ESS Instrument design, development and building and application for scientific research SLOKT12026T.

Functional Micro/Mesoporous Nanomaterials for Novel Energy Conversion and Storage Systems IUT20-13.

Functionalization of carbon nanomaterials: synthesis, characterization and application SLOKT12180.

Nano/mesoporous nanofibre polymer membranes for non-aqueous electrical double layer supercapacitors ETF7606.

Physical and electrochemical properties of hydrogen, different solutions and hydrides in micro-/mesoporous carbon materials PUT55.

Processes at modified phase boundaries and development of novel electrochemical power sources and supercapacitors SF0180002s08.

Research grants and scholarships:

2010–2014	Grant stipend
2012	2012 Kristjan Jaak travel grant
2014–2015	Elering AS scholarship

Teaching work:

Information regarding the teaching work carried out at universities:

LOKT.02.023	Chemistry of Nanoporous and Nanostructural Materials. (Lecturer: 2011–2015)
LOKT.02.046	Materials Technology (Lecturer and practical work supervisor: 2013–2015)

Supervision:

Ester Tee	2013 defended Bachelor thesis “The Influence of Activation on the Physical Characteristics of Silicon Carbide Derived Carbons” 2015 defended Master thesis “The Influence of Activation Conditions on the Physical and Electrochemical Characteristics of Silicon Carbide Derived Carbons”

ELULOOKIRJELDUS

Nimi: Indrek Tallo
Sünniaeg: 30. august 1984
Kodakondsus: Eesti
Aadress: Keemia instituut, Tartu Ülikool
Ravila 14a, 50411 Tartu, Eesti
Telefon: +372 7376625
E-post: indrek.tallo@ut.ee
Töökoht: Tartu Ülikool, Keemia Instituut, keemik

Haridus:

2011–…	Tartu Ülikool – Doktoriõpe keemia erialal
2010–2011	Tartu Ülikool – Magistrikraad materjaliteaduses
2007–2010	Tartu Ülikool – Bakalaureusekraad materjaliteaduses
2003–2007	Tartu Ülikool – Lõpetamata bakalaureus füüsikas
2000–2003	Tallinna Reaalkool – Keskharidus
1997–2000	Tallinna 21. Kool – Põhiharidus (7.–9. klass)
1991–1997	Tallinna Kuristiku Gümnaasium – Põhiharidus (1.–6. klass)

Keelteoskus:

Eesti keel	emakeel
Inglise keel	väga hea kõnes ja kirjas
Soome keel	rahuldav kõnes, kehv kirjas
Vene keel	kehv kõnes ja kirjas

Teenistuskäik:

2009–...	Tartu Ülikool, Keemia Instituut; keemik
2005–2006	Eesti Nanotehnoloogiate Arenduskeskus; laborant

Peamised uurimisvaldkonnad:
Loodusteadused ja tehnika, keemia ja keemiatehnika, elektrokeemia, superkondensaatorid

Publikatsioonide loetelu:

Tallo, T. Thomberg, K. Kontturi, A. Jänes, E. Lust, Nanostructured carbide-derived carbon synthesized by chlorination of tungsten carbide, Carbon 49 (2011) 4427–4433.

Tallo, T. Thomberg, A. Jänes, E. Lust. Electrochemical Behaviour of α–Tungsten Carbide–Derived Carbon Based Electric Double–Layer Capacitors, Journal of Electrochemical Society 159 (2012) A208–A213.

Tallo, T. Thomberg, A. Jänes, E. Lust, Comparative study of using chlorine and hydrogen chloride for synthesis of titanium carbide derived karbon, ECS Transactions 50(43) (2012) 3–12.

Tallo, T. Thomberg, H. Kurig, A. Jänes, K. Kontturi, E. Lust. Supercapacitors based on carbide-derived carbons synthesised using HCl and Cl2 as reactants, Journal of Solid State Chemistry 17(1) (2013) 19–28.

Tallo, T. Thomberg, A. Jänes, E. Lust, Replacing Chlorine with Hydrogen Chloride as a Possible Reactant for Synthesis of Titanium Carbide Derived Carbon Powders for High-Technology Devices, IOP Conference Series: Materials Science and Engineering 49 (1) (2013) art. no. 012018.

K. Vaarmets, S. Sepp, J. Nerut, E. Härk, I. Tallo, E. Lust, Electrochemical and physical characterization of Pt–Ru alloy catalyst deposited onto microporous–mesoporous carbon support derived from Mo2C at 600 °C, Journal of Solid State Electrochemistry 17(6) (2013) 1729–1741.

E. Härk, J. Nerut, K. Vaarmets, I. Tallo, H. Kurig, J. Eskusson, K. Kontturi, E. Lust, Electrochemical Impedance Characteristics and Electroreduction of Oxygen at Tungsten Carbide Derived Micromesoporous Carbon Electrodes, Journal of Electroanalytical Chemistry 689 (2013) 176–184.

Tallo, T. Thomberg, H. Kurig, K. Kontturi, A. Jänes, E. Lust. Novel micro-mesoporous carbon materials synthesized from tantalum hafnium carbide and tungsten titanium carbide, Carbon 67 (2014) 607–616.

E. Lust, K. Vaarmets, J. Nerut, I. Tallo, P. Valk, S. Sepp, E. Härk,. Influence of specific surface area and microporosity-mesoporosity of pristine and Pt-nanoclusters modified carbide derived carbon electrodes on the oxygen electroreduction, Electrochimica Acta 140(SI) (2014) 294–303.

E. Tee, I. Tallo, H. Kurig, T. Thomberg, A. Jänes, E. Lust, Huge enhancement of energy storage capacity and power density of supercapacitors based on the carbon dioxide activated microporous SiC-CDC, Electrochimica Acta 161 (2015) 364–370.

Rahvusvahelistel konverentsidel osalemine:

Tallo, T. Thomberg, A. Jänes, E. Lust, Optimisation of Tungsten Carbide-derived Carbon as Electrode Material for Supercapacitors. 221st ECS Meeting, USA, Seattle, 6–10 May 2012 (suuline ettekanne).

Tallo, T. Thomberg, A. Jänes, E. Lust, Comparative Study of Using Chlorine and Hydrogen Chloride for Synthesis of Titanium Carbide Derived Carbon, PRiME 2012, Honolulu, Hawaii, 7–12 Oct. 2012 (poster ettekanne).

Tallo, T. Thomberg, A. Jänes, E. Lust, (2013). Hydrogen chloride as a possible reactant for synthesis of titanium carbide derived carbon powders for high-technology devices, Functional materials and Nanotechnologies-2013, Tartu, Estonia, 21–24 April 2013 (poster ettekanne).

Tallo, A. Jänes, E. Lust New micromesoporous carbon material for supercapacitors synthesized from Ta4HfC5 and WTiC2, International Conference on Advanced Capacitors, Osaka, Japan, 27–30 May 2013 (suuline ettekanne).

Projektide loetelu:

Tahkeoksiidsete ja madaltemperatuursete kütuseelementide, elektrolüüserite ja superkondensaatorite materjalide ja ühiskrakkude väljatöötamine ja testimine SLOKT10209T.

Mikro/mesopoorsete süsinikmaterjalide ja elektrolüütide väljatöötamine suure energia- ja võimsustihedusega elektrilise kaksikkihi kondensaatoritele, hübriidsuperkondensaatoritele ja liitium-ioon patareidele ETF8172.

Eesti osalemine ESS instrumentide kavandamisel, projekteerimisel ja ehitamisel ning rakendamisel teaduslikeks uuringuteks (ESSource) SLOKT12026T.

Funktsionaalsed mikro/mesopoorsed materjalid kõrgefektiivsete energia muundamise ja salvestamise süsteemides IUT20-13.

Süsinik-nanomaterjalide funktsionalisatsioon, süntees, karakteriseerimine ja rakendused SLOKT12180.

Nano/mesopoorsed nanokiud polümeersed membraanid mittevesilahustel põhinevatele elektrilise kaksikkihi superkondensaatoritele ETF7606.

Vesiniku, erinevate lahuste ja hüdriidide füüsikaliste ja elektrokeemiliste omaduste uurminie mikro-/mesopoorsetes süsinikmaterjalides.

Protsessid modifitseeritud piirpindadel ja faasides ning nende rakendused uuetüübilistes energia allikates ning superkondensaatoritesSF0180002s08.

Saadud uurimistoetused ja stipendiumid:

2010–2014	Grandistipendium
2012	2012 Kristjan Jaagu reisistipendium
2014–2015	Elering AS Energeetikastipendium

Andmed kõrgkoolis tehtud auditoorse õppetöö kohta:

LOKT.02.023	Nanopoorsete ja nanostruktuursete materjalide keemia (Loengute andmine: 2011–2015)
LOKT.02.046	Materjalide tehnoloogia (loengute andmine ning praktilise töö juhendamine: 2013–2015)

Juhendamine:

Ester Tee	2013 kaitses bakalaureusetöö teemal „Aktiveerimise mõju ränikarbiidist sünteesitud süsiniku füüsikalistele karakteristikutele“ 2015 kaitses magistritöö teemal „Ränikarbiidist sünteesitud ning süsinikdioksiidiga järelaktiveeritud süsiniku füüsikalised ja elektrokeemilised omadused”

DISSERTATIONES CHIMICAE UNIVERSITATIS TARTUENSIS

1. **Toomas Tamm.** Quantum-chemical simulation of solvent effects. Tartu, 1993, 110 p.
2. **Peeter Burk.** Theoretical study of gas-phase acid-base equilibria. Tartu, 1994, 96 p.
3. **Victor Lobanov.** Quantitative structure-property relationships in large descriptor spaces. Tartu, 1995, 135 p.
4. **Vahur Mäemets.** The ^{17}O and ^{1}H nuclear magnetic resonance study of H_2O in individual solvents and its charged clusters in aqueous solutions of electrolytes. Tartu, 1997, 140 p.
5. **Andrus Metsala.** Microcanonical rate constant in nonequilibrium distribution of vibrational energy and in restricted intramolecular vibrational energy redistribution on the basis of slater's theory of unimolecular reactions. Tartu, 1997, 150 p.
6. **Uko Maran.** Quantum-mechanical study of potential energy surfaces in different environments. Tartu, 1997, 137 p.
7. **Alar Jänes.** Adsorption of organic compounds on antimony, bismuth and cadmium electrodes. Tartu, 1998, 219 p.
8. **Kaido Tammeveski.** Oxygen electroreduction on thin platinum films and the electrochemical detection of superoxide anion. Tartu, 1998, 139 p.
9. **Ivo Leito.** Studies of Brønsted acid-base equilibria in water and non-aqueous media. Tartu, 1998, 101 p.
10. **Jaan Leis.** Conformational dynamics and equilibria in amides. Tartu, 1998, 131 p.
11. **Toonika Rinken.** The modelling of amperometric biosensors based on oxidoreductases. Tartu, 2000, 108 p.
12. **Dmitri Panov.** Partially solvated Grignard reagents. Tartu, 2000, 64 p.
13. **Kaja Orupõld.** Treatment and analysis of phenolic wastewater with microorganisms. Tartu, 2000, 123 p.
14. **Jüri Ivask.** Ion Chromatographic determination of major anions and cations in polar ice core. Tartu, 2000, 85 p.
15. **Lauri Vares.** Stereoselective Synthesis of Tetrahydrofuran and Tetrahydropyran Derivatives by Use of Asymmetric Horner-Wadsworth-Emmons and Ring Closure Reactions. Tartu, 2000, 184 p.
16. **Martin Lepiku.** Kinetic aspects of dopamine D_2 receptor interactions with specific ligands. Tartu, 2000, 81 p.
17. **Katrin Sak.** Some aspects of ligand specificity of P2Y receptors. Tartu, 2000, 106 p.
18. **Vello Pällin.** The role of solvation in the formation of iotsitch complexes. Tartu, 2001, 95 p.

19. **Katrin Kollist.** Interactions between polycyclic aromatic compounds and humic substances. Tartu, 2001, 93 p.
20. **Ivar Koppel.** Quantum chemical study of acidity of strong and superstrong Brønsted acids. Tartu, 2001, 104 p.
21. **Viljar Pihl.** The study of the substituent and solvent effects on the acidity of OH and CH acids. Tartu, 2001, 132 p.
22. **Natalia Palm.** Specification of the minimum, sufficient and significant set of descriptors for general description of solvent effects. Tartu, 2001, 134 p.
23. **Sulev Sild.** QSPR/QSAR approaches for complex molecular systems. Tartu, 2001, 134 p.
24. **Ruslan Petrukhin.** Industrial applications of the quantitative structure-property relationships. Tartu, 2001, 162 p.
25. **Boris V. Rogovoy.** Synthesis of (benzotriazolyl)carboximidamides and their application in relations with *N*- and *S*-nucleophyles. Tartu, 2002, 84 p.
26. **Koit Herodes.** Solvent effects on UV-vis absorption spectra of some solvatochromic substances in binary solvent mixtures: the preferential solvation model. Tartu, 2002, 102 p.
27. **Anti Perkson.** Synthesis and characterisation of nanostructured carbon. Tartu, 2002, 152 p.
28. **Ivari Kaljurand.** Self-consistent acidity scales of neutral and cationic Brønsted acids in acetonitrile and tetrahydrofuran. Tartu, 2003, 108 p.
29. **Karmen Lust.** Adsorption of anions on bismuth single crystal electrodes. Tartu, 2003, 128 p.
30. **Mare Piirsalu.** Substituent, temperature and solvent effects on the alkaline hydrolysis of substituted phenyl and alkyl esters of benzoic acid. Tartu, 2003, 156 p.
31. **Meeri Sassian.** Reactions of partially solvated Grignard reagents. Tartu, 2003, 78 p.
32. **Tarmo Tamm.** Quantum chemical modelling of polypyrrole. Tartu, 2003. 100 p.
33. **Erik Teinemaa.** The environmental fate of the particulate matter and organic pollutants from an oil shale power plant. Tartu, 2003. 102 p.
34. **Jaana Tammiku-Taul.** Quantum chemical study of the properties of Grignard reagents. Tartu, 2003. 120 p.
35. **Andre Lomaka.** Biomedical applications of predictive computational chemistry. Tartu, 2003. 132 p.
36. **Kostyantyn Kirichenko.** Benzotriazole – Mediated Carbon–Carbon Bond Formation. Tartu, 2003. 132 p.
37. **Gunnar Nurk.** Adsorption kinetics of some organic compounds on bismuth single crystal electrodes. Tartu, 2003, 170 p.
38. **Mati Arulepp.** Electrochemical characteristics of porous carbon materials and electrical double layer capacitors. Tartu, 2003, 196 p.

39. **Dan Cornel Fara.** QSPR modeling of complexation and distribution of organic compounds. Tartu, 2004, 126 p.
40. **Riina Mahlapuu.** Signalling of galanin and amyloid precursor protein through adenylate cyclase. Tartu, 2004, 124 p.
41. **Mihkel Kerikmäe.** Some luminescent materials for dosimetric applications and physical research. Tartu, 2004, 143 p.
42. **Jaanus Kruusma.** Determination of some important trace metal ions in human blood. Tartu, 2004, 115 p.
43. **Urmas Johanson.** Investigations of the electrochemical properties of polypyrrole modified electrodes. Tartu, 2004, 91 p.
44. **Kaido Sillar.** Computational study of the acid sites in zeolite ZSM-5. Tartu, 2004, 80 p.
45. **Aldo Oras.** Kinetic aspects of dATPαS interaction with $P2Y_1$ receptor. Tartu, 2004, 75 p.
46. **Erik Mölder.** Measurement of the oxygen mass transfer through the air-water interface. Tartu, 2005, 73 p.
47. **Thomas Thomberg.** The kinetics of electroreduction of peroxodisulfate anion on cadmium (0001) single crystal electrode. Tartu, 2005, 95 p.
48. **Olavi Loog.** Aspects of condensations of carbonyl compounds and their imine analogues. Tartu, 2005, 83 p.
49. **Siim Salmar.** Effect of ultrasound on ester hydrolysis in aqueous ethanol. Tartu, 2006, 73 p.
50. **Ain Uustare.** Modulation of signal transduction of heptahelical receptors by other receptors and G proteins. Tartu, 2006, 121 p.
51. **Sergei Yurchenko.** Determination of some carcinogenic contaminants in food. Tartu, 2006, 143 p.
52. **Kaido Tämm.** QSPR modeling of some properties of organic compounds. Tartu, 2006, 67 p.
53. **Olga Tšubrik.** New methods in the synthesis of multisubstituted hydrazines. Tartu. 2006, 183 p.
54. **Lilli Sooväli.** Spectrophotometric measurements and their uncertainty in chemical analysis and dissociation constant measurements. Tartu, 2006, 125 p.
55. **Eve Koort.** Uncertainty estimation of potentiometrically measured ph and pK_a values. Tartu, 2006, 139 p.
56. **Sergei Kopanchuk.** Regulation of ligand binding to melanocortin receptor subtypes. Tartu, 2006, 119 p.
57. **Silvar Kallip.** Surface structure of some bismuth and antimony single crystal electrodes. Tartu, 2006, 107 p.
58. **Kristjan Saal.** Surface silanization and its application in biomolecule coupling. Tartu, 2006, 77 p.
59. **Tanel Tätte.** High viscosity $Sn(OBu)_4$ oligomeric concentrates and their applications in technology. Tartu, 2006, 91 p.

60. **Dimitar Atanasov Dobchev**. Robust QSAR methods for the prediction of properties from molecular structure. Tartu, 2006, 118 p.
61. **Hannes Hagu**. Impact of ultrasound on hydrophobic interactions in solutions. Tartu, 2007, 81 p.
62. **Rutha Jäger.** Electroreduction of peroxodisulfate anion on bismuth electrodes. Tartu, 2007, 142 p.
63. **Kaido Viht.** Immobilizable bisubstrate-analogue inhibitors of basophilic protein kinases: development and application in biosensors. Tartu, 2007, 88 p.
64. **Eva-Ingrid Rõõm.** Acid-base equilibria in nonpolar media. Tartu, 2007, 156 p.
65. **Sven Tamp.** DFT study of the cesium cation containing complexes relevant to the cesium cation binding by the humic acids. Tartu, 2007, 102 p.
66. **Jaak Nerut.** Electroreduction of hexacyanoferrate(III) anion on Cadmium (0001) single crystal electrode. Tartu, 2007, 180 p.
67. **Lauri Jalukse.** Measurement uncertainty estimation in amperometric dissolved oxygen concentration measurement. Tartu, 2007, 112 p.
68. **Aime Lust.** Charge state of dopants and ordered clusters formation in CaF_2:Mn and CaF_2:Eu luminophors. Tartu, 2007, 100 p.
69. **Iiris Kahn**. Quantitative Structure-Activity Relationships of environmentally relevant properties. Tartu, 2007, 98 p.
70. **Mari Reinik.** Nitrates, nitrites, N-nitrosamines and polycyclic aromatic hydrocarbons in food: analytical methods, occurrence and dietary intake. Tartu, 2007, 172 p.
71. **Heili Kasuk.** Thermodynamic parameters and adsorption kinetics of organic compounds forming the compact adsorption layer at Bi single crystal electrodes. Tartu, 2007, 212 p.
72. **Erki Enkvist.** Synthesis of adenosine-peptide conjugates for biological applications. Tartu, 2007, 114 p.
73. **Svetoslav Hristov Slavov**. Biomedical applications of the QSAR approach. Tartu, 2007, 146 p.
74. **Eneli Härk.** Electroreduction of complex cations on electrochemically polished Bi(*hkl*) single crystal electrodes. Tartu, 2008, 158 p.
75. **Priit Möller.** Electrochemical characteristics of some cathodes for medium temperature solid oxide fuel cells, synthesized by solid state reaction technique. Tartu, 2008, 90 p.
76. **Signe Viggor.** Impact of biochemical parameters of genetically different pseudomonads at the degradation of phenolic compounds. Tartu, 2008, 122 p.
77. **Ave Sarapuu.** Electrochemical reduction of oxygen on quinone-modified carbon electrodes and on thin films of platinum and gold. Tartu, 2008, 134 p.
78. **Agnes Kütt.** Studies of acid-base equilibria in non-aqueous media. Tartu, 2008, 198 p.

79. **Rouvim Kadis.** Evaluation of measurement uncertainty in analytical chemistry: related concepts and some points of misinterpretation. Tartu, 2008, 118 p.
80. **Valter Reedo.** Elaboration of IVB group metal oxide structures and their possible applications. Tartu, 2008, 98 p.
81. **Aleksei Kuznetsov.** Allosteric effects in reactions catalyzed by the cAMP-dependent protein kinase catalytic subunit. Tartu, 2009, 133 p.
82. **Aleksei Bredihhin.** Use of mono- and polyanions in the synthesis of multisubstituted hydrazine derivatives. Tartu, 2009, 105 p.
83. **Anu Ploom.** Quantitative structure-reactivity analysis in organosilicon chemistry. Tartu, 2009, 99 p.
84. **Argo Vonk.** Determination of adenosine A_{2A}- and dopamine D_1 receptor-specific modulation of adenylate cyclase activity in rat striatum. Tartu, 2009, 129 p.
85. **Indrek Kivi.** Synthesis and electrochemical characterization of porous cathode materials for intermediate temperature solid oxide fuel cells. Tartu, 2009, 177 p.
86. **Jaanus Eskusson.** Synthesis and characterisation of diamond-like carbon thin films prepared by pulsed laser deposition method. Tartu, 2009, 117 p.
87. **Marko Lätt.** Carbide derived microporous carbon and electrical double layer capacitors. Tartu, 2009, 107 p.
88. **Vladimir Stepanov.** Slow conformational changes in dopamine transporter interaction with its ligands. Tartu, 2009, 103 p.
89. **Aleksander Trummal.** Computational Study of Structural and Solvent Effects on Acidities of Some Brønsted Acids. Tartu, 2009, 103 p.
90. **Eerold Vellemäe.** Applications of mischmetal in organic synthesis. Tartu, 2009, 93 p.
91. **Sven Parkel.** Ligand binding to 5-HT_{1A} receptors and its regulation by Mg^{2+} and Mn^{2+}. Tartu, 2010, 99 p.
92. **Signe Vahur.** Expanding the possibilities of ATR-FT-IR spectroscopy in determination of inorganic pigments. Tartu, 2010, 184 p.
93. **Tavo Romann**. Preparation and surface modification of bismuth thin film, porous, and microelectrodes. Tartu, 2010, 155 p.
94. **Nadežda Aleksejeva.** Electrocatalytic reduction of oxygen on carbon nanotube-based nanocomposite materials. Tartu, 2010, 147 p.
95. **Marko Kullapere.** Electrochemical properties of glassy carbon, nickel and gold electrodes modified with aryl groups. Tartu, 2010, 233 p.
96. **Liis Siinor.** Adsorption kinetics of ions at Bi single crystal planes from aqueous electrolyte solutions and room-temperature ionic liquids. Tartu, 2010, 101 p.
97. **Angela Vaasa.** Development of fluorescence-based kinetic and binding assays for characterization of protein kinases and their inhibitors. Tartu 2010, 101 p.

98. **Indrek Tulp.** Multivariate analysis of chemical and biological properties. Tartu 2010, 105 p.
99. **Aare Selberg.** Evaluation of environmental quality in Northern Estonia by the analysis of leachate. Tartu 2010, 117 p.
100. **Darja Lavõgina.** Development of protein kinase inhibitors based on adenosine analogue-oligoarginine conjugates. Tartu 2010, 248 p.
101. **Laura Herm.** Biochemistry of dopamine D_2 receptors and its association with motivated behaviour. Tartu 2010, 156 p.
102. **Terje Raudsepp.** Influence of dopant anions on the electrochemical properties of polypyrrole films. Tartu 2010, 112 p.
103. **Margus Marandi.** Electroformation of Polypyrrole Films: *In-situ* AFM and STM Study. Tartu 2011, 116 p.
104. **Kairi Kivirand.** Diamine oxidase-based biosensors: construction and working principles. Tartu, 2011, 140 p.
105. **Anneli Kruve.** Matrix effects in liquid-chromatography electrospray mass-spectrometry. Tartu, 2011, 156 p.
106. **Gary Urb.** Assessment of environmental impact of oil shale fly ash from PF and CFB combustion. Tartu, 2011, 108 p.
107. **Nikita Oskolkov.** A novel strategy for peptide-mediated cellular delivery and induction of endosomal escape. Tartu, 2011, 106 p.
108. **Dana Martin.** The QSPR/QSAR approach for the prediction of properties of fullerene derivatives. Tartu, 2011, 98 p.
109. **Säde Viirlaid.** Novel glutathione analogues and their antioxidant activity. Tartu, 2011, 106 p.
110. **Ülis Sõukand.** Simultaneous adsorption of Cd^{2+}, Ni^{2+}, and Pb^{2+} on peat. Tartu, 2011, 124 p.
111. **Lauri Lipping.** The acidity of strong and superstrong Brønsted acids, an outreach for the "limits of growth": a quantum chemical study. Tartu, 2011, 124 p.
112. **Heisi Kurig.** Electrical double-layer capacitors based on ionic liquids as electrolytes. Tartu, 2011, 146 p.
113. **Marje Kasari.** Bisubstrate luminescent probes, optical sensors and affinity adsorbents for measurement of active protein kinases in biological samples. Tartu, 2012, 126 p.
114. **Kalev Takkis.** Virtual screening of chemical databases for bioactive molecules. Tartu, 2012, 122 p.
115. **Ksenija Kisseljova**. Synthesis of aza-β^3-amino acid containing peptides and kinetic study of their phosphorylation by protein kinase A. Tartu, 2012, 104 p.
116. **Riin Rebane.** Advanced method development strategy for derivatization LC/ESI/MS. Tartu, 2012, 184 p.

117. **Vladislav Ivaništšev.** Double layer structure and adsorption kinetics of ions at metal electrodes in room temperature ionic liquids. Tartu, 2012, 128 p.
118. **Irja Helm.** High accuracy gravimetric Winkler method for determination of dissolved oxygen. Tartu, 2012, 139 p.
119. **Karin Kipper.** Fluoroalcohols as Components of LC-ESI-MS Eluents: Usage and Applications. Tartu, 2012, 164 p.
120. **Arno Ratas.** Energy storage and transfer in dosimetric luminescent materials. Tartu, 2012, 163 p.
121. **Reet Reinart-Okugbeni**. Assay systems for characterisation of subtype-selective binding and functional activity of ligands on dopamine receptors. Tartu, 2012, 159 p.
122. **Lauri Sikk.** Computational study of the Sonogashira cross-coupling reaction. Tartu, 2012, 81 p.
123. **Karita Raudkivi.** Neurochemical studies on inter-individual differences in affect-related behaviour of the laboratory rat. Tartu, 2012, 161 p.
124. **Indrek Saar.** Design of GalR2 subtype specific ligands: their role in depression-like behavior and feeding regulation. Tartu, 2013, 126 p.
125. **Ann Laheäär.** Electrochemical characterization of alkali metal salt based non-aqueous electrolytes for supercapacitors. Tartu, 2013, 127 p.
126. **Kerli Tõnurist.** Influence of electrospun separator materials properties on electrochemical performance of electrical double-layer capacitors. Tartu, 2013, 147 p.
127. **Kaija Põhako-Esko.** Novel organic and inorganic ionogels: preparation and characterization. Tartu, 2013, 124 p.
128. **Ivar Kruusenberg.** Electroreduction of oxygen on carbon nanomaterial-based catalysts. Tartu, 2013, 191 p.
129. **Sander Piiskop.** Kinetic effects of ultrasound in aqueous acetonitrile solutions. Tartu, 2013, 95 p.
130. **Ilona Faustova**. Regulatory role of L-type pyruvate kinase N-terminal domain. Tartu, 2013, 109 p.
131. **Kadi Tamm.** Synthesis and characterization of the micro-mesoporous anode materials and testing of the medium temperature solid oxide fuel cell single cells. Tartu, 2013, 138 p.
132. **Iva Bozhidarova Stoyanova-Slavova.** Validation of QSAR/QSPR for regulatory purposes. Tartu, 2013, 109 p.
133. **Vitali Grozovski**. Adsorption of organic molecules at single crystal electrodes studied by *in situ* STM method. Tartu, 2014, 146 p.
134. **Santa Veikšina**. Development of assay systems for characterisation of ligand binding properties to melanocortin 4 receptors. Tartu, 2014, 151 p.
135. **Jüri Liiv.** PVDF (polyvinylidene difluoride) as material for active element of twisting-ball displays. Tartu, 2014, 111 p.

136. **Kersti Vaarmets.** Electrochemical and physical characterization of pristine and activated molybdenum carbide-derived carbon electrodes for the oxygen electroreduction reaction. Tartu, 2014, 131 p.
137. **Lauri Tõntson**. Regulation of G-protein subtypes by receptors, guanine nucleotides and Mn^{2+}. Tartu, 2014, 105 p.
138. **Aiko Adamson.** Properties of amine-boranes and phosphorus analogues in the gas phase. Tartu, 2014, 78 p.
139. **Elo Kibena**. Electrochemical grafting of glassy carbon, gold, highly oriented pyrolytic graphite and chemical vapour deposition-grown graphene electrodes by diazonium reduction method. Tartu, 2014, 184 p.
140. **Teemu Näykki.** Novel Tools for Water Quality Monitoring – From Field to Laboratory. Tartu, 2014, 202 p.
141. **Karl Kaupmees.** Acidity and basicity in non-aqueous media: importance of solvent properties and purity. Tartu, 2014, 128 p.
142. **Oleg Lebedev**. Hydrazine polyanions: different strategies in the synthesis of heterocycles. Tartu, 2015, 118 p.
143. **Geven Piir.** Environmental risk assessment of chemicals using QSAR methods. Tartu, 2015, 123 p.
144. **Olga Mazina.** Development and application of the biosensor assay for measurements of cyclic adenosine monophosphate in studies of G protein-coupled receptor signalinga. Tartu, 2015, 116 p.
145. **Sandip Ashokrao Kadam.** Anion receptors: synthesis and accurate binding measurements. Tartu, 2015, 118 p.